Cylindrical Quantum Dots, Spin Qubits, and Decoherence

A thesis submitted in
partial fulfillment of the requirements
for the degree of

DOCTOR OF PHILOSOPHY

by

Agile Mathew

Centre for Nanotechnology
Indian Institute of Technology Guwahati

April 2014

Certificate

This is to certify that the work contained in this thesis, entitled **"Cylindrical Quantum Dots, Spin Qubits and, Decoherence"** has been carried out by Agile Mathew with my supervision and that this work has not been submitted elsewhere for a degree.

April 2014

Sd/–
Dr. Malay K. Nandy
Associate Professor
Department of Physics
Indian Institute of Technology
Guwahati, India

To my wife, daughter and mother

Acknowledgements

I would like to acknowledge my supervisor Dr. Malay Kumar Nandy for the inspiring discussions I had with him, and also for his teachings and guidance throughout the course of this work.

I would like to thank Prof. Arun Chattopadhyay and Prof. Siddhartha S. Ghosh, former heads of the Centre, for giving me the opportunity to work at the Centre for Nanotechnology, IIT Guwahati.

I would like to thank Prof. Roy P. Paily, the present head of the Centre, for his regular encouragements and support during the entire period of my doctoral research.

I would like to thank all the members of my doctoral committee viz. Dr. Ashish K. Gupta, Dr. Charudatt Y. Kadolkar, Dr. Sukanta Pati, Prof. Arun Chattopadhyay and Dr. Malay K. Nandy for their encouragements and suggestions throughout the progress of this work.

I would like to thank my colleagues Dr. N. Ramakrishnan, Dr. Krishna K. Dey, Dr. Anto Pradeep, Dr. Aneesh Rajendran, Arun Mathew and many others from the Centre and other departments for making my time in the Institute academically more interesting.

I would like to acknowledge my parents Sri. P.S. Mathew and Smt. Treesa Mathew and my brother Alok Mathew for lovingly supporting my desire to pursue higher education. I also acknowledge the prayers and support of my parents-in-law.

I would like to thank some of the members from Christian fellowship at IIT Guwahati, viz. Samuel Jedidiah, Ravi Bolleddu and family, Simon Peter and family, Rohit Singh, Nishanth P.V., Yennam Rajesh, Srinivasa Rao, Wilfred Godfrey, Rajendra Pamula, T.L. Haokip and

family, and Nelson Muthu for the relationship, prayers and encouragements during my stay in IIT Guwahati Campus.

I want to give special thanks to my wife Blessy Joy for constantly standing with me till the completion of this work with perseverance and prayers on my behalf. I very much enjoyed the birth and upbringing of my little daughter Vismayah A. Mathew during the course of this work.

Most of all, I thank my Lord Jesus Christ for his loving and caring relationship that keeps me in the ups and downs of this earthly life.

Abstract

The broad area of this research work comes under semiconductor quantum dots and quantum computation. The specific motivation for the thesis came from Loss-DiVincenzo proposal [Phys. Rev. A 57, (1998) 120], where they showed how electron spins in semiconductor quantum dots could be used for the realization of a scalable quantum computer. In their work, the confinement of electrons in z-direction is achieved through band gap engineering and that in x-y direction is achieved through gate electrodes. This resulted in harmonic confinement potentials in x and y directions where the electrons are held while the information on it is being processed. In our work, a different scenario is proposed where the need for lateral charge confining gate electrodes is totally eliminated. Instead, completely heterostructured and/or impurity potential confined quantum dots are employed for holding electrons in x and y directions. This modification comes with advantages as well as disadvantages. The advantage is that we can now increase the number of quantum bits in a given area of semiconductor material, which is very important as far as miniaturization of a scalable system is concerned. The disadvantage of our proposal is that we cannot move around electrons anymore by manipulating their lateral confining potential. But this is no problem if we succeed in moving around the qubit (information) without having to move around the electron itself. This we show can be achieved through the manipulation of the strength of external magnetic field alone. We also show how we can achieve useful two-qubit quantum gate operation by switching the external magnetic field for required periods of time. In the final part of the thesis, we studied decoherence, which is the effect of environment that spoils the quantum coherence of a qubit. In the present scenario, the interaction

of a qubit with the nuclear spins in the semiconductor material poses the greatest challenge for proper functioning of quantum gate operation. Using approximate models, we have studied decoherence for single and two qubit cases with and without the presence of external magnetic field. In both cases, we find that the coherence is lost gradually with respect to time and a characteristic value for decoherence-time comparable to certain reported experimental values are obtained. We also see how the decoherence process depends on the nature of interaction incorporated in the model.

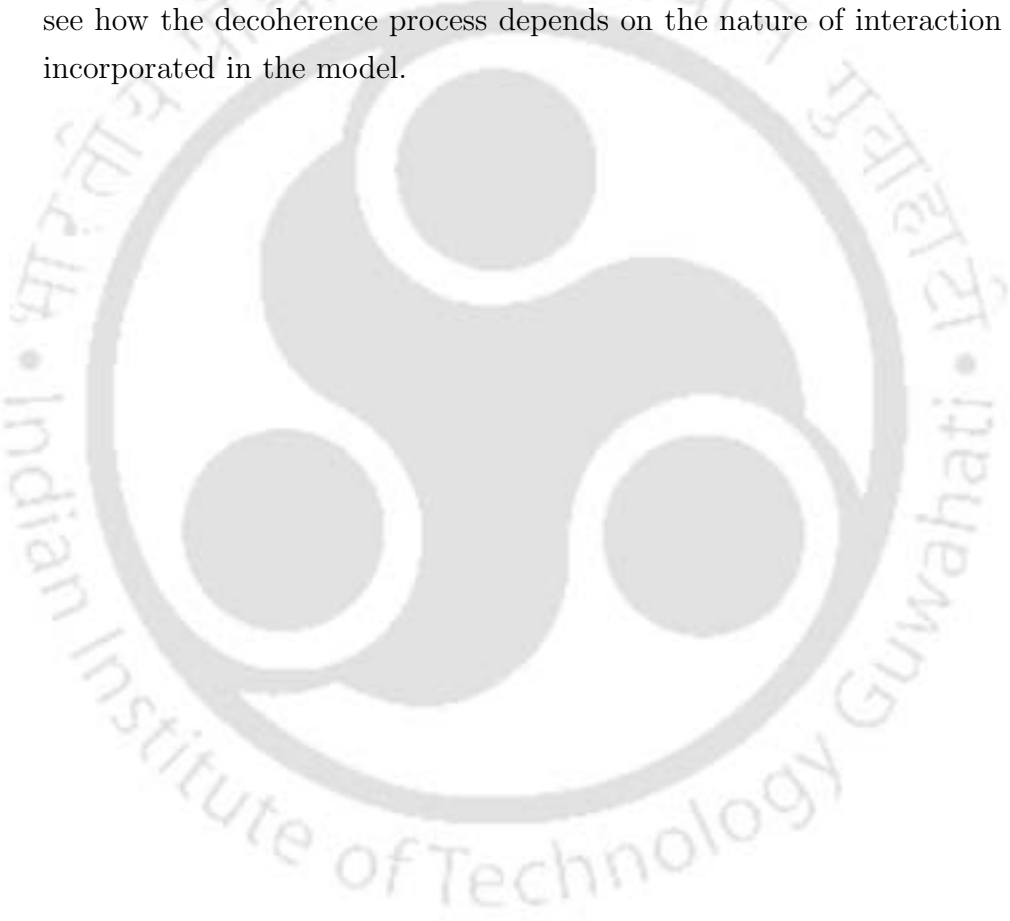

Contents

List of Figures

Chapter 1

Introduction

"But our present QM formalism is not purely epistemological; it is a peculiar mixture describing in part realities of Nature, in part incomplete human information about Nature — all scrambled up by Heisenberg and Bohr into an omelette that nobody has seen how to unscramble." — Edwin Thompson Jaynes

1.1 Quantum States

The discovery of quantum mechanics in the early 20^{th} century resulted in a breakthrough in understanding the world of atoms and microscopic particles. Quantum mechanics taught us to think about any form of matter as a wave and as a particle. For example, in the double-slit experiment, light behaves as waves and in photo-electric effect, it behave as particles. The central object around which the quantum theory is built are observables, things we can measure in a physical system. Examples are energy, position, momentum, angular momentum etc. According to quantum theory, observables correspond to operators in a linear vector space (LVS). Their eigen values and eigen vectors denote possible measured values and states after the measurements, respectively. Since the value an observable takes after measurement is always real, the operator must be Hermitian. Thus the problem of analyzing a quantum system is reduced to solving an eigen value problem in an LVS. The dynamics of the system is determined by

a differential equation called the Schrodinger equation, which specifies the time evolution of the state vector inside the LVS. Further, the state of the system is unknown before the measurement and in general it is not the same before and after measurement. Two observables do not have simultaneous eigen states if their operators do not commute. This led to what is called the Heisenberg's uncertainty principle, which tells one cannot simultaneously determine the exact values of any two non-commuting observables.

To appreciate further, let us consider a single electron in a one dimensional space. We can represent the electron state vector $|s\rangle$ in any basis which completely span the LVS of the quantum system. It is mostly a practice to use the basis corresponding to the position observable, in which the state vector is written as

$$|s(t)\rangle = \int_{-\infty}^{\infty} dx\, \psi(x,t)\, |x\rangle\,, \tag{1.1}$$

where x is the position of the electron and $\psi(x,t)$ is the probability amplitude for electron to be in state $|x\rangle$ at time t. The probability of finding the electron in the infinitesimally small distance dx at a position x is given by $|\psi(x,t)|^2 dx$. Since the total probability is equal to one, we have the normalization condition

$$\int_{-\infty}^{\infty} |\psi(x,t)|^2 dx = 1. \tag{1.2}$$

The state represented by Eq. (1.1) is a superposition state, which means the electron can sit at various positions at the same time. Since the position basis is no special as far as the LVS of a quantum system is concerned, similar superpositions also exist in other basis representations of the state vector. As far as the dynamics of a quantum system is concerned, energy eigenstates are special because the time evolution of a quantum system is governed by the Hamiltonian operator $\hat{H}$ according to the Schrodinger equation

$$i\hbar \frac{\partial\, |s\rangle}{\partial t} = \hat{H}\, |s\rangle\,. \tag{1.3}$$

For a closed system, if the electron state is an energy eigen state, the probability density function $|\psi(x,t)|^2$ will not vary with time and therefore such states are

called stationary states. According to Eq. (1.3), the only change that can happen to a stationary state is the introduction of a linear phase with time. The rate of this phase change depends upon the magnitude of the energy eigen value. Therefore, if the quantum state is prepared in a linear superposition of two energy eigen states say $|\epsilon_1\rangle$ and $|\epsilon_2\rangle$, the time evolution of the state can be written as

$$|s(t)\rangle = e^{i\omega_1 t}\left(|\epsilon_1\rangle + e^{i(\omega_2-\omega_1)t}\,|\epsilon_2\rangle\right)/\sqrt{2} \tag{1.4}$$

where ϵ_1 and ϵ_2 are the energy eigenvalues and $\omega_1 = \epsilon_1/\hbar$ and $\omega_2 = \epsilon_2/\hbar$. The $\sqrt{2}$ in the denominator is to make sure of the normalization condition $\langle s(t)\,|s(t)\rangle = 1$. The expression in Eq. (1.4) can be thought of as two waves interfering each other where the time dependent relative phase, $(\omega_2 - \omega_1)t$ determines the condition for constructive or destructive interference of the individual amplitudes. This ability of quantum states to interfere among themselves is usually referred to as quantum coherence. The coherence of a quantum state is a resource and it could be utilized for representing information in an absolutely non-classical way. A quantum state which is in a coherent superposition of two eigen states of any observable can be treated as a fundamental unit of quantum information. This is called a qubit or a quantum bit. Examples are– spin of an electron, structure of a benzene molecule, path of a single photon in a double–slit experiment ...etc. Yet another non-classical feature of a quantum state is entanglement, which is a property of composite systems to maintain correlation between its parts even when they are far apart from one another. This was initially pointed out by Einstein [1] and was later confirmed by the experiments due to Aspect [2] based on Bell's inequality [3].

1.2 Two-electron System

The total Hamiltonian of a system of two identical particles (excluding the spin degrees of freedom) can be written as

$$H(1,2) = \frac{\mathbf{p}_1^2}{2m} + \frac{\mathbf{p}_2^2}{2m} + V_{\text{pair}}(|\mathbf{x}_1 - \mathbf{x}_2|) + V_{\text{ext}}(\mathbf{x}_1) + V_{\text{ext}}(\mathbf{x}_2). \tag{1.5}$$

where the position and momentum operators necessarily appear in a symmetric manner. This symmetry in the Hamiltonian (with respect to exchange of two particles) will also be present when the spin degrees of freedom are included in the Hamiltonian. This symmetry imposes restriction on the form of the two-particle wave function, namely, the total wave function (with respect to both orbital and spin parts) must be either symmetric or antisymmetric with respect to exchange of the two particles.

In Nature, there are two categories of particles: fermions and bosons. Fermions are particles of half-integral spins and bosons are particles of integral spins. The spin-statistics theorem asserts that the wave function of identical fermions (bosons) must be antisymmetric (symmetric) with respect to exchange of two fermions (bosons). An immediate consequence of the electron being a fermion is that electrons must satisfy the Pauli exclusion principle, which states that no two electrons can occupy the same state.

The Schrodinger equation being linear in the wave function, the state of a two-elctron system can be represented by a linear combination of the form

$$|\psi\rangle = c_1 \, |K'K''\rangle + c_2 \, |K''K'\rangle \tag{1.6}$$

where K' and K'' represent the eigen-values of a complete set of commuting observables (including orbital and spin parts) for each electron.

Since the orbital and spin vector spaces are disjoint spaces (omitting spin-orbit interaction), the total state vector could be expressed as a product of orbital and spin states. For the two electron states, this would demand definite but opposite symmetries for the orbital and spin parts of the state kets. The two-electron spin space is four dimensional with basis spanned by $|\uparrow\uparrow\rangle$, $|\uparrow\downarrow\rangle$, $|\downarrow\uparrow\rangle$ and $|\downarrow\downarrow\rangle$ orthonormal states. Since the original basis states $|\uparrow\downarrow\rangle$ and $|\downarrow\uparrow\rangle$ do not have definite symmetries, we consider $\frac{[|\uparrow\downarrow\rangle - |\downarrow\uparrow\rangle]}{\sqrt{2}}$ and $\frac{[|\uparrow\downarrow\rangle + |\downarrow\uparrow\rangle]}{\sqrt{2}}$ instead of the original basis states. The three spin-symmetric states $|\uparrow\uparrow\rangle$, $|\downarrow\downarrow\rangle$ and $\frac{[|\uparrow\downarrow\rangle + |\downarrow\uparrow\rangle]}{\sqrt{2}}$ are called spin-triplet states and the spin-antisymmetric state $\frac{[|\uparrow\downarrow\rangle - |\downarrow\uparrow\rangle]}{\sqrt{2}}$ is called the spin-singlet state. The total wave function being antisymmetric, the spin-triplet states will be associated with symmetric orbital states. For the same reason, the spin-singlet state has a symmetric orbital counterpart.

In the case of a typical two-electron bound system represented by Eq. (1.5), the terms $V_{\text{ext}}(\mathbf{x}_1)$ and $V_{\text{ext}}(\mathbf{x}_2)$ are the potential energies of the individual electrons due to the confinement potential, whereas, the term $V_{\text{pair}}(|\mathbf{x}_1 - \mathbf{x}_2|)$ in general represents the potential energy due to Coulomb interaction, $e^2/4\pi\epsilon\,|\mathbf{x}_1 - \mathbf{x}_2| = e^2/4\pi\epsilon r_{12}$. The corresponding time-independent Schrodinger equation does not have an exact (closed form) solution. But the solution to a problem which ignores the Coulomb term could be obtained exactly in most of the cases. The orbital part of the this simplified problem can be written as

$$\psi(\mathbf{x}_1, \mathbf{x}_2) = \frac{\varphi_A(\mathbf{x}_1)\varphi_B(\mathbf{x}_2) \pm \varphi_B(\mathbf{x}_1)\varphi_A(\mathbf{x}_2)}{2}, \tag{1.7}$$

where $\varphi_A(\mathbf{x})$ and $\varphi_B(\mathbf{x})$ are the single electron states of the first and second electron. In the above expression, the upper sign corresponds to spin singlet state and the lower sign corresponds to the spin triplet state.

Now, if we treat Coulomb interaction as a perturbation, then the first order correction in energy, ΔE, is given by the expectation value $\langle 1/4\pi\epsilon r_{12}\rangle$. This becomes $C_{\text{d}} + C_{\text{x}}$ and $C_{\text{d}} - C_{\text{x}}$ for the singlet and triplet states, respectively, where

$$C_{\text{d}} = \int d^3x_1 \int d^3x_2 \; |\varphi_A(\mathbf{x}_1)|^2 \, |\varphi_B(\mathbf{x}_2)|^2 \, e^2/4\pi\epsilon r_{12} \tag{1.8}$$

is the direct interaction energy and

$$C_{\text{x}} = \int d^3x_1 \int d^3x_2 \; \varphi_A^*(\mathbf{x}_1)\varphi_B(\mathbf{x}_1)\varphi_B^*(\mathbf{x}_2)\varphi_A(\mathbf{x}_2) \, e^2/4\pi\epsilon r_{12} \tag{1.9}$$

is the exchange interaction energy.

Since the probability density of the space-part of the triplet wavefunction [given by Eq. (1.7)] vanishes when $\mathbf{x}_1 = \mathbf{x}_2$, the value of C_{d} will be minimum for those states. In contrast, C_{d} will have a larger value for the singlet state, due to the enhanced probability of finding electrons at the same point in space.

The important point to notice for a two-electron system is that although the original Hamiltonian is treated as spin independent, the energies are dependent on whether the spins are in a singlet or a triplet state. This feature is further exploited later in the thesis for designing a two-qubit quantum gate.

1.3 Quantum Information Technology

Information technology (IT) deals with gathering, storing, processing and communication of information. It is now well established that no information can exist in an abstract space, but only on the state of a physical system [4]. Let us first review how classical IT is performed. Storing information involves keeping the state of a physical system undisturbed from any external influences. Processing information involves manipulation of these physical states according to our need. For example, the voltage state at the output of a MOS transistor switch can be treated as a bit of digital information. By feeding such voltage states as inputs to appropriate digital gate circuits, we can perform logical operations or information processing. Similarly, an electronic circuit that amplifies or filters an input analog signal is also an example for information processing. Communication of classical information is achieved by utilizing the electromagnetic wave phenomena that can propagate from one point to another. The information is first encoded on an electromagnetic wave by varying any of its parameters such as amplitude, frequency or phase, while launching them into the transmission media. Then by guiding these signals to the desired location, we achieve information transfer. Notice in all the above, macroscopic classical systems and states were utilized.

One of the ways in which present day classical IT is developing is by reducing the size of information processing components year after year. This progression is usually expressed in terms of what is called the Moore's law, which says that in every one-and-a-half year, the number of transistors doubles for a unit chip area. Due to this fact, at this moment we have reached a stage where the dimensions of fundamental devices like transistors are only a few nanometers. At these length scales, quantum mechanics become unavoidable. Quantum effects like tunneling begin to spoil the classical nature of operation of these devices. Therefore, engineers envisage to suppress or compensate for these undesirable quantum effects by clever design techniques [5].

Along a different line of development, many scientists have envisioned to make use of quantum effects to build information processing devices. The idea was independently conceived by two great minds almost at the same time. One was

Feynman who pointed out that the simulation of quantum mechanics on a classical computer may be computationally expensive. To solve this problem, he suggested the possibility of using computation based on quantum mechanics itself [6]. On the other hand, Benioff showed how a classical Turing machine could be simulated by the reversible unitary evolution of a quantum process [7]. Following this, Deutsch described the idea of universal quantum computer, which generalized the classical computational model of universal Turing machines into the quantum regime [8]. He further showed that there exists a class of problems which could be solved more efficiently by quantum computation than by any classical or stochastic methods [9]. These developments have resulted in the beginning of a new era involving quantum information technology, where the information is represented on the states of a quantum system. This has given rise to new degrees of freedom for information storage, processing and communication. For example, in a quantum system, electric currents can go in both directions at the same time in a closed circuit, something not permitted for a classical state of current. Similarly, spins can be up or down at the same time. Because of this new feature, an N-qubit state can in general be prepared as a superposition of 2^N states. Any computation which employs a coherent superposition of quantum state is called quantum computation (QC). The development of large-scale QC research started rapidly after the presentation of the factoring algorithm by Peter Shor [10] and algorithm for searching an unsorted database by Lov Grover [11].

The physical implementation of a quantum computer would require an experimental realization of highly coherent quantum systems, whose time-evolution could be controlled by external means [12; 13]. Apart from coherent superposition, the entanglement in a composite quantum state can also be utilized as a resource in quantum information technology. It helps us to establish a quantum communication link over large distances. Along with a little classical information transfer, this resource enables us to communicate quantum information between two parties [14]. Various quantum cryptographic methods are also proposed to improve the security in transmitting information between two parties [15; 16].

1.4 Semiconductor Quantum Dots

A quantum dot (QD) is a semiconductor nanostructure that confines the motion of conduction band electrons, valence band holes, or excitons (bound pairs of conduction band electrons and valence band holes) in all three spatial directions. The electronic properties of these materials are intermediate between those of bulk semiconductors and of discrete molecules. There are several ways to confine charge carriers in semiconductors, resulting in different methods to produce QDs. First of all, they can be synthesized chemically as colloidal semiconductor nano–particles dispersed in a solution [17]. Typical examples of this are cadmium selenide, cadmium sulfide, indium arsenide, and indium phosphide quantum dots. Secondly we can trap charge carriers via band gap engineering, i.e. by surrounding a low band-gap semiconductor material with a relatively high band-gap material [18; 19]. Coherently strained islands on top of a two-dimensional wetting layer are spontaneously created when a material is grown on a substrate to which it is not lattice matched. This is known as Stranski–Krastanov growth and is achieved using advanced epitaxial techniques such as molecular beam epitaxy (MBE) and metallorganic vapor phase epitaxy (MOVPE). The islands can be subsequently buried to form the QD. Apart from self-organized growth techniques, band-gap engineered QDs can also be grown by artificially patterning the thin film structures. Yet another popular method to fabricate QD is to trap charge carriers in confining potentials created with the help of lithographically patterned gate electrodes [20; 21]. In these QDs, one can electrically control the precise number of electrons by exploiting the Coulomb blockade phenomena [22; 23].

Semiconductor QDs have been studied both experimentally as well as theoretically since the time it became feasible to practically fabricate them [24; 25; 26; 27; 28]. By choosing appropriate materials, shape of the confining potential, geometry of the nanostructure, one can tune the electronic and optical properties of QDs. Therefore they are also known as artificial atoms. QDs have many applications such as to contruct single electron devices [29; 30; 31], single photon sources [32], lasers [33], nano-antennas [34], display color converters [35], bio-medical sensors [36], highly efficient solar cells [37] etc. In Loss-DiVincenzo proposal for quantum computation, coupled quantum dots on a semiconductor substrate form

the platform for spin based quantum information processing [38; 39].

1.5 Loss-DiVincenzo Proposal

In 1998, Daniel Loss and David P. DiVincenzo showed how a coupled quantum dot system could be used for the realization of a scalable quantum computer [38]. The qubit is realized as the spin of the excess electron on a single-electron QD. It has been established that a quantum XOR gate along with single-qubit operations may be assembled to do any quantum computation [40]. Further, the XOR gate can be obtained by a simple sequence of operations

$$U_{XOR} = e^{i\pi/2S_1^z} e^{i\pi/2S_2^z} U_{\text{sw}}^{1/2} e^{i\pi S_1^z} U_{\text{sw}}^{1/2} \tag{1.10}$$

where $e^{i\pi S_1^z}$, etc., are single-qubit operations, which can be realized by applying local magnetic field and $U_{\text{sw}}^{1/2}$ is a two qubit gate called the square root of swap operation. $\vec{S}_1$ and $\vec{S}_2$ are the spin operators corresponding to electron-one and electron-two, and, S_1^z and S_2^z are their z-components. Thus the implementation of a quantum XOR gate is essentially reduced to the implementation of $U_{\text{sw}}^{1/2}$ which is achieved by temporarily coupling the two spins. In the limit $kT << \Delta E$ where ΔE is the level spacing with the higher lying single-particle states of the dots, the interaction between two spins $\vec{S}_1$ and $\vec{S}_2$ can be described by a Heisenberg Hamiltonian

$$H_s(t) = J(t)\vec{S}_1 \cdot \vec{S}_2/\hbar^2. \tag{1.11}$$

For the above Hamiltonian, the time evolution operator can be written as

$$U_s(t) = Te^{-i\int_0^t H_s(t')dt'/\hbar} \tag{1.12}$$

and the evolution of the state vector at time t becomes $|\psi(t)\rangle = U_s(t)\,|\psi(0)\rangle$. Pulsing the exchange interaction between 0 and J_0 for a period τ_s, such that $\int_0^{\tau_s} J(t)dt = J_0\tau_s = \pi$, we achieve two-qubit swap operation U_{sw} so that

$$U_{\text{sw}}\,|ij\rangle = |ji\rangle \tag{1.13}$$

where i, j label the basis states of the two spins in the S_z basis. If the interaction is pulsed on for just half the duration, the resulting two-qubit gate is the required root of the swap operator, $U_{\mathrm{sw}}^{1/2}$.

Many extensions of the original theoretical idea have also been reported. One of the proposal was to use vertically tunnel-coupled quantum dots in the presence of external electric and magnetic fields [41]. The single qubit operation require control over a local magnetic field which introduces substantial complexities into the system. This was shown to be overcome by a modified scheme in which a two-level quantum system based on two-electron spin form the logical qubit [42]. An experimental demonstration of the coherent control over such an encoded qubit is also reported in the literature [43]. It was also demonstrated that a quantum XOR gate operation in an encoded qubit scenario could be achieved via capacitive coupling between two double quantum dots [44]. Some researchers have also considered simultaneous exchange interaction between a larger number of coupled quantum dots [45]. Further, a proposal for long distance exchange interaction based on floating gates was also reported [46]. Apart from such minor variations, there are also other solid-state proposals for quantum computations based on donor-atom nuclear spins and electron spins [47; 48]. Many experimental demonstrations of single and two qubit gate operations were also published [49; 50]. The reading out of final output state is usually achieved by using spin-dependent tunnel rates, where the spin states are first correlated to different charge states [51].

1.6 Decoherence

The experimental realization of a quantum computer is extremely challenging. There are five major criteria to be satisfied. Since the basic units of the theory are qubits, first of all we require a scalable two-level quantum system. In the Loss-DiVincenzo proposal, this is achieved easily by using the inherently two-dimensional Hilbert space of individual electron spin. Secondly, we should have the ability to achieve desired evolution of the quantum system. In the aforesaid proposal, this is achieved via electrically controlling the exchange interaction between electrons in the coupled quantum dots. Thirdly, one should be able to

prepare qubits in some specified set of initial states and fourthly, we should be able to measure the final output state of the system. It is hard to find all the above four criterion satisfied in a single physical system. Finally, it is hard to build quantum computers because the quantum nature of a physical state (especially the superposition state) is always subjected to influences from outside the system. These environmental interactions in effect perform a measurement operation which will result in the destruction of superposition states. This process of losing quantum coherence in a physical system through environmental interactions is called decoherence. Meeting this (fifth) criterion of decoherence free QC is identified as the biggest challenge in the physical realization of any quantum computer [52].

Decoherence can be viewed as a loss of information from a system into the environment, since the system is loosely coupled with the state of its surroundings and entanglement between the both are generated. Though the combined system plus environment evolves in a unitary fashion, viewed in isolation, the system's dynamics are non-unitary. Since the microscopic state of the environment is inaccessible to us, the phenomenon of decoherence is irreversible. Decoherence is an extremely fast process for macroscopic objects since the number of degrees of freedom of the environment interacting with such objects is very high. This also explains why quantum behaviors are not observed in everyday macroscopic objects. The theory of decoherence is usually expressed in terms of density matrix formalism of quantum mechanics. The characteristic time it takes for a physical state to lose its quantum properties is called decoherence time. In the gate circuit model of quantum computation, the time it takes to execute a quantum algorithm must be many orders of magnitude lesser than the decoherence time for error-free quantum computation.

1.7 Outline of the Thesis

The content of the thesis is organized as follows.

In Chapter 2, we present detailed results of the calculation for single electron states in a cylindrical quantum dot in the presence of a constant magnetic field in the axial direction. The quantum dot structure considered is with a finite

barrier potential in the radial direction and infinite barrier potential in the z-direction. We show how the states and energy levels depend on the strength of the magnetic field for different quantum numbers. It is observed that energy levels with different quantum numbers group together at high magnetic fields.

In Chapter 3, we study the confinement of a single electron in hydrogenic impurity potential in the presence of a magnetic field. The analysis is done by approximating the system into a quasi-two dimensional problem. The Schrodinger equation is solved numerically using finite difference method based on Numerov's shooting algorithm. The results show that the ground state energy level is well separated from all other excited states and the corresponding wavefunction is insensitive to lower magnetic field strengths. On the other hand, higher energy levels are significantly compressed in the presence of magnetic fields.

In Chapter 4, we present the results obtained for the problem of two electrons in a cylindrical quantum dot with finite step potential in the presence of an orthogonal magnetic field. The method we adopt is linear variational theory, where the basis states are constructed from single electron eigenfunctions of the harmonic oscillator potential. We show how the two electron energy levels vary with the magnetic field for various quantum numbers. Magnetization of the system is then calculated after determining its free energy at a non–zero temperature. Finally, we also plot the electron density and pair correlation function for various quantum numbers and field strengths.

In Chapter 5, we consider two electrons in a laterally coupled quantum dots in the presence of an orthogonal magnetic field. In this chapter, we consider two separate cases. The first case involves the study of exchange interaction between electrons confined by a cylindrical step potential. The second case involves exchange interaction for coupled hydrogenic impurity potential. In both cases, we evaluate the exchange coupling constant as a function of external magnetic field strength. The theoretical tools used are Heitler-London method and Weinbaum method, the latter being a refined method that takes account of the double-occupancy states in each dots. The results show that we could switch the exchange interaction ON and OFF by switching external magnetic field between two magnitudes. Finally, considering an adiabatic switching of exchange interaction, we also estimate the time required for fundamental gate operation according

to the Loss-DiVincenzo proposal.

In Chapter 6, using a simple model of central spin interacting with a spin bath, we study the decoherence of single electron spin states in a quantum dot within one, two and three dimensional nanostructure geometries. We consider a one–component hyperfine interaction term and express its strength as a smooth function of position vector. Decoherence measures are evaluated and plotted for various initial states, and we notice a decrease in decoherence time with the reduction of spin bath dimension.

In Chapter 7, we extend the above model to study the decoherence of two interacting spin qubits in the presence of a nuclear spin bath. The interaction between qubits are modeled using Heisenberg's effective Hamiltonian. The interaction between the qubits and the nuclear bath are treated to be of Ising type. Whether both qubits are interacting with the same bath configuration is determined by the correlation between single particle electron probability density function for each electron. We evaluate the dynamics of decoherence and entanglement between qubits for various initial states of the spin qubits.

Finally, in Chapter 8, the thesis is concluded with final remarks on the results obtained and possible future extensions of the work presented. In Appendix A, the values of all the constants used to evaluate the strength of hyperfine interaction are listed. Appendix B lists the publications from this thesis work. References cited in all chapters of the thesis are listed at the end.

Chapter 2

Single electron in a cylindrical quantum dot potential

2.1 Introduction

Semiconductor quantum dots are a potential platform for building single electron devices [31; 53] and solid-state based quantum information technologies [38; 39; 41; 44; 45]. Utilizing the Coulomb blockade phenomena, it is now possible to precisely control the number of electrons in such dots. Most of these proposals employ band gap engineering to create a thin sheet of 2D electron gas which is then confined further through in-plane metallic gate electrodes to form the dot potential [43; 49; 54]. The in-plane variation of the potential in such dots is parabolic in nature to a very good approximation. Thus the single electron states of a parabolic quantum dot are employed in the detailed analysis of such devices. One way of achieving control in the operation of these devices is by varying the strength of constant external magnetic field. The eigen states and energy of a parabolic confinement in magnetic field were initially derived by Fock [55] and it is reproduced with details in reference [26].

The recent advancements in semiconductor fabrication technology [56; 57; 58] suggest the possibility of making fully hetrostructured quantum dot in a controlled fashion. For these reasons, it is of interest to theoretically explore the possibilities of employing such dots with different shapes and dimensions for the

above mentioned device applications. Some of such explorations which employ cylindrical quantum dot structure in the presence of a magnetic field are listed in the references [59; 60; 61; 62]. These make use of the single electron ground state of a cylindrical quantum dot in magnetic field for constructing the trial wave function in their respective variational analysis. The derivation of single-electron states of a cylindrical quantum dot with infinite wall potential boundary in a magnetic field was first reported by Rensink [63]. This result is then extended to finite boundary case by Bajaj et al. [64; 65] as a part of their analysis on the hydrogenic donor states in such dots. In this chapter, we revisit the problem and present the detailed results of calculations for different eigen states and their dependence on the magnetic field strength. In what follows, we present the same with the detailed theory in section 2.2, discussion of results in section 2.3 and conclusion in section 2.4. Similar to the case of parabolic quantum dot, we find that the energy levels with a certain combinations of quantum numbers are grouped together at high magnetic field strength.

2.2 Theory

We do our analysis for a fully hetrostructured cylindrical quantum dot made out of GaAs/Al_xGa_{1-x}As material. The shape and dimensions of such a dot is schematically shown in Fig.2.1. The thickness of the structure everywhere is taken as d_z. The potential barrier height, and substrate effective mass, depend on the Al concentration, x as, $V_0 = Q_e(1.36x+0.22x^2)$ and $m_s = m_d+0.083x\, m_0$ [64; 65]. Here, $Q_e = 0.6$, m_d is the electron effective mass inside the dot, and m_0 is the free-electron mass. We have fixed the value of V_0 to be 100 meV. This corresponds to $x = 0.1202$ and $m_s = 0.077\, m_0$, where we have used $m_d = 0.067\, m_0$. The complete potential profile of the dot-structure as shown in Fig. 2.1, can be written as

$$V(r,\phi,z) = V(r,z) = \begin{cases} 0, & \text{for } r \le r_0 \text{ and } 0 \le z \le d_z; \\ V_0, & \text{for } r > r_0 \text{ and } 0 \le z \le d_z; \\ \infty, & \text{otherwise.} \end{cases} \tag{2.1}$$

Within the framework of the effective mass approximation, the Hamiltonian of

the above system with a single electron in the presence of a constant magnetic field in the z-direction takes the form

$$\hat{H} = \left(-i\hbar\vec{\nabla} + q\vec{A}\right)\frac{1}{2m(r)}\left(-i\hbar\vec{\nabla} + q\vec{A}\right) + V(r,z) \tag{2.2}$$

where q is the charge of the electron, $\frac{1}{m(r)} = \frac{1}{m_d}\theta(r_0 - r) + \frac{1}{m_s}\theta(r_0 - r)$, the electron effective mass function, and $\vec{A}(r,\phi,z) = \frac{B}{2}r\mathbf{e}_\phi$ is the vector potential for the magnetic field $\vec{B} = B\,\mathbf{e}_z$.

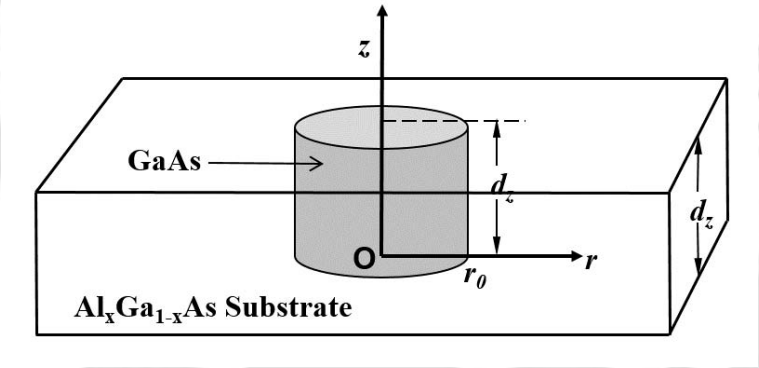

Figure 2.1: Cylindrical quantum dot potential

The corresponding time-independent Schrodinger equation in cylindrical coordinates becomes

$$-\frac{\hbar^2}{2}\left\{\frac{1}{m(r)}\frac{\partial^2\Psi}{\partial r^2} + \left(\frac{1}{m(r)}\frac{1}{r} - \frac{m_s - m_d}{m_s m_d}\delta(r - r_0)\right)\frac{\partial\Psi}{\partial r} + \frac{1}{m(r)r^2}\frac{\partial^2\Psi}{\partial\phi^2} + \frac{1}{m(r)}\frac{\partial^2\Psi}{\partial z^2}\right\}$$
$$-\frac{i\hbar\omega_c}{2}\frac{\partial\Psi}{\partial\phi} + \left(\frac{m(r)\omega_c^2}{8}r^2 + V(r,z)\right)\Psi = E\Psi \tag{2.3}$$

where $\omega_c = qB/m(r)$ is the electron cyclotron frequency and it also is a function of r. Defining $\hat{H} = \hat{H}_0 + \hat{H}'$, where

$$\hat{H}' = \hbar^2\frac{m_s - m_d}{2m_s m_d}\delta(r - r_0)\frac{\partial}{\partial r} \tag{2.4}$$

is treated as a perturbation to the unperturbed system described by the equation

$$\hat{H}_0\psi = E_0\psi. \tag{2.5}$$

The potential $V(r,z)$ can be expressed as a sum of two terms, $V_R(r)$ and $V_Z(z)$, given by

$$V_R(r) = \begin{cases} 0, & r \le r_0; \\ V_0, & r > r_0. \end{cases} \text{ and, } V_Z(z) = \begin{cases} 0, & 0 \le z \le d_z; \\ \infty, & \text{otherwise.} \end{cases} \tag{2.6}$$

Nevertheless, due to the radial dependence of the effective mass, this does not guarantee a variable separable solution for Eq. (2.5). But we can consider product form of solution separately for regions with constant effective masses as

$$\psi(r,\phi,z) = \begin{cases} \Lambda_1(r,\phi)\Sigma_1(z), & ; r \le r_0 \\ \Lambda_2(r,\phi)\Sigma_2(z), & ; r > r_0. \end{cases} \tag{2.7}$$

Thus we get,

$$\begin{aligned} \left\{ \frac{\partial^2}{\partial r^2} + \frac{1}{r}\frac{\partial}{\partial r} + \frac{1}{r^2}\frac{\partial^2}{\partial \phi^2} + \frac{im(r)\omega_c}{\hbar}\frac{\partial}{\partial \phi} - \left(\frac{m(r)\omega_c}{2\hbar}\right)^2 r^2 \right\} \Lambda_j(r,\phi) \\ + \frac{2m(r)}{\hbar^2}\left[E_0 - E_{Zj} - V_R(r)\right]\Lambda_j(r,\phi) = 0 \end{aligned} \tag{2.8}$$

where $j = 1(2)$ stands for region inside (outside) the dot, E_{Zj} is the eigen value of the following equation in z coordinate.

$$\left\{ \frac{d^2}{dz^2} + \frac{2m(r)}{\hbar^2}[E_{Zj} - V_Z(z)] \right\} \Sigma_j(z) = 0 \tag{2.9}$$

As $V_Z(z) = \infty$ for the region $z < 0$ and $z > d_z$, we impose the boundary condition $\Sigma(0) = \Sigma(d_z) = 0$, and the normalized solution for Eq. (2.9) becomes

$$\Sigma_j(z) = \sqrt{\frac{2}{d_z}} \sin\left(\frac{k\pi z}{d_z}\right); \text{and } E_{Zj} = \frac{k^2\pi^2\hbar^2}{2m(r)d_z^2}; \text{where}, k = 1, 2, 3, ... \tag{2.10}$$

Notice here that the wavefunction $\Sigma_j(z)$ remains the same for $j = 1$ and 2 thus ensuring continuity conditions at the boundary, whereas the corresponding quan-

tized energy varies between inside and outside of the quantum dot. Since the total energy of any energy eigen state must be constant, the contribution to energy from other degrees of freedom must adjust accordingly. As $-i\hbar\frac{\partial}{\partial\phi} = \hat{L}_z$ is the z-component of the angular momentum operator of the electron and since it commutes with the two-dimensional Hamiltonian in Eq. (2.8), we try a product solution $\Lambda_j(r,\phi) = R_j(r)e^{il\phi}/\sqrt{2\pi}$ and obtain

$$r^2\frac{d^2R_j}{dr^2} + r\frac{dR_j}{dr} - \left\{\gamma^2r^4 + \beta_j(E_0)\,r^2 + l^2\right\}R_j(r) = 0 \tag{2.11}$$

where

$$\gamma = \frac{m(r)\omega_c}{2\hbar} = \frac{qB}{2\hbar}$$

and

$$\beta_j(E_0) = \frac{2m(r)}{\hbar^2}\left(V_R(r) + E_{Zj} + \frac{\hbar\omega_c l}{2} - E_0\right).$$

Substituting $r = \sqrt{y/\gamma}$ in Eq. (2.11), so that $R_j\left(\sqrt{y/\gamma}\right) = G_j(y)$, we get

$$\frac{d^2G_j}{dy^2} + \frac{1}{y}\frac{dG_j}{dy} - \frac{1}{4}\left(1 + \frac{\beta_j/\gamma}{y} + \frac{l^2}{y^2}\right)G_j(y) = 0 \tag{2.12}$$

.

Considering the asymptotic solutions for the above equation as in [66] and page 461 of [67], we substitute $G_j(y) = y^{|l|/2}e^{-y/2}F_j(y)$. Thus, Eq. (2.12) becomes

$$y\frac{d^2F_j}{dy^2} + (|l|+1-y)\frac{dF_j}{dy} - \left(\frac{1+|l|}{2} + \frac{\beta_j}{4\gamma}\right)F_j(y) = 0 \tag{2.13}$$

The final equation is in the form of standard confluent hypergeometric differential equation

$$y\frac{d^2F_j}{dy^2} + (c-y)\frac{dF_j}{dy} - a_jF_j(y) = 0 \tag{2.14}$$

whose complete solution for the case of $c \geq 1$ is given in [68] as

$$F_j(y) = A_jM(a_j;c;y) + B_jU(a_j;c;y) \tag{2.15}$$

where $M(a_j;c;y)$ and $U(a_j;c;y)$ are the confluent hypergeometric functions of

the first and second kind, respectively, and $a_j = (1+|l|)/2+\beta_j/4\gamma$ and $c = |l|+1$. Thus, the solution for Eq. (2.11) becomes

$$\begin{aligned} R_1(r) &= r^{|l|}e^{-\gamma r^2/2}\left[A_1\, M(a_1;|l|+1;\gamma r^2) + B_1\, U(a_1;|l|+1;\gamma r^2)\right] \\ R_2(r) &= r^{|l|}e^{-\gamma r^2/2}\left[A_2\, M(a_2;|l|+1;\gamma r^2) + B_2\, U(a_2;|l|+1;\gamma r^2)\right] \end{aligned} \tag{2.16}$$

where

$$\begin{aligned} a_1 &= \frac{1+|l|+l}{2} + \frac{k^2\pi^2\hbar}{2d_z^2 qB} - \left(\frac{m_d}{\hbar qB}\right)E_0 \\ a_2 &= a_1 + \frac{m_s}{\hbar qB}\left[\left(\frac{m_d}{m_s}-1\right)E_0 + V_0\right]. \end{aligned} \tag{2.17}$$

Since $r^{|l|}e^{-\gamma r^2/2}U(a_1;|l|+1;\gamma r^2)$ and $r^{|l|}e^{-\gamma r^2/2}M(a_2;|l|+1;\gamma r^2)$ diverge for $r\to 0$ and $r\to\infty$ respectively, we set $B_1 = A_2 = 0$. Thus the required solution of Eq. (2.5) after applying the continuity of the wave function condition at $r = r_0$ and the substitution $A_1 = C_0/M(a_1;1+|l|;\gamma r_0^2)$, becomes

$$\psi(r,\phi,z) = C_0\, r^{|l|}e^{-\gamma r^2/2}e^{il\phi}\sin(k\pi z/d_z)\begin{cases} \frac{M(a_1;|l|+1;\gamma r^2)}{M(a_1;|l|+1;\gamma r_0^2)}; & r\le r_0 \\ \frac{U(a_2;|l|+1;\gamma r^2)}{U(a_2;|l|+1;\gamma r_0^2)}; & r > r_0 \\ 0; & \text{elsewhere.} \end{cases} \tag{2.18}$$

Here, the value of parameter a_1 is determined by matching the value of $\frac{\partial\psi}{\partial r}$ at $r = r_0$. Correspondingly, we get

$$\left(\frac{a_1}{|l|+1}\right)\frac{M(a_1+1;|l|+2;\gamma r_0^2)}{M(a_1;|l|+1;\gamma r_0^2)} = -a_2\frac{U(a_2+1;|l|+2;\gamma r_0^2)}{U(a_2;|l|+1;\gamma r_0^2)}. \tag{2.19}$$

The above equation is solved numerically for a given value of k and l to evaluate a_1 and the corresponding bound states are indexed as $n = 0, 1, 2, ...$ in the increasing order of energy, E_0, whose expression in the general form can be written from Eq. (2.17) as

$$E_0^{n\,l\,k} = \frac{\hbar qB}{m_d}\left(\frac{1+|l|+l}{2} - a_1\right) + \frac{k^2\pi^2\hbar^2}{2m_d d_z^2} \tag{2.20}$$

or equivalently,

$$E_0^{n\,l\,k} = \frac{\hbar qB}{m_s}\left(\frac{1+|l|+l}{2} - a_2\right) + V_0 + \frac{k^2\pi^2\hbar^2}{2m_s d_z^2}. \tag{2.21}$$

The indices $n = 0, 1, 2, ...,\ l = 0, \pm1, \pm2, ...$ and $k = 1, 2, 3, ...$ are the radial, azimuthal and z quantum numbers respectively. The value of quantum number n corresponds to the number of nodes in the radial part of the wave function.

Once the value of a_1 is obtained for a given set of quantum numbers (n, l, k), the final step is to normalize the resulting wavefunction. This is done by evaluating the constant C_0 in Eq. (2.18) by integrating the probability amplitude throughout the region where the function value is non-zero, i.e.

$$\int_{r=0}^{\infty}\int_{\phi=0}^{2\pi}\int_{z=0}^{d_z}|\psi|^2 r\, dr\, d\phi\, dz = 1 \tag{2.22}$$

To find the approximate value of energy eigen value, E of the original problem given in Eq. (2.3), we apply first order perturbation theory. The first order correction in energy for a state ψ_{nlk} which is non-degenerate is given by

$$\Delta E^{nlk} = \int_{r=0}^{\infty}\int_{\phi=0}^{2\pi}\int_{z=0}^{d_z}\psi^*_{nlk}\hat{H}'\psi_{nlk}\, r dr d\phi dz \tag{2.23}$$

where the expression for $\hat{H}'$ is as given in Eq. (2.5). Thus the approximate value of unknown energy $E^{nlk} \cong E_0^{nlk} + \Delta E^{nlk}$. This approximation can be considered proper only if the value of ΔE is negligible in comparison to that of E_0.

2.3 Results and Discussion

We solved Eq. (2.19) numerically using Mathematica software [69]. Here, the values of a_1 are found by determining the crossing points of the function on the left hand side (L.H.S.) and right hand side (R.H.S.) of Eq. (2.19). A plot of these functions for a quantum dot with $r_0 = 50$ nm and, $B = 8$ Tesla is shown in Fig. 2.2. The effect due to the difference in the effective mass of the electron enters into these plots via a_1 and a_2 in Eq. (2.17). If we ignore the differences in the effective mass, the expression for a_2 reduces to $a_1 + \frac{V_0}{\hbar\omega_c}$. The results in both cases are more or less the same. The only variation we could observe was a slight change in the wave functions near the potential wall. At large magnetic fields, we noticed that the asymptotes in the L.H.S. function align with integer

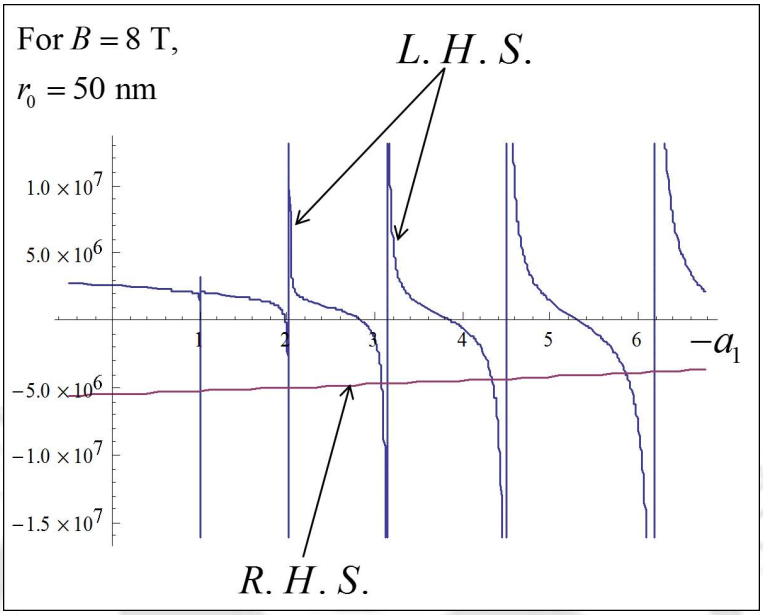

Figure 2.2: Graphical plot of L.H.S. and R.H.S. of Eq. (2.19) as a function of a_1

values starting from 0 and they cut the R.H.S. function almost perpendicularly. This results in a modification of the radial part of eigen energies, $E_0^{nl} = E - E_Z$, as expressed below.

$$E_0^{nl}\,(\text{at high } B \text{ field}) = \hbar\omega_c \left[n + \frac{1 + |l| + l}{2} \right] \tag{2.24}$$

The above energy levels correspond exactly to the diamagnetic free electron levels discussed in references [66; 67; 70; 71]. The variation of probability density of a few lower states in the radial direction for a dot size of 40 nm for two magnetic field intensities is plotted in Fig. 2.3. These results are plotted up to a radial distance of $1.2r_0$ for a value of barrier potential $V_0 = 100$ meV. The number of bounded states is determined collectively by the values of V_0, r_0, and $\vec{B}$. The result shows that, at high magnetic fields, the states are confined more and more toward the centre of the dot. This effect is prominent at large dot diameters and it clearly demonstrates the dominating role of confinement due to magnetic field over the confinement due to the dot-potential at high magnetic fields. The variation of different energy levels with magnetic field $\vec{B}$ for quantum dots with radii $r_0 = 40$ nm and $r_0 = 20$ nm are plotted in Fig. 2.4 (a) and

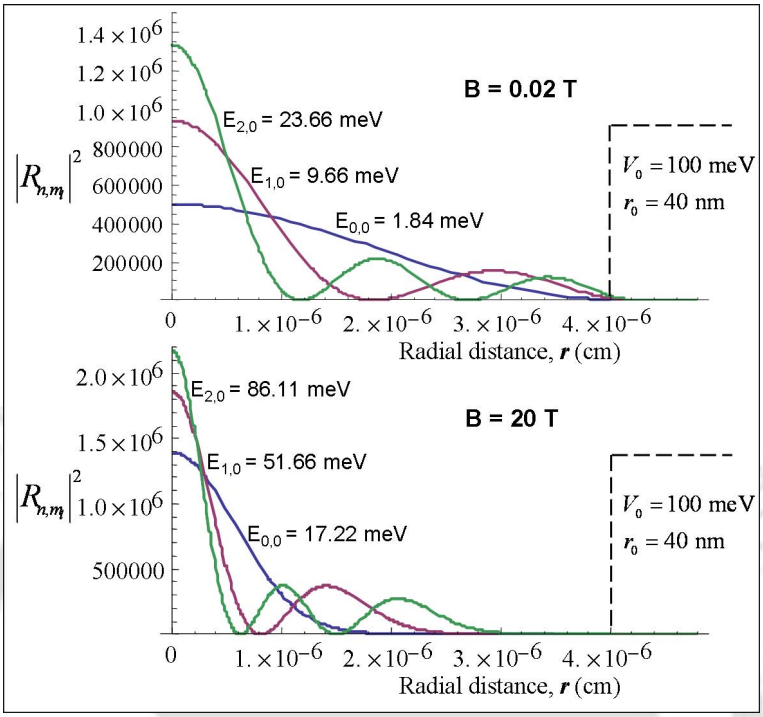

Figure 2.3: Variation of electron probability density with magnetic field strength

(b) respectively. The energy level values for the states with the same quantum numbers increase with the decrease of the dot radius. This follows directly from the uncertainty principle as the uncertainty of the electron momentum increases, thereby increasing its energy, with the decrease of position uncertainty due to the cylindrical wall confinement. But at high magnetic fields, such differences due to dot diameters vanish, as can be seen from Fig. 2.4, due to quicker increase of energy levels with magnetic field strength in the case of large dot diameters. The degeneracies are lifted for sufficiently high magnetic field. We also noticed a grouping of energy levels at high magnetic field as per Eq. (2.24) for different combinations of n and l values. The values of E_0^{nl} are grouped to $\hbar\omega_c(n+1/2)$ when l is negative and to $\hbar\omega_c(n+l+1/2)$ when l is positive. Here, ω_c is the cyclotron frequency and it is directly proportional to the strength of the magnetic field. For a large diameter dot, grouping of energy levels happens immediately with the increase of the magnetic field strength. This can be verified by comparing part (a) and (b) of Fig. 2.4. Similar variations and groupings of energy levels with

magnetic field strength were already reported in the case of parabolic quantum dots [26]. There, the threshold value of magnetic field strength at which the energy levels tend to diamagnetic levels is determined by the frequency of the harmonic oscillator potential. In contrast, it is determined by the dot radius for cylindrical quantum dots.

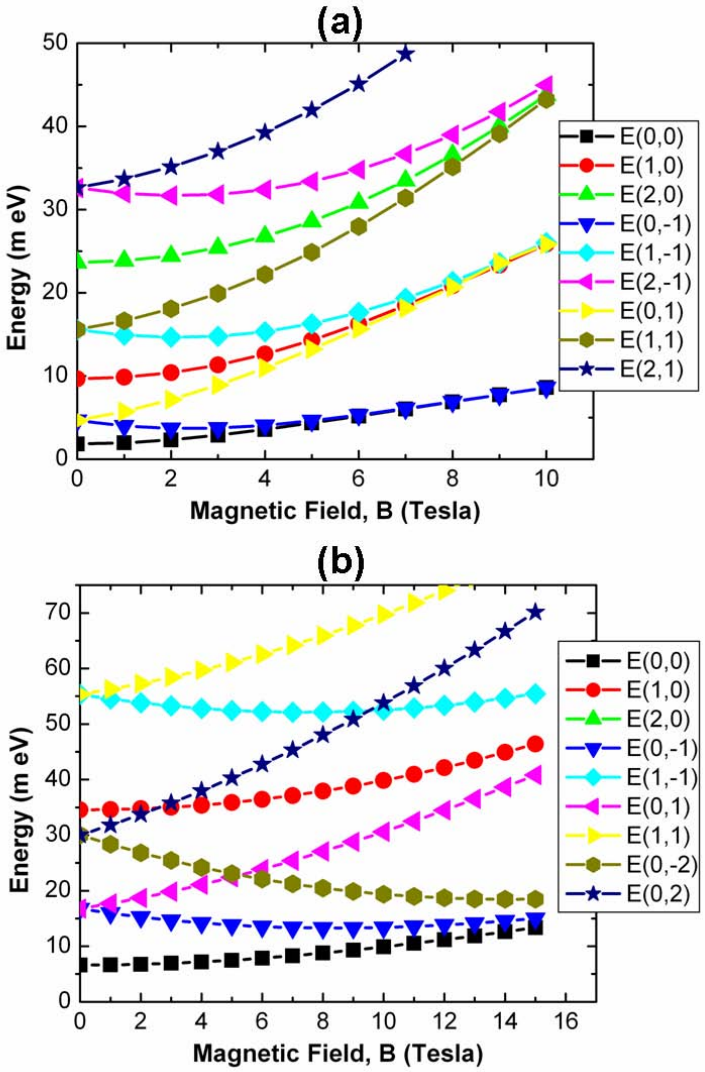

Figure 2.4: Variation of radial energy levels with magnetic field strength for quantum dot with radius (a) 40nm and (b) 20nm. The legend is shown in the format $E_0(n, l)$.

In the above analysis we have not included the effect of Zeeman interaction, whose energy contribution depends on the orientation of spin along the z direction and is given by

$$E_Z = \pm g\mu_B B/2 \tag{2.25}$$

where $g = 2$ is the electron g-factor, μ_B is the Bohr magneton and B is the applied magnetic field strength. This splitting is explicitly shown in Fig. 2.5.

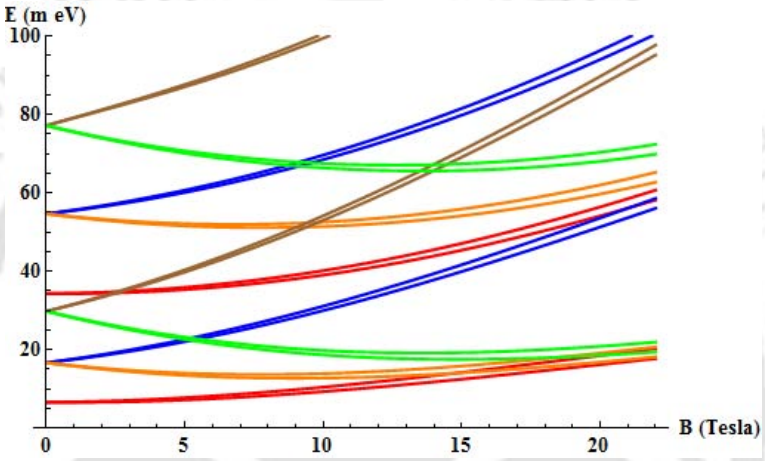

Figure 2.5: Splitting of single electron energy levels due to Zeeman interaction for a QD with $r_0 = 20$nm.

We have also calculated the first order correction in energies for the ground state energy level for various values of magnetic fields and quantum dot radii. Omitting the vertical dimension, the ground state of single electron cylindrical quantum dot for $r \leq r_0$ can be written as

$$\psi_0(r,\phi) = C' e^{-\frac{\gamma}{2}r^2} M(a_1; 1; \gamma r^2) \tag{2.26}$$

where C' is the normalization constant of the wavefunction in $r-\phi$ plane and all other factors are as defined before.

$$\frac{\partial \psi_0}{\partial r} = C'\gamma r e^{-\frac{\gamma}{2}r^2} \left\{ -M(a_1; 1; \gamma r^2) + 2a_1 M(a_1+1; 2; \gamma r^2) \right\} \tag{2.27}$$

Substituting these in the first order correction term

$$\Delta E^{00} = \hbar^2 \frac{(m_s - m_d)}{2m_s m_d} \int_{\phi=0}^{2\pi} \psi_0^* \frac{\partial \psi_0}{\partial r} r d\phi|_{r=r_0} \tag{2.28}$$

we get the following energy corrections for a quantum dot with radius $r_0 = 15$nm.

	$B = 0$T	$B = 5$T	$B = 10$T	$B = 15$T	$B = 20$T
E_0^{00} (meV)	10.954	11.493	13.06	15.502	18.640
ΔE^{00} (meV)	-0.370	-0.356	-0.314	-0.255	-0.191
% change	3.38	3.10	2.41	1.65	1.03

It may be seen from the above table that the energy corrections are lesser than 3.40% of the unperturbed energy values. It becomes even more negligible at higher magnetic fields. The effect of perturbation also reduces with larger quantum dot radius. This can be verified from the results shown below where r_0 =20nm.

	$B = 0$T	$B = 5$T	$B = 10$T	$B = 15$T	$B = 20$T
E_0^{00} (meV)	6.601	7.477	9.893	13.356	17.356
ΔE^{00} (meV)	-0.174	-0.154	-0.106	-0.058	-0.025
% change	2.64	2.06	1.07	0.43	0.14

2.4 Conclusion

In view of the second quantum revolution [72], we have presented a comprehensive report on the derivation of the single electron states for a cylindrical quantum dot in the presence of constant magnetic field in transverse direction. The quantum dot structure considered was with finite barrier potential in the radial direction and infinite barrier potential in the z-direction. The eigen energy values are determined numerically by exploring the continuity relations of the wave functions at the boundary. The radial variation of the probability density for a few low lying states is plotted with different dot sizes and magnetic field strengths. We noticed a prominent compression of these states for larger dots at high magnetic field. The radial part of the energy values for different states are plotted as a function of magnetic field $\vec{B}$. We noticed the grouping of energy levels at high magnetic field strengths which may be attributed to the domination of diamagnetic effect over the barrier confinement.

Chapter 3

Single electron in hydrogenic impurity potential

3.1 Introduction

Nanostructures with hydrogenic impurity is a problem that has been studied by many researchers since the time the technology to build such structures became feasible [73; 74; 75; 76]. Such structures are useful for building hardware for quantum gate operations [47; 48]. These systems are also interesting from the fundamental science point of view. Because in such structures one can study how the parameters of confining potential modify the properties of electron donated by the impurity atom. The spectrum and binding energy [77; 78], optical characteristics [79; 80], effects of electric and magnetic fields [81; 82] are a few to mention. hydrogenic impurity inside non-linear as well as non-isotropic host materials were also considered by some authors [83; 84]. As can be seen in these references, the nanostructures mostly studied in the context of hydrogenic impurities were quantum wells, quantum wires and quantum dots (QD) with spherical, cylindrical, box confinements. Donor impurities in quantum rings were also studied recently [85]. As analytical solutions do not exist in most of the cases, the theoretical studies were mostly performed using variational analysis [64; 65]. In some of the cases, the system can be approximately treated as a two-dimensional problem. In such cases, the problem can be treated like a two-dimensional hydro-

gen atom [86; 87]. A hydrogenic impurity will result in a logarithmic potential in a strictly two-dimensional world due Gauss's law in two dimensions. Such a problem was studied numerically a few decades ago [88]. But for a practically two-dimensional system, such as in the case of a two-dimensional quantum disc problem, $1/r$ potential is more appropriate, since all the electric flux from the positive nucleus is not confined in the two-dimensional plane. In what follows, we numerically solve the problem of hydrogenic impurities in two-dimensions in the presence of a magnetic field orthogonal to the 2D plane.

This chapter is organized as follows. In Section 3.2, we present the theoretical model and then discuss various numerical procedures to solve the eigen value problem. The results obtained such as energy eigen states and their variation with respect to magnetic flux densities are analyzed in Section 3.3. Finally the chapter is concluded in Section 3.4.

3.2 Theory and Numerical Procedure

We consider a thin sheet of GaAs material in which a hydrogenic impurity is placed at the origin. The impurity will donates a single electron into the lattice which will be confined by the nuclear potential. The confinement in axial direction of the disc is assumed to be much stronger than that in the plane of the disc and therefore the system can in effect be treated as a quasi two-dimensional structure. Our aim in this study is to find out how the energy levels of such a system is modified by the presence of an external magnetic field in the perpendicular direction.

The single electron Hamiltonian of the present system can be written as,

$$H = \frac{1}{2m_e^*}\left(\vec{p} + q\vec{A}\right)^2 - \frac{q^2}{\kappa\, r} \tag{3.1}$$

where $\kappa = 4\pi\epsilon_0\epsilon_r$ with $\epsilon_r = 13.1$ (for GaAs). Here m_e^* is the effective mass of electron in GaAs material, which is $0.067m_0$, where m_0 is the rest mass of the electron, and q is the charge of the electron, and $\vec{A}(r,\phi) = \frac{B}{2}(0,r)$ is the magnetic vector potential corresponding to a constant magnetic field $\vec{B} = B\hat{e}_z$. The corresponding time-independent Schrodinger equation in polar coordinates

becomes

$$-\frac{\hbar^2}{2m_e^*}\left\{\frac{\partial^2\psi}{\partial r^2}+\frac{1}{r}\frac{\partial\psi}{\partial r}+\frac{1}{r^2}\frac{\partial^2\psi}{\partial\phi^2}\right\}-\frac{i\hbar\omega_c}{2}\frac{\partial\psi}{\partial\phi}+\left(\frac{m_e^*\omega_c^2}{8}r^2-\frac{q^2}{\kappa\, r}\right)\psi=E\psi \quad (3.2)$$

As in Section 2.2, since $\hat{L}_z$ commutes with the two-dimensional Hamiltonian in Eq. (3.2), we try a product solution $\psi(r,\phi)=R(r)e^{i\,l\phi}/\sqrt{2\pi}$, where $l=0,\pm1,\pm2,...$ and obtain

$$-t_0\left\{\frac{d^2R}{dr^2}+\frac{1}{r}\frac{dR}{dr}\right\}+\left[t_1r^2+t_2\frac{l}{2}-\frac{t_3}{r}+\frac{t_0l^2}{r^2}\right]R(r)=ER(r) \quad (3.3)$$

where $t_0=\frac{\hbar^2}{2m_e^*}$; $t_1=\frac{1}{2}m_e^*(\omega_c/2)^2$; $t_2=\hbar\omega_c$; $t_3=q^2/\kappa$ and $\omega_c=\frac{qB}{m_e^*}$.

The above equation has no analytically exact solutions. But they are available for certain values of magnetic field strengths for a given set of radial and azimuthal quantum numbers [89]. A solution for intermediate magnetic field strength in the form of a uniformly convergent Taylor series has also been reported in a case related to our present problem [90].

In the following, we solve Eq. (3.3) using numerical methods, where the unknown function $R(r)$ is evaluated at discrete points. Before proceeding further, we remove the first order term from the above differential equation as most of the numerical methods can be directly applied to differential equations that has only second order derivatives. Thus we use a substitution $R(r)=r^{-1/2}f(r)$ and obtain

$$-t_0\left\{\frac{d^2}{dr^2}+U(r)\right\}f(r)=Ef(r) \quad (3.4)$$

where

$$U(r)=\left[t_1r^2+t_2\frac{l}{2}-\frac{t_3}{r}+\frac{t_0(l^2-1/4)}{r^2}\right].$$

In the following subsections we outline the procedures employed in various finite difference methods (FDM). With proper substitutions, we could extend this method for solving problems on a non-linear grid also.

3.2.1 Matrix Method

In all FDM based methods, we discretize the given differential equation using a regular interval grid of N points. i.e. the values of independent variable and all its associated functions are indexed using integers, like $r_i = i\,\Delta$, where i runs from 1 to N and $\Delta = r_{\max}/N$. Here $r_{\max}$ is a sufficiently large value of r where the wavefunction for all practical purposes can be taken to be zero. The boundary conditions $f(0) = f(\infty) = 0$ are numerically imposed by setting $f(r_0) = f(r_{N+1}) = 0$. Substituting the central difference approximation formula for second derivative and sampling the value of $U(r)$ at the grid points, Eq. (3.4) at $r = r_i$ becomes

$$-t_0\left[\frac{f_{i-1} - 2f_i + f_{i+1}}{\Delta^2}\right] + U_i f_i = E f_i \tag{3.5}$$

where, $f_i = f(r_i)$ and $U_i = U(r_i)$. Writing similar equation for all value of i and applying the boundary condition, Eq. (3.4) becomes an $N \times N$ matrix eigen value problem where the operator part is a tri-diagonal matrix as shown below.

$$\begin{bmatrix} \frac{2t_0}{\Delta^2} + U_1 & -\frac{t_0}{\Delta^2} & \cdots & \cdots & 0 \\ -\frac{t_0}{\Delta^2} & \frac{2t_0}{\Delta^2} + U_2 & -\frac{t_0}{\Delta^2} & \cdots & 0 \\ \vdots & \ddots & \ddots & \ddots & \vdots \\ 0 & \cdots & -\frac{t_0}{\Delta^2} & \frac{2t_0}{\Delta^2} + U_{N-1} & -\frac{t_0}{\Delta^2} \\ 0 & \cdots & \cdots & -\frac{t_0}{\Delta^2} & \frac{2t_0}{\Delta^2} + U_N \end{bmatrix} \begin{bmatrix} f_1 \\ f_2 \\ \vdots \\ f_{N-1} \\ f_N \end{bmatrix} = E \begin{bmatrix} f_1 \\ f_2 \\ \vdots \\ f_{N-1} \\ f_N \end{bmatrix} \tag{3.6}$$

Solving the above equation we get N eigen values E_a and their corresponding eigen vectors $f^{(a)}$ which can be expressed as an orthonormal set. We have implemented this using Eigensystem command in MATHEMATICA package which automatically takes care of the orthonormality condition

$$\sum_{i=1}^{N} f_i^{(a)*} f_i^{(b)} = \delta^{ab}. \tag{3.7}$$

The continuous function $f(r)$ is restored from the respective discrete function $f(r_i)$ through proper interpolation. To recover the required radial function we apply $R(r) = f(r)/\sqrt{r}$. For the validation of the present computational method,

we considered the case of $B = 0$T for which the analytical solution is

$$R_{nl}(r) = \alpha \left\{ \frac{(n-1-|l|)!}{(|l|+n-1)!\,(2n-1)} \right\}^{1/2} e^{-\alpha r/2} (\alpha r)^{|l|} L^{2|l|}_{n-|l|-1}(\alpha r) \tag{3.8}$$

where $\alpha = \frac{t_3/t_0}{n-1/2}$ and L^p_q are the associated Laguerre polynomials. For $n = 1, l = 0$ case, the plot of analytical wavefunction is contrasted with corresponding numerical result in Fig. 3.1. The comparison shows heavy mismatch near to the origin and therefore the results should not be trusted. The ground state energy obtained with a 1000 point grid (-12.92 meV) was also in marked disagreement with the exact value (-21.34 meV). At this point the author also wishes to point out that we could get sufficiently accurate results for the solution of 3-dimensional H-impurity using the same method.

The matrix method with higher order accuracy in the approximation of second derivative term was also considered in our research. But this also resulted in similar output with no significant improvement over the present method. Thus we resort to look for a method which can incorporate a non-uniform grid with more samples in the region $r = 0$. The answer for such a technique was found in Numerov's shooting method which incorporates a logarithmic grid.

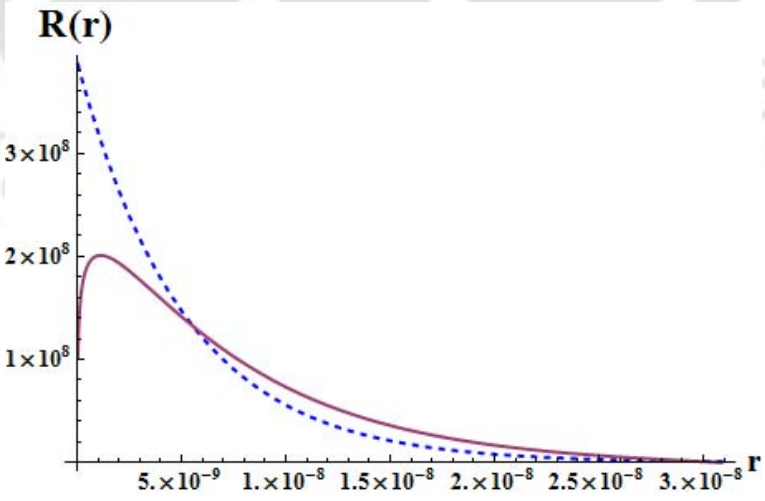

Figure 3.1: Comparison of analytical (dashed) and numerical (continuous) solution based on matrix method

3.2.2 Numerov's Shooting Method

The differential operator eigen value problem in Eq. 3.4 can be expressed in a standard form as

$$f''(r) + Q(r)f(r) = 0 \tag{3.9}$$

where $Q(r) = \frac{E-U(r)}{t_0}$. Using Taylor series expansion we can write

$$f(r \pm \Delta) = f(r) \pm \Delta f'(r) + \frac{\Delta^2}{2} f''(r) \pm \frac{\Delta^3}{6} f'''(r) + \frac{\Delta^4}{24} f''''(r) + \cdots \tag{3.10}$$

From this, we can write the second order derivative of $f(r)$ as

$$f''(r) = \frac{f(r+\Delta) - 2f(r) + f(r-\Delta)}{\Delta^2} - \frac{\Delta^2}{12} f''''(r) + O(\Delta^4). \tag{3.11}$$

Now, the value of $f''''(r)$ can be evaluated by differentiating Eq. 3.9 two times and applying the central difference formula to $Q(r)f(r)$. Thus

$$\begin{aligned} f''''(r) = -\frac{d^2}{dr^2}\{Q(r)f(r)\} = -\frac{1}{\Delta^2}\{&Q(r+\Delta)f(r+\Delta) - 2Q(r)f(r) \\ &+ Q(r-\Delta)f(r-\Delta) + O(\Delta^2). \end{aligned} \tag{3.12}$$

Finally, substituting Eq. 3.12 in Eq. 3.11 and then Eq. 3.11 in Eq. 3.9, we get

$$f(r \pm \Delta) = \frac{f(r)\left[2 - \frac{10\Delta^2}{12}Q(r)\right] - f(r \mp \Delta)\left[1 + \frac{\Delta^2}{12}Q(r \mp \Delta)\right]}{1 + \frac{\Delta^2}{12}Q(r \pm \Delta)} + O(\Delta^6) \tag{3.13}$$

The above equation has higher order accuracy and what it tells is that if we have the value of $f(r)$ at two successive grid points either at the left or at the right boundary, we can generate the entire solution. But we must remember that Eq. 3.9 is an eigen value equation and therefore $Q(r)$ contains an unknown parameter E which is the unknown energy of the electron in the problem. As in the case of all Sturm-Liouville problems, the solutions exits only for specific values of the unknown energy eigen values. The steps involved in numerically solving this problem is as listed below.

1. Assign the value of unknown function $f(r)$ at two successive grid points at

both boundaries, i.e. at $i = 1, 2$ and $i = N, N-1$. Since we know only the value of function f_i at $i = 1$ and $i = N$, i.e. $f_1 = f_N = 0$, we use them and assign $f_2 = f_{N-1} = 1$ (or any fixed number).

2. The initial energy eigen value is also assigned by making a good guess by considering the characteristic energy range of the problem. For all bounded problems, the value of energy is usually taken as negative and therefore the ground state energy will be the most negative. For higher excited states of a given l value, the energies will be lesser and lesser negative. It must also be noticed that the larger the number of nodes in a wavefunction, greater will be its corresponding eigen energy.
3. Using the assigned energy and boundary values, we evaluate Eq. 3.13 for obtaining $f_L(r)$, the forward marching solution and $f_R(r)$, the backward marching solution from the left and right boundary values respectively upto an intermediate point r_c, where both solutions are compared and matched. The intermediate point should be sufficiently away from the origin so that if there are nodes present in the actual function, they will all appear before this point.
4. The number of nodes in the $f_L(r)$ function is counted by tracing the number of times the function changes its sign until it reach the intermediate point r_c we have fixed. If it is more than what we wanted in our solution, we reassign the energy to a lower (more negative) value and vice versa.
5. If the number nodes is as we wanted, then we match the relative slopes of $f_L(r)$ and $f_R(r)$ at the intermediate point r_c by comparing $\frac{f(r_{i+1})-f(r_i)}{f(r_i)}$ from both sides. If $f_L(r)$ has more relative slope than $f_R(r)$, then the energy value must be increased thus spreading the wavefunction more outward from the center. The opposite case is handled in a likewise manner.
6. The algorithm is repeated from step 3 to step 5 until the difference in energy value between two successive loops becomes less than the accuracy we wanted to attain. Once this convergence is achieved, the final solution $f(r)$ can be

constructed in the following way,

$$f(r) = \begin{cases} f_L(r); & r \leq r_c \\ \frac{f_L(r_c)}{f_R(r_c)} f_R(r); & r > r_c \end{cases} \tag{3.14}$$

i.e. by selecting $f_L(r)$ and $f_R(r)$ with suitable normalization at the boundary.

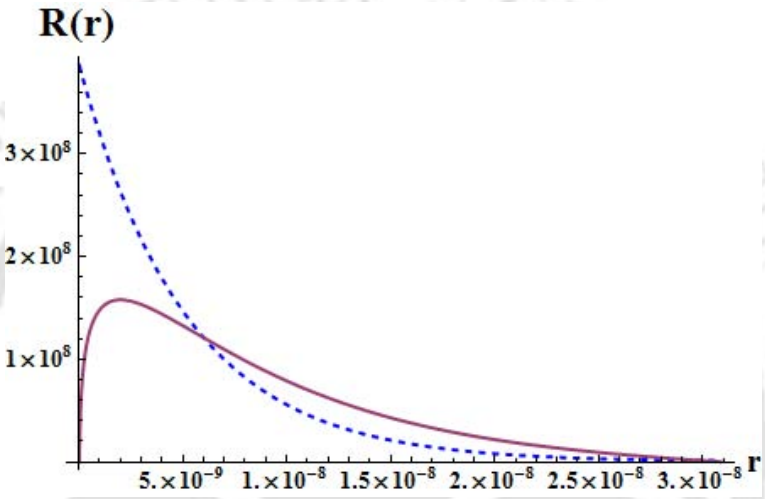

Figure 3.2: Comparison of analytical (dashed) and numerical (continuous) solution based on shooting method

In Fig. 3.2, we plot the ground state solution obtained using Numerov shooting method. For comparison we have also ploted the analytical wavefunction along with it. It can be noticed that the present solution matches more poorly with the exact solution as compared to that in the matrix method of the previous subsection. In addition, the energy of the ground state obtained on a 1000 point grid was -10.26 meV compared to the exact -21.34 meV, which is again very discouraging. But the advantage of shooting method is that we could also extend this technique for non-uniform grid such as the logarithmic grid employed in the following subsection.

3.2.3 Logarithmic Grid

A potential reason for the failure of the previous numerical methods is the existence of a regular singular point of order 2 at $r = 0$. Therefore, in order to nu-

merically capture the true behavior of the wavefunction, we employ a co-ordinate transformation which results in a new differential equation free from such singularities. Such transformation is to set a dimensionless parameter x corresponding to distance as

$$x = \log_e\left(\frac{r}{r_B}\right) \tag{3.15}$$

where $r_B = 2t_0/t_3$, the measure of a characteristic length scale of the system. The above transformation modifies the function $f(r) = f(r_B e^x) = g(x)$ and the corresponding differential equation becomes

$$g''(x) - g'(x) + r^2 Q(r_B e^x) g(x) = 0. \tag{3.16}$$

The first derivative in the above equation is undesirable to be applied with Numerov method. So we substitute $g(x) = e^{x/2}h(x)$ and obtain

$$h''(x) + P(x)h(x) = 0 \tag{3.17}$$

where $P(x) = r^2 Q(r) - 1/4$ and $r = r_B e^x$. Equation (3.17) is in a stardard form to which Numerov shooting method could be directly applied with new boundary conditions written in terms of the variable x. Since x varies from $-\infty$ to $+\infty$, we set lower (x_{min}) and upper (x_{max}) limits such that the function $h(x)$ does not significantly vary beyond these co-ordinate values. For example, for ground state evaluation we took $e^{x_{min}} = 10^{-100}$ and $e^{x_{max}} = 4$. This results in atleast 99% of the total grid points falling in the region $r < r_B$. Fig. 3.3 shows the ground state solution of Eq. (3.17) we obtain using a linear grid of 1000 points along the x-coordinate for the case $B = 0$.

The corresponding wavefunction in r coordinate is shown in Fig. 3.4 in which the exact solution is also plotted. The two results are in excellent agreement as on the same graph they superpose exactly and cannot be distinguished. The energy obtained using the logarithmic grid is -21.34 meV, in excellent agreement with the exact value accurate to two decimal places. Thus we have validated the present numerical method using a case where analytical solutions are available. In the next section we present the results for the general case where $B \neq 0$.

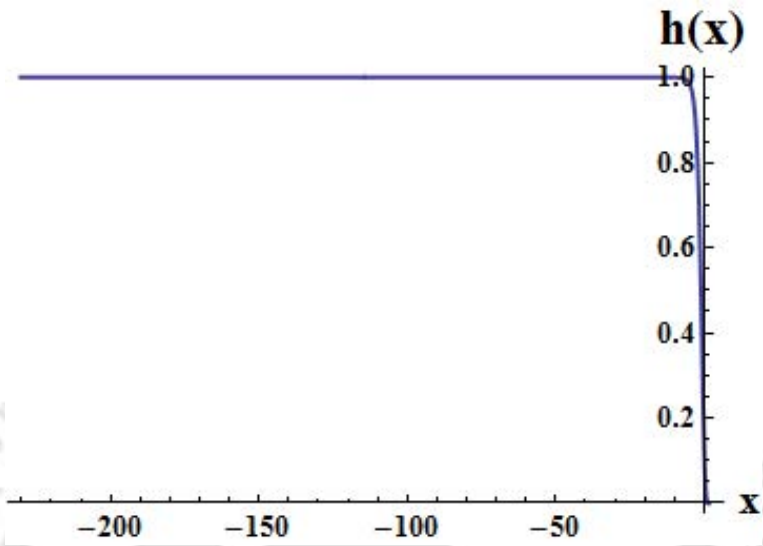

Figure 3.3: Ground state solution for Eq. 3.17. The plot is in arbitrary units.

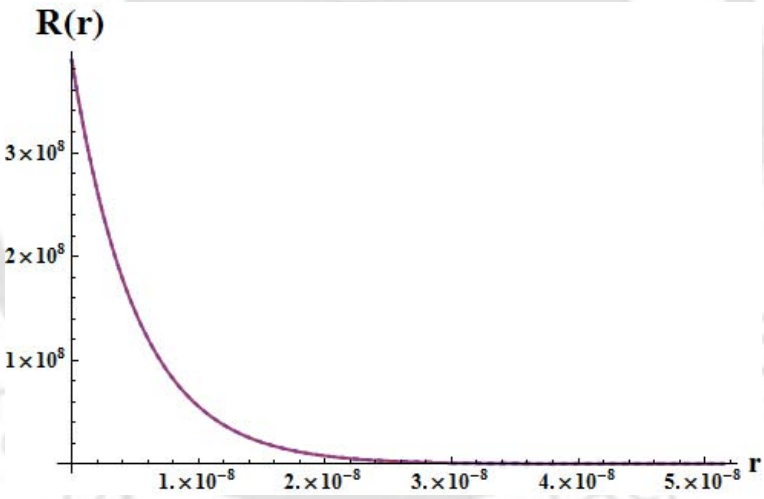

Figure 3.4: Comparison of analytical (dashed curve) and numerical (continuous curve) solution based on shooting method using logarithmic grid

3.3 Results and Discussion

After the validation of Numerov shooting method on a logarithmic grid, we have solved the eigen value problem of a single electron bound to a hydrogenic impurity inside a thin sheet of GaAs material in the presence of a magnetic field. The procedure has to be repeated for each set of quantum numbers (n, l). For a given

value of radial quantum number n, the azimuthal quantum number l can only take values in the range $0, \pm 1, \pm 2, \cdots, \pm(n-1)$. The ground state corresponds to $n = 1$ and $l = 0$. Figure 3.5 shows the radial plot of the ground state wavefunction for different external magnetic flux densities. From this figure it may be seen that the characteristic spread of ground state, the effective Bohr radius (r_B), is around 10nm. The increase from $r_B = 0.53$ Å in the case of H-atom to this high value is due to the effective mass of the electron and dielectric constant of GaAs material. Smaller m_e^* and larger ϵ_r result in larger spread of the electron wavefunction.

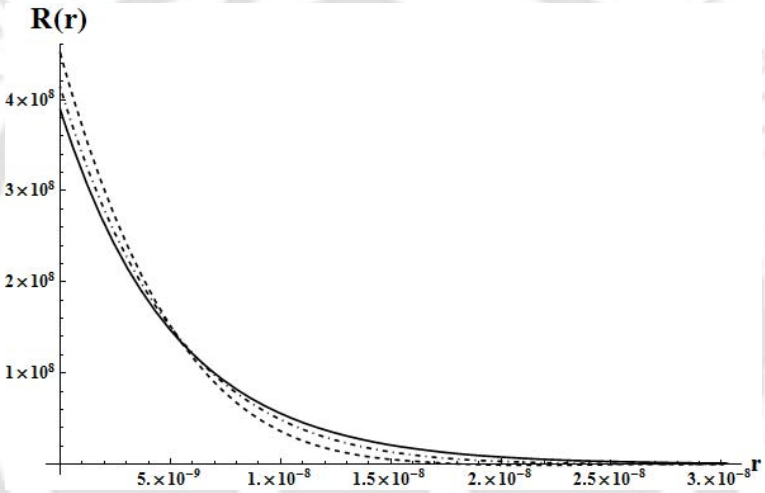

Figure 3.5: Variation of ground state wavefunction with respect to magnetic field strengths $B = 0T$ (continuous), $B = 15T$ (dot-dashed) and $B = 30T$ (dashed).

In the presence of an external magnetic field, the diamagnetic effect will try to confine the electron to magnetic lengths (classical cyclotron radius) of the order of $\sqrt{\frac{\hbar}{qB}}$. Therefore, for appreciable compression of ground state, the magnetic field must be greater than $B = \frac{\hbar}{qr_B^2} = 6.56$T. Signature of diamagnetic compressions can also seen from the field dependent energy spectrum curves plotted in Fig. 3.6. It may be noticed that a significant change in the ground state energy occurs only when the magnetic flux densities are above $6 - 7$ Tesla. For any value of n, the states corresponding to different values of l are degenerate for $B = 0$. This degeneracy is quickly lifted with the introduction of non-zero magnetic field. All the excited bound states which lied very close to one another at zero magnetic field are seen to spread apart with the increase of the magnetic field strength.

This is because the rate of increase in the energy of the a state depends upon the value of l. States with positive values of l, increase its energy at a faster rate with respect to the magnitude of external field in comparison to those having negative values of l.

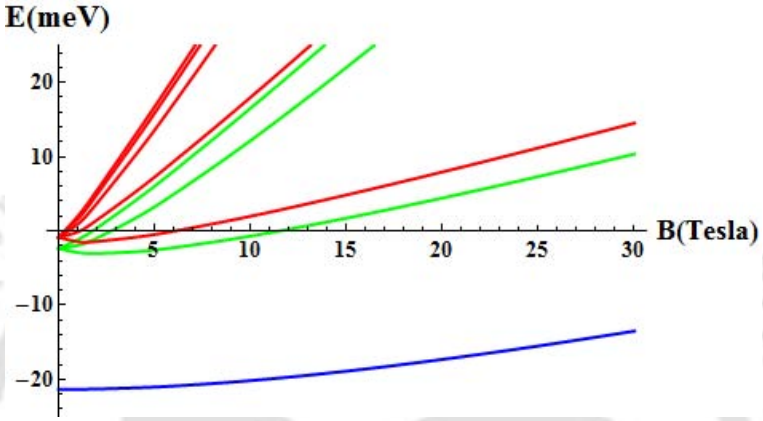

Figure 3.6: Bound state energy level variation with respect to magnetic field strength. The color codes are: blue stands for $n = 1, m = 0$, green stands for $n = 2, m = (-1, 0, 1)$ and, red stands for $n = 3, m = (0, \pm 1, \pm 2)$

The variation of the excited state wavefunctions with respect to the magnetic field is shown in Fig. 3.7. The curves correspond to the quantum number sets $(n = 2, m = 0)$ and $(n = 2, m = -1)$ respectively. The dashed curves correspond to $B = 0$ and the continuous curves correspond to $B = 5$T. Very significant compression of these wavefunctions may be noticed from the radial plots. This is because the average radius of these states at zero magnetic field is larger than the cyclotron radius of the electron at $B = 5$T.

3.4 Conclusion

In this chapter we considered a system of a single electron bound to a hydrogenic donor impurity inside a thin sheet of GaAs semiconductor material in the presence of an orthogonal magnetic field. We approximated the system as a two-dimensional problem with $1/r$ potential. The solutions where sought numerically. First we tried a solution using central difference approximation formula. When we try to validate the results using a case $(B = 0)$ for which analytical solutions

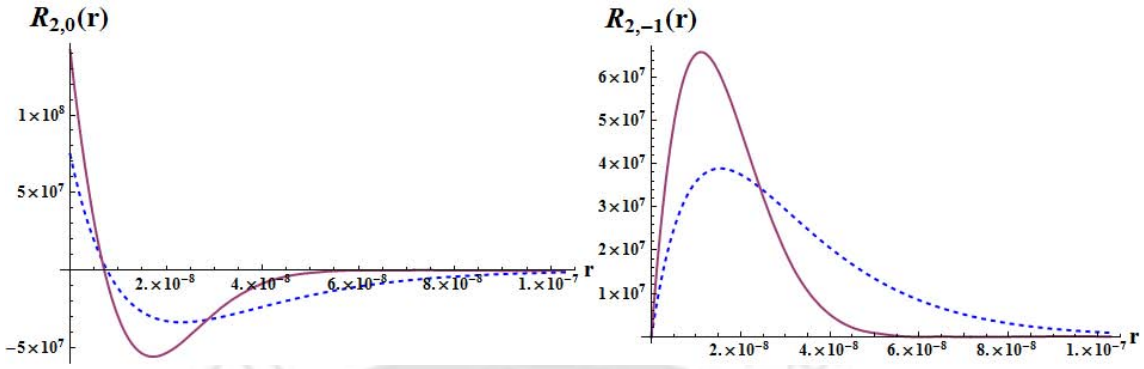

Figure 3.7: Compression of excited states with respect to magnetic field.

exist, we noticed significant deviation near the location of impurity. This may be attributed to the presence of singularity in potential at that point. Therefore, we try to improve the results using a higher order accurate method called matrix Numerov method. Again, the results turned out to be incorrect near the location of singularity. Finally we used a logarithmic grid based Numerov shooting method to sample the solutions more frequently near the singularity point. Using this method, we achieved very accurate solutions of wavefunctions and energy values for the case of zero magnetic field. We then introduced the terms corresponding to arbitrary magnetic field and obtained solutions for the eigen value problem at various values of azimuthal quantum number l. The variation of eigen energies are plotted as function of external magnetic field. We noticed that the ground state energy lies way below all excited states. The energy of the ground state was seen to undergo no significant change until $B = 5\text{T}$. In contrast, for the excited states, their energy varies even with moderate magnetic flux densities. This behavior may be explained by looking at the spread of various energy eigen states. The spread of ground state is very small compared to that of all the excited states. For an applied magnetic field to diamagnetically compress any wavefunction, its characteristic radial spread must be comparable to cyclotron radius. For the excited states, this condition will be satisfied with smaller magnetic field as their radial spread is larger in comparison to the ground state spread. Since the spread of the wavefunction of a donor electron in any host material is decided by the effective mass and dielectric constant of the material, these characteristics will vary with the type of host material.

Chapter 4

Two electrons in a cylindrical quantum dot

4.1 Introduction

Quantum dots in magnetic fields are extensively studied in the context of nanotechnology, both theoretically as well as experimentally [26; 27]. Technology is now matured enough to have precise control over the number of electrons inside the QDs [91]. To theoretically study few electron dots, various model potentials are employed such as rectangular, harmonic oscillator, cylindrical, inverted-Gaussian, spherical etc. [92; 93; 94; 95; 96]. Though for majority of cases harmonic oscillator model potential is a good approximation, for certain optically active self-assembled quantum dots, cylindrical potential is a better approximation [97]. In the present chapter, we focus on a two electron cylindrical quantum dot with a finite-height discontinuous confinement potential in the presence of a magnetic field in its axial direction. The one-electron problem for such a GaAs/$Ga_{1-x}Al_xAs$ dot was studied earlier [98].

Two electron quantum dots are interesting because it is the simplest case for studying the effect of electron-electron interaction [99]. We can anticipate that the energy spectrum of a multi-electron quantum dot is going to depend on various factors such as confinement due to external magnetic field, confinement due to dot-potential, and finally the electron-electron interaction and correlation

effects. For a dot with very small height to diameter ratio, we can safely assume that electrons are restricted to the ground state sub-band in the z-direction and thus the problem reduces to the case of a two-dimensional circular disc. The energy levels for a two electron quantum dot with harmonic potential was studied extensively by many researchers [100; 101; 102; 103; 104; 105]. A similar study for discontinuous model potential was done by F. M. Peeters et al. wherein they solved the one electron problem using the finite difference scheme, and then used those results to do variational analysis for the two electron problem [106]. In the present work, we employ linear variational analysis where the trial wave function is constructed out of single electron harmonic oscillator wavefunctions.

This chapter is organized as follows. Section 4.2 discusses the theoretical model and the basic analytical steps involved, the results are the presented and discussed in Section 4.3, and finally the chapter is concluded in Section 4.4.

4.2 Theory and Procedure

In the following analysis we consider a quantum dot based on GaAs/$Ga_{1-x}Al_xAs$ heterostructure, but assume that the electron effective mass remains constant across the heterogeneous boundary. This is a reasonable approximation for a potential step of size 100 meV, as it amounts to only a 15% difference in the effective mass for the $Ga_{1-x}Al_xAs$ outer region in comparison to that of the inner GaAs region [98]. As the the electron densities for the lower energy states are negligible in the outer region, this difference does not contribute much to our problem. Further, we assume a much stronger confinement in the axial direction of the dot relative to that in its radial direction, thus justifying our two dimensional model for the analysis [106]. Under these assumptions, the Hamiltonian of a two electron cylindrical quantum dot system in a constant magnetic field B can be written as

$$H = \sum_{i=1,2} \left[\frac{1}{2m_e^*} \left(\vec{p_i} + q\vec{A_i} \right)^2 + V\left(r_i\right) + \frac{g\mu_B}{\hbar} \vec{S_i} \cdot \vec{B} \right] + \frac{q^2}{\kappa \left| \vec{r_1} - \vec{r_2} \right|} \tag{4.1}$$

where $\vec{A}_i = \frac{B}{2}(0, r_i, 0)$ and

$$V(r_i) = \begin{array}{lll} 0 & ; & r_i \leq r_0 \\ V_0 & ; & r_i > r_0 \end{array} .$$

Here $\vec{r}_i$ and $\vec{p}_i$ are the conjugate position and momentum of the i^{th} electron, m_e^* is the electron effective mass, q is the electron charge, g is the electron g-factor, μ_B is the Bohr magneton, $\vec{S}_i$ is the spin angular momentum of the i^{th} electron, and $\kappa = 4\pi\epsilon$, in SI units. Here, the value of quantum dot permittivity, ϵ, is given an average value of $13.1\epsilon_0$ throughout the material. In the operator form Eq.(4.1) becomes

$$\hat{H} = \sum_{i=1}^{2}\left[-\frac{\hbar^2}{2m_e^*}\left(\frac{\partial^2}{\partial r_i^2} + \frac{1}{r_i}\frac{\partial}{\partial r_i} + \frac{1}{{r_i}^2}\frac{\partial^2}{\partial \phi_i^2}\right) + \frac{\omega_C}{2}\hat{L}_{z_i} + \frac{1}{2}m_e^*\left(\frac{\omega_C}{2}\right)^2 {r_i}^2 + V(r_i) + \frac{\hbar\omega_L}{2}\hat{\sigma_z}^{(i)}\right] + \frac{q^2}{\kappa\left|\vec{r_1} - \vec{r_2}\right|} \tag{4.2}$$

where $\hat{L}_{z_i} = -i\hbar\frac{\partial}{\partial\phi_i}$, the z-component of the angular momentum operator of the i^{th} electron, $\omega_C = \frac{qB}{m_e^*}$, the cyclotron frequency, and $\omega_L = \frac{qB}{m_0}$, the Larmor frequency.

By adding and subtracting a harmonic oscillator potential $\frac{1}{2}m_e^*\omega_0^2 r_i^2$ for each electron, we can re-write the above Hamiltonian as

$$\hat{H} = \hat{H}^0(1,2) + \hat{H}'(1,2) \tag{4.3}$$

The definitions of $\hat{H}^0(1,2)$ and $\hat{H}'(1,2)$ are as given below.

$$\hat{H}^0(1,2) = \hat{H}_{ho}(1) + \hat{H}_{ho}(2) \tag{4.4}$$

where

$$\hat{H}_{ho}(i) = -\frac{\hbar^2}{2m_e^*}\left(\frac{\partial^2}{\partial r_i^2} + \frac{1}{r_i}\frac{\partial}{\partial r_i} + \frac{1}{{r_i}^2}\frac{\partial^2}{\partial\phi_i^2}\right) + \frac{\omega_C}{2}\hat{L}_{z_i} + \frac{1}{2}m_e^*\omega^2 {r_i}^2 \tag{4.5}$$

with $\omega = \sqrt{\omega_0^2 + \left(\frac{\omega_C}{2}\right)^2}$. Similarly,

$$\hat{H}'(1,2) = \hat{W}(1,2) + \hat{Z}(1,2) + \hat{C}(1,2) \tag{4.6}$$

where

$$\hat{W}(1,2) = \sum_{i=1}^{2}\left[V(r_i) - \frac{1}{2}m_e^*\omega_0^2 r_i^2\right], \quad \text{the residue potential term}$$

$$\hat{Z}(1,2) = \frac{\hbar\omega_L}{2}\sum_{i=1}^{2}\hat{\sigma}_z^{(i)}, \quad \text{the Zeeman term and}$$

$$\hat{C}(1,2) = \frac{q^2}{\kappa|\vec{r}_1 - \vec{r}_2|}, \quad \text{the Coulomb term.}$$

The eigenvalues and eigenfunctions of $\hat{H}_{ho}$ are well known [26] and are as given below.

$$\hat{H}_{ho}\ \varphi_{n,m}(r,\phi) = \mathcal{E}_{n,m}\ \varphi_{n,m}(r,\phi) \tag{4.7}$$

where $n = 0, 1, 2\ldots$ and $m = 0, \pm1, \pm2\ldots$ are the radial and azimuthal quantum numbers respectively, and

$$\mathcal{E}_{n,m} = \hbar\omega\,(2n + |m| + 1) + \hbar\omega_C\frac{m}{2} \tag{4.8}$$

$$\varphi_{n,m}(r,\phi) = \frac{1}{a_B^{1+|m|}\,|m|\,!}\sqrt{\frac{(|m|+n)\,!}{\pi n!}}\exp\left[\frac{-r^2}{2a_B^2} + im\phi\right] r^{|m|}{}_1F_1[-n, |m|+1, \frac{r^2}{a_B^2}] \tag{4.9}$$

where $a_B = \sqrt{\frac{\hbar}{m_e^*\omega}}$ is the effective Bohr radius of the quantum dot.

Now, in a linear variational theory [107], we consider a trial wavefunction expressed as

$$|\psi\rangle = c_1|\chi_1\rangle + c_2|\chi_2\rangle + \cdots + c_i|\chi_i\rangle + \cdots + c_d|\chi_d\rangle \tag{4.10}$$

Here d is the dimension of the basis set, coefficients $c_1, c_2, \ldots, c_d$ are variational parameters and $|\chi_i\rangle$ are the orthonormalized two-electron states. If s_1 and s_2 are the spin quantum numbers of individual electrons (each having a value $\frac{1}{2}$), and if s is the total spin quantum number of the two-electron system, then by angular momentum addition rule s can take only two values viz. $s = 0$ corresponding to

$|s_1 - s_2|$, and $s = 1$ corresponding to $|s_1 + s_2|$. For $s = 0$ state, the z-component of the total spin operator, $\hat{S}_z$, can have only one value for its quantum number viz. $m_s = 0$ (singlet), and for the $s = 1$ state, it can take three values viz. $m_s = 0, \pm 1$ (triplet). The orbital part of the singlet state must be symmetric and that of the triplet states must be antisymmetric. These can be easily constructed out of one-electron wavefunctions by taking Slater permanent and determinant respectively. For example, if $|\varphi_{n_1,m_1}\rangle$ and $|\varphi_{n_2,m_2}\rangle$ are any two distinct one-electron eigen states, then

$$\left|\chi^{\pm}_{n_1,m_1,n_2,m_2}(1,2)\right\rangle = \frac{|\varphi_{n_1,m_1}(1)\rangle\,|\varphi_{n_2,m_2}(2)\rangle \pm |\varphi_{n_2,m_2}(1)\rangle\,|\varphi_{n_1,m_1}(2)\rangle}{\sqrt{2}} \tag{4.11}$$

is a valid orthonormalized symmetric (antisymmetric) two-electron orbital wavefunction constructed out of them, except for the case $(n_1, m_1) = (n_2, m_2)$ where, an additional factor of $\sqrt{2}$ must be taken care of. This, multiplied by their appropriate spin-wavefunction counterpart ($|s\rangle$), forms the required basis wavefunctions in Eq. (4.10), given by

$$|\chi_i\rangle = \left|\chi^{\pm}_i\right\rangle |s = 0(1)\rangle \tag{4.12}$$

Since $\left[\hat{H}, \hat{L}_z\right] = 0$, the total z-component of the angular momentum, $M = m_1 + m_2$, must be the same for all terms in the trial wavefuntion. Similarly, since $\left[\hat{H}, \hat{S}^2\right] = \left[\hat{H}, \hat{S}_z\right] = 0$, every term in the trial wavefunction must have the same value for the s and m_s quantum numbers. Thus, we can do variational analysis for each combinations of M, s and m_s values separately. For each case, the linear variational analysis reduces to solving an eigen value problem of the type

$$[H]\,\{C\} = E\,\{C\}\,. \tag{4.13}$$

Here $[H]$ is a square matrix of size $d \times d$ with elements $H_{ij} = \left\langle \chi_i \middle| \hat{H} \middle| \chi_j \right\rangle$, $\{C\}$ is a column matrix of size $d \times 1$ with unknown coefficients c_i of Eq. (4.10) as elements, and E is their corresponding eigen energy. The matrix $[H]$ can be written as a sum of matrices $[H^0]$ and $[H']$ corresponding to the operators $\hat{H}^0$ and $\hat{H}'$ defined via Eq. (4.3). The elements of $[H^0]$ for the case of singlet (+)

and triplet $(-)$ states are given by Eq. (4.14). Due to the orthogonality of one-electron wavefunctions $|\varphi_{n,m}\rangle$, it may be noticed that $[H^0]$ has non-zero elements only along its diagonal.

$$\begin{aligned} H^0_{ij} &= \left\langle \chi^{\pm}_{n_1,m_1,n_2,m_2} \left| \hat{H}_{ho}(1) + \hat{H}_{ho}(2) \right| \chi^{\pm}_{n_3,m_3,n_4,m_4} \right\rangle \\ &= \delta_{n_1 n_3}\delta_{m_1 m_3}\delta_{n_2 n_4}\delta_{m_2 m_4}\left(\mathcal{E}_{n_3,m_3} + \mathcal{E}_{n_4,m_4}\right) \end{aligned} \tag{4.14}$$

Similarly, the elements of $[H']$ are also evaluated. In the case of triplet states, the result after substituting for $|\chi^-\rangle$ from Eq. (4.11) becomes

$$\begin{aligned} H'_{ij} = &\left\langle \varphi_{n_1,m_1}(1)\,\varphi_{n_2,m_2}(2) \left| \hat{H}'(1,2) \right| \varphi_{n_3,m_3}(1)\,\varphi_{n_4,m_4}(2) \right\rangle \\ &- \left\langle \varphi_{n_1,m_1}(1)\,\varphi_{n_2,m_2}(2) \left| \hat{H}'(1,2) \right| \varphi_{n_4,m_4}(1)\,\varphi_{n_3,m_3}(2) \right\rangle \end{aligned} \tag{4.15}$$

A little care must be given while evaluating the elements of $[H']$ for singlet states. This is because, we can build symmetric orbital states out one-electron eigenstates even when $n_1 = n_2$ and $m_1 = m_2$, and those states are different from the general symmetric states given by Eq. (4.11). For the general states,

$$\begin{aligned} H'_{ij} = &\left\langle \varphi_{n_1,m_1}(1)\,\varphi_{n_2,m_2}(2) \left| \hat{H}'(1,2) \right| \varphi_{n_3,m_3}(1)\,\varphi_{n_4,m_4}(2) \right\rangle \\ &+ \left\langle \varphi_{n_1,m_1}(1)\,\varphi_{n_2,m_2}(2) \left| \hat{H}'(1,2) \right| \varphi_{n_4,m_4}(1)\,\varphi_{n_3,m_3}(2) \right\rangle \end{aligned} \tag{4.16}$$

When $n_1 = n_2$ and $m_1 = m_2$ and $n_3 = n_4$ and $m_3 = m_4$, the elements of $[H']$ for singlet states becomes

$$H'_{ij} = \left\langle \varphi_{n_1,m_1}(1)\,\varphi_{n_1,m_1}(2) \left| \hat{H}'(1,2) \right| \varphi_{n_3,m_3}(1)\,\varphi_{n_3,m_3}(2) \right\rangle \tag{4.17}$$

The final case is when quantum numbers are equal only on one side, say $n_1 = n_2$ and $m_1 = m_2$, the elements of $[H']$ for singlet states are given by

$$H'_{ij} = \sqrt{2}\left\langle \varphi_{n_1,m_1}(1)\,\varphi_{n_1,m_1}(2) \left| \hat{H}'(1,2) \right| \varphi_{n_3,m_3}(1)\,\varphi_{n_4,m_4}(2) \right\rangle \tag{4.18}$$

All the elements of $[H']$ were found out through numerical integration in the MATHEMATICA software. To simplify the case, we can split and write $[H']$ as a sum of three matrices corresponding to the terms defined in Eq. (4.6) as

$$[H'] = [W] + [Z] + [C] \tag{4.19}$$

Now, the matrix $[Z]$ is diagonal due to the orthonormality of orbital part of the basis wavefunctions. Furthermore, these diagonal elements are also zero for $m_s = 0$ states $\left(\frac{|\uparrow\downarrow\rangle \pm |\downarrow\uparrow\rangle}{\sqrt{2}}\right)$. But for $m_s = \pm 1$ states $(|\uparrow\uparrow\rangle, |\downarrow\downarrow\rangle)$, it give rises to a constant value, $\pm\hbar\omega_L$ for all the diagonal elements. Similarly, many of the elements in $[W]$ are zeros due to the othogonality condition when $m_1 \neq m_3$ or $m_2 \neq m_4$. Again, because of the azimuthal and exchange symmetries of the $\hat{W}(1,2)$ term, all the non-zero $[W]$ elements require only one–variable numerical integrations. The evaluation of elements in the $[C]$ matrix involves calculation of terms like

$$C_{12,34} = \left\langle \varphi_{n_1,m_1}(1)\, \varphi_{n_2,m_2}(2) \left| \hat{C}(1,2) \right| \varphi_{n_3,m_3}(1)\, \varphi_{n_4,m_4}(2) \right\rangle. \tag{4.20}$$

If we substitute $\varphi_{n,m}(r,\phi) = \rho_{n,m}(r)\, \frac{e^{im\phi}}{\sqrt{2\pi}}$ in Eq. (4.20) we get,

$$\begin{aligned} C_{12,34} = \frac{q^2}{2\pi\kappa} \int_{r_1=0}^{\infty} r_1\, dr_1\, \rho^*_{n_1,m_1}(r_1)\, \rho_{n_3,m_3}(r_1) \\ \int_{r_2=0}^{\infty} r_2\, dr_2\, \rho^*_{n_2,m_2}(r_2)\, \rho_{n_4,m_4}(r_2)\, I(r_1,r_2) \end{aligned} \tag{4.21}$$

where

$$I(r_1,r_2) = \int_{\phi=0}^{2\pi} d\phi_1 \int_{\phi=0}^{2\pi} d\phi_2\, \frac{\exp[i(-m_1+m_3)\phi_1 + i(-m_2+m_4)\phi_2]}{|\vec{r}_1 - \vec{r}_2|}.$$

Using the multipole expansion of $\frac{1}{|\vec{r}_1-\vec{r}_2|}$ and simplifying further, $I(r_1,r_2)$ becomes

$$I(r_1,r_2) = 4\pi^2 \frac{1}{r_>} \sum_{l=0}^{\infty} \left(\frac{r_<}{r_>}\right)^l \frac{(l-m_1+m_3)!}{(l+m_1-m_3)!} (P_l^{m_1-m_3}(0))^2 \tag{4.22}$$

where, $r_> = r_1$ and $r_< = r_2$ when $r_1 > r_2$ and vice versa, and P_l^m is the associated Legendre function. Substituting this expression for $I(r_1,r_2)$ in Eq. (4.21), we get

$$C_{12,34} = \frac{2\pi q^2}{\kappa} \sum_{l=|m_1-m_3|}^{\infty} \frac{(l-m_1+m_3)!}{(l+m_1-m_3)!} (P_l^{m_1-m_3}(0))^2 \int_{r_1=0}^{\infty} r_1\, dr_1\, \rho^*_{n_1,m_1}(r_1)\, \rho_{n_3,m_3}(r_1) \left[\int_{r_2=0}^{r_1} dr_2\, \rho^*_{n_2,m_2}(r_2)\, \rho_{n_4,m_4}(r_2) \left(\frac{r_2}{r_1}\right)^{l+1} + \int_{r_2=r_1}^{\infty} dr_2\, \rho^*_{n_2,m_2}(r_2)\, \rho_{n_4,m_4}(r_2) \left(\frac{r_1}{r_2}\right)^{l} \right] \tag{4.23}$$

Thus we have replaced the original four-variable integration given in Eq. (4.20) with an infinite sum of two-variable integrations. But since the result is pretty accurate with only first few (say 30) terms of Eq. (4.23), this new formula helps us to achieve fast computation of the elements in $[C]$.

Once all the elements of $[H]$ are evaluated, we proceed to solve the eigen value problem of Eq. (4.13) which will then give us the energy spectrum and corresponding electron wavefunctions. We have done this by using the subroutine Eigensystem available in the MATHEMATICA software. This process is done separately for each value of quantum numbers (M, s) and it is then repeated for values of B ranging from 0 to 30 Tesla. The electron density, $\eta(r)$, and pair correlation function, $f_{pc}(\vec{r})$, are then evaluated using these resultant wavefunctions, following the definitions mentioned in reference [106] as given below

$$\begin{aligned} \eta(\vec{r}) &= \sum_{i=1}^{2} \langle \delta(\vec{r} - \vec{r_i}) \rangle \\ f_{pc}(\vec{r}) &= \langle \delta(\vec{r} - \vec{r_1} + \vec{r_2}) \rangle \end{aligned} \tag{4.24}$$

4.3 Results and Discussion

The results obtained here are classified in terms of quantum numbers (M, s), which form separate infinite-dimensional subspaces within the Hilbert space of the problem. The accuracy of results, obtained through linear variational analysis for each such case, depends on how well the basis set spans over the subspace of interest. Though the lower energy states are mostly spanned by the lower energy basis functions, the accuracy of results gets better as we increase the size

of the basis set. This size, in turn depends on the number of one-electron eigenfunctions we begin with, from which we construct those basis functions. In the present problem, we have used single electron eigenfunctions $|\varphi_{n,m}\rangle$ with quantum numbers n ranging from 0 to ν, and m ranging from $-\mu$ to μ. This results in a total number of $N_1 = (\nu+1)(2\mu+1)$ single electron wavefunctions. From N_1 one-electron wavefunctions, we can construct $\frac{N_1(N_1+1)}{2}$ symmetric wavefunctions for singlet states, and $\frac{N_1(N_1-1)}{2}$ antisymmetric wavefunctions for triplet states. The number of two-electron basis functions that can be constructed for a given ν, μ, M and s values is given by

$$N_2 = \begin{cases} (\nu+1)\left[(\nu+1)\left(\mu+1-\frac{|M|}{2}\right)-\frac{\nu}{2}-s\right] & ; \quad M \text{ even} \\ (\nu+1)^2\left(\mu-\frac{|M|-1}{2}\right) & ; \quad M \text{ odd} \end{cases} \tag{4.25}$$

where $\mu+1-\frac{|M|}{2}$ and $\mu-\frac{|M|-1}{2}$ respectively are, for even and odd cases of M, the number of possible combinations of m_1 and m_2 such that $m_1+m_2=M$. Now, $(\nu+1)^2$ is the number of possible combinations for n_1 and n_2 for each allowed combination of m_1 and m_2 values. The $\frac{\nu(\nu+1)}{2}$ in Eq. (4.25) is the number of repeated cases of two-electron wavefunctions for the $m_1=m_2$ case, due to the permutation of n_1 and n_2 values. Finally the subtraction of $(\nu+1)\,s$ term removes the prohibited case of $(n_1,m_1)=(n_2,m_2)$ from the antisymmetric orbital wavefunctions of triplet states. The results plotted in this section are for the case $\nu=2$ and $\mu=3$, giving $N_1=21$, in which case we obtain 231 singlet basis states and 210 triplet basis states. These states are then classified according to their M values, giving rise to different basis dimensions for each case, as listed in Table 4.1. It may be noticed from the table that the largest basis set is obtained for $M=0$ and the smallest basis set is for $M=\pm 2\mu$. Therefore, for a given analysis described here, we expect more accurate results for terms with smaller $|M|$ values.

An important parameter we must fix beforehand is the value of ω_0 in Eq. (4.5). We expect best results when the harmonic oscillator potential $V_{ho}(\omega_0, r) = \frac{1}{2}m_e^*\omega_0^2 r^2$ effectively mimics the most of the cylindrical step potential of the original problem. To find this value of ω_0, we have expressed $V_{ho}(\omega_0, r_0) = kV_0$,

M **value**	**Dimension of Singlet basis**	**Dimension of Triplet basis**
-6	6	3
-5	9	9
-4	15	12
-3	18	18
-2	24	21
-1	27	27
0	33	30
1	27	27
2	24	21
3	18	18
4	15	12
5	9	9
6	6	3

Table 4.1: Dimensions of two-electron basis set for different M values

where V_0 is the step-size and k is a dimensionless number whose value we need to determine. Then ω_0 becomes

$$\omega_0(k) = \sqrt{\frac{2kV_0}{m_e^* r_0^2}} \tag{4.26}$$

By tuning the value of k, we found that there exists a minimum for the ground state energy when $k = 0.25$. This corresponds to $\hbar\omega_0 = 15.85$ meV for a quantum dot with $r_0 = 15$nm and $V_0 = 100$ meV.

The energy spectrum obtained for various quantum numbers are plotted as a function of external magnetic field strength in Fig. 4.1. We have chosen $r_0 =$ 15nm, to avoid the piling up of many energy levels in a window of energy between 0 to 100 meV, but at the same time granting us decent number of curves for observation. In the figure, we have shown curves for both siglet (continuous) and triplet (dashed) states, and in each case M varying from -2 to $+2$ which are represented by various color codes, as mentioned in the figure caption. Curves

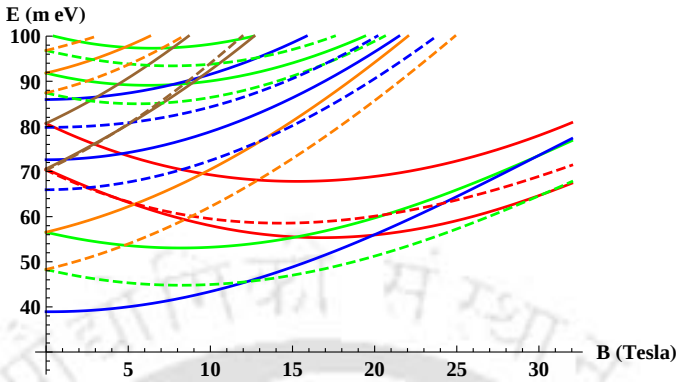

Figure 4.1: Two electron energy spectrum for a cylindrical quantum dot. Here, the dotted (continuous) curves stands for $s = 1$ ($s = 0$) states. The colors red, green, blue, orange and brown stand for $M = -2, -1, 0, 1, 2$ respectively. The results plotted are for an $r_0 = 15$nm and $V_0 = 100$ meV.

with higher energies for the same color code corresponds to excited states, which may be labeled by a new quantum number $N = 1, 2, 3$...etc. We notice from the figure that at 0T, the states corresponding to $\pm M$ are degenerate and the degeneracy is lifted as the magnetic field is switched on. The curves for different values of m_s quantum number have been suppressed for the sake of clarity. If we add them, the only difference it will make is to introduce two more levels for each triplet state, which differ from the present one by $\pm\hbar\omega_L$. The results we obtained show considerable similarity with those in Reference [106], where they have plotted for cylindrical quantum dot with $V_0 = 500$ meV and $r_0 = 10$nm and $r_0 = 20$nm respectively. Similar to their cases, grouping of energy levels are noticed at higher magnetic field strengths as shown in Fig. 4.1. Similarly, singlet-triplet crossing is observed for the ground state, with the increase of external magnetic field. Our results for 15nm dot nicely interpolates with the two cases in reference [106], in terms of the scales of energy and magnetic field strength as can be seen from the graphs. The first singlet-triplet crossing here takes place at around 12T and the second one happens at around 29T, which were 10T and 19T in their case of 20nm quantum dot. The discrepancies could be attributed to the differences in confinement energies of both cases due to the differences in r_0 and V_0 values.

In Fig. 4.2, we have plotted the magnetization of the present two-electron

quantum dot as a function of magnetic field strength. This is evaluated by taking the negative derivative of free energy with respect to magnetic field as [108]

$$\mu_{mag} = -\frac{\partial F}{\partial B} \tag{4.27}$$

where $F = -kT\ln Z(B)$ is the free energy of the system, and $Z(B) = \sum_i e^{-\frac{E_i(B)}{kT}}$ is the system partition function. Here B is the magnetic field strength and E_i are the energy levels plotted in Fig. 4.2(a). The result shown are for a temperature $T = 4$K and magnitude of magnetization are expressed in units of Bohr magneton ($\mu_B = 5.79 \times 10^{-2}$meV/T). It may be noticed that, we now have lesser number of singlet-triplet transitions for the ground state as compared to that in Fig. 4.1 and the first one takes place early at around 10.3T. This is because we now have taken into account the Zeeman effect, whose contribution is important for the calculation of free energy. Similar results for two electrons in parabolic quantum dot potential were shown earlier in reference [109]. In comparison, we notice only one oscillation in the magnetization curve as opposed to many in their case for a given range of magnetic field strength. This can be attributed to the large effective confinement radius (almost double in comparison) in their case. We also notice larger paramagnetic contribution in the step size of magnetization at the point of transition, which definitely points to the contribution from exchange interaction and orbital motion. The step is found to be abrupt for very low values of T but smoothens with the increase of temperature, as the value of kT becomes comparable to that of the spacing between energy levels. Since magnetization can be measured experimentally, these results are useful for the determination of spin states in spintronic applications as reported in reference [39].

We have also plotted the electron radial densities and pair correlation functions for various quantum numbers (M, s) and magnetic field strengths. These are shown in Fig.(4.3), where we again notice very compliant results with that in reference [106]. The qualitative nature and quantitative values of both the radial electron densities and pair correlation functions look very appealing by comparison of these results. At higher magnetic fields, these functions are seen to be pressed toward the center of the dot, due to the magnetic confinement. But for low magnetic fields, the electron-electron interaction pushes them apart,

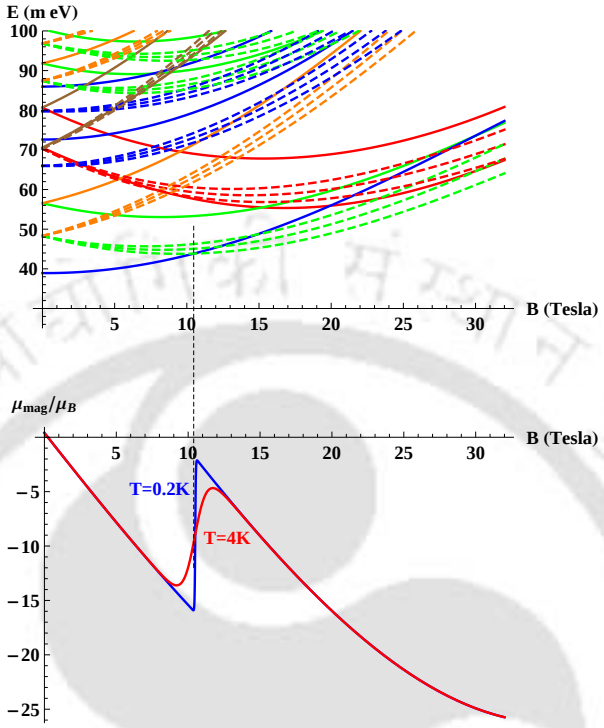

Figure 4.2: (a) Two electron energy spectrum including the multiplicity of triplet states due to Zeeman interaction, (b) Magnetization at $T = 0.2$K (blue) and 4K (red) are shown as a function of magnetic field strength.

while the dot confinement potential limits the extent to which they can be separated. Due to the inherent anti-symmetry in the orbital wavefunction of the triplet states, $f_{pc}(0) = 0$ as two electrons cannot be in the same place in such states. In contrast, for all singlet states, there exists a non-zero value for $f_{pc}(0)$.

4.4 Conclusion

We have conducted a linear variational analysis for a two-electron cylindrical quantum dot with step potential, with a trial wavefunction constructed out of harmonic oscillator eigen functions. We fixed the strength of this oscillator potential by tuning the oscillator frequency for minimum ground state energy. We plotted the two-electron energy spectrum as a function of external magnetic field strength for various values of quantum numbers (M, s). From these, we evaluated

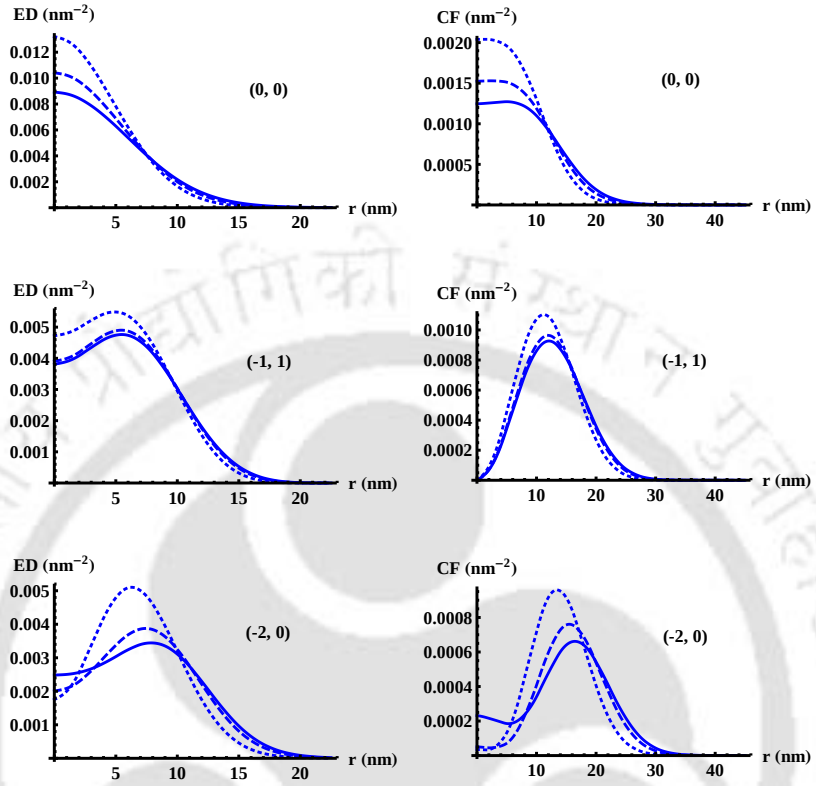

Figure 4.3: Left column: Radial electron density (ED), $\eta(r, \phi = 0)$; Right column: Pair correlation function (CF), $f_{pc}(r, \phi = 0)$. The continuous, dashed and dotted curves corresponds to $B = 0$, 10 and 20 Tesla respectively. The rows 1, 2 and 3 corresponds to quantum numbers $(0, 0)$, $(-1, 1)$ and $(-2, 0)$ respectively. All results are for an $r_0 = 15$nm.

the free energy and determined the dependency of magnetization with respect to the magnetic field strength. Similarly, we have also plotted radial electron density and pair correlation functions for different quantum numbers and different magnetic field strengths. We could convincingly obtain all the qualitative and even most of the quantitative features of the exact results obtained by F. M. Peeters et al. [106] where they considered around 1000 basis states for each combination of (M, s) quantum numbers. In comparison, we considered less than 50 basis states to obtain the results displayed. This shows that a very few low-energy harmonic oscillator eigenfunctions are able to effectively capture the quantum dot cylindrical step-potential. Our method also eliminates the requirement of finite element

analysis for obtaining one electron wavefunctions. However, our results are valid only under the assumption that the effective mass and permittivity of the dot are almost constant throughout the material. This may be taken as a very good approximation as the effective mass and permittivity changes are known to be very small with respect to the composition of the material.

Chapter 5

Two electrons in laterally coupled quantum dots

5.1 Introduction

Coupled quantum dots or artificial molecular hydrogen is an important problem that attracted attention of many researchers during the past two decades. Some have pursued this to characterize its physical properties, whereas others approached it from the application point of view. Coulomb blockade and conductance properties [110; 111], electronic structure and optical properties [112; 113; 114], electron-phonon interactions [115], Kondo resonant spectra [116], etc. are examples for some of the physical properties studied. On the other hand, application of these nanostructures include quantum gates [39], resonant tunneling diode [117], preparation of entangled states [118], vertical cavity lasers [119], quantum cellular automata [120] etc. The coupling of quantum dots are done either laterally [121] or vertically [122]. The confinement potential for a coupled quantum dot could be created out of patterned gate electrodes [43], donor impurity placement [48] or by pure band-gap engineering as in self-assembled coupled quantum dots [123]. The advantage of a patterned electrode based potential is that we can electrically control the inter-dot distance as well as the number of electrons inside each dot.

The modeling of the confinement potential depends upon the method of con-

finement. For donor impurities, Coulomb potential is an ideal one. For self-assembled quantum dots, step potential may be a good approximation. In the case of self-assembled quantum dots, experimental results indicate a violation of the generalized Kohn theorem suggesting discontinuities in the confinement potential [124; 125]. The disadvantage of fully heterostructured coupled quantum dots is that we cannot manipulate their confinement potential for achieving control over inter-dot interaction. But control over the number of electrons in a heterostructred quantum dot, even to the extent of single electron charging was achieved by fabricating them inside a field effect transistor kind of environment [126]. We believe the same could be achieved in the case of coupled self-assembled QDs also. This opens the possibility of using such structures for building quantum gates. The advantage of employing such structures over patterned gate is that we can achieve higher number of those basic units in a given area of two-dimensional semiconductor surface. This is due to the fact that the patterned gate based QDs have radial dimensions of the order of 100nm, whereas the self-assembled QDs can be fabricated in less than 10nm radius. The disadvantage of inability to control inter-dot interaction can be overcome by relying fully on an orthogonal external magnetic field as a handle. For simultaneous control of many quantum gate units, we require a nano-scale manipulation of magnetic induction, which is also a part of present day research [127; 128].

In this chapter, we study two electrons in laterally coupled heterostructured quantum dots with cylindrically symmetric step potential as well as coupled donor impurities in the presence of a magnetic field. We investigate the possibility of controlling exchange interaction in these structures by varying the strength of magnetic field. In Section 5.2, we present the theoretical discussion for the analysis of coupled quantum dots using methods from molecular physics. The results thus obtained such as the variation of exchange interaction with respect to the magnetic field and inter-dot separation etc. are presented and discussed in Section 5.3. Finally the chapter is concluded in Section 5.5.

5.2 Theory

In our analysis we consider a thin sheet of semiconductor material consisting of two cylindrically symmetric QDs having one electron each, laterally coupled to each other as shown in Fig. 5.1. In the first case we assume that the dot potentials are due to heterostructured confinements forming cylindrical step potentials. In the second case, we consider hydrogenic impurity potentials laterally aligned and coupled to each other. Our aim is to evaluate the exchange interaction strength between these electrons as a function of external magnetic field in the orthogonal direction, for a given inter dot separation. We make use of the variational principle in molecular physics namely, the Heitler-London (H-L) method and then refine these results by incorporating double occupancy states in each dot.

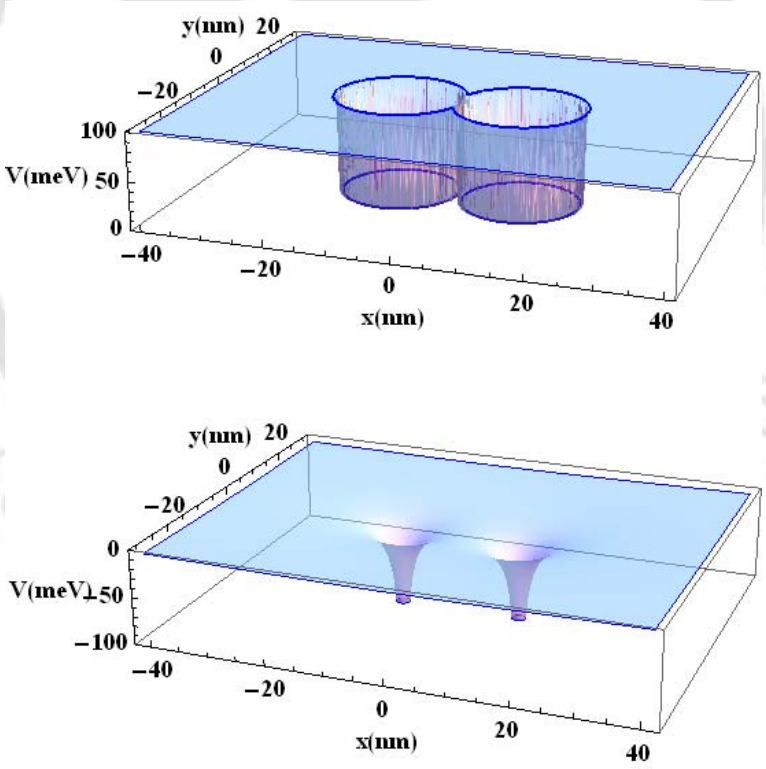

Figure 5.1: A perspective projection of the potential profile under consideration. (a) An approximate model potential for fully heterostructured coupled dots. The potential is taken as $V = 0$ inside the dots and $V = V_0$ outside the dots. (b) Model potential of coupled donor impurities.

In both cases we assume that the quantum dots are formed in a two dimensional electron gas (2DEG) and the whole analysis is done under the effective mass approximation. The Hamiltonian for the coupled system is then given by

$$\begin{aligned} H &= \sum_{i=1,2} h_i + \frac{q^2}{\kappa|\vec{r}_1 - \vec{r}_2|}, \\ h_i &= \frac{1}{2m_e}\left(\vec{p}_i + q\vec{A}(r_i)\right)^2 + V(r_i) + g\mu_B \vec{B}\cdot\vec{S}_i \end{aligned} \tag{5.1}$$

Here, the first term in the Hamiltonian involving h_i determines the dynamics of the independent electrons, which in turn breaks into kinetic energy of the electron, potential energy due to confinement and the interaction with external constant magnetic field. g is the electron g-factor and μ_B is the Bohr magneton. The second term in the Hamiltonian is the Coulomb interaction between the two electrons. We consider the magnetic field to be along z axis, which couples to the electric charge via the vector potential $\vec{A}(r) = \frac{B}{2}(-y, x, 0)$. The coupled QD confining potentials, as shown in Fig. 5.1 can be written as

$$V_I(x,y) = \begin{cases} 0, & \sqrt{(|x|-a)^2 + y^2} \leq r_0; \\ V_0, & \sqrt{(|x|-a)^2 + y^2} > r_0; \end{cases} \tag{5.2a}$$

$$V_{II}(x,y) = -\frac{q^2}{\kappa}\left(\frac{1}{\sqrt{(x+a)^2+y^2}} + \frac{1}{\sqrt{(x-a)^2+y^2}}\right) \tag{5.2b}$$

where, $V(x,y) = V_I(x,y)$ for the first case (heterostructure) and $V(x,y) = V_{II}(x,y)$ for the second case (donor impurity). V_0 is the step potential and r_0 is the radius of individual heterostructure dot. The centers of individual QDs are separated by a distance $2a$ and they are measured in units of r_0 in the case of heterostructure dots and $r_B = \frac{\hbar^2\kappa}{m_e q^2}$, the effective Bohr radius, in the case of impurity dots. We assume the inter-dot distance can be controlled experimentally, and the screening lengths of Coulomb interactions are very large compared to the dot dimensions.

The Hamiltonian in Eq. 5.1 is symmetric with respect to the exchange of particles, as electrons are indistinguishable. This leads to a condition on the orbital part of the total wavefunction that it should be either symmetric or anti-

symmetric. Since the total wave function of the two electron system must be anti-symmetric, this will introduce correlation between the spins through orbital degrees of freedom. The spin part of symmetric orbital wave function must be a singlet state and that of the anti-symmetric orbital wave function must be a triplet state. Since, the electrons will occupy only the lowest orbital eigen states of the total Hamiltonian at temperatures close to zero, we can write a generic two electron state as

$$|\psi(t)\rangle = C_1(t)\,|\psi_+\rangle\,|\chi_s\rangle + C_2(t)\,|\psi_-\rangle\,|\chi_t\rangle\,, \tag{5.3}$$

a superposition of the lowest singlet and triplet states. Which one of these is the ground state, as we will show, is determined by the magnitude of applied external magnetic field intensity. $|\psi_\pm\rangle$ is the orbital part and $\left|\chi_{s/t}\right\rangle$ is the spin part of the wavefunction. $C_1(t)$ and $C_2(t)$ are the probability amplitude for singlet and triplet states respectively at any given time t. In Schrodinger picture, the a time evolution from t_0 to t can be written as

$$\begin{aligned} |\psi(t)\rangle &= e^{-\frac{i}{\hbar}H(t-t_0)}\,|\psi(t_0)\rangle \\ &= C_1(t_0)e^{-\frac{i}{\hbar}E_+(t-t_0)}\,|\psi_+\rangle\,|\chi_s\rangle + C_2(t_0)e^{-\frac{i}{\hbar}E_-(t-t_0)}\,|\psi_-\rangle\,|\chi_t\rangle \end{aligned} \tag{5.4}$$

where E_+ and E_- are singlet and triplet energies respectively. This can be further simplified by writing in terms of exchange energy $J = E_- - E_+$ and ignoring the global phase of the state as

$$|\psi(t)\rangle = C_1(t_0)\,|\psi_+\rangle\,|\chi_s\rangle + C_2(t_0)e^{-\frac{i}{\hbar}J(t-t_0)}\,|\psi_-\rangle\,|\chi_t\rangle\,. \tag{5.5}$$

From above equation, it is clear that any non-zero exchange interaction will introduce a relative phase $Jt/\hbar$ between the singlet and triplet states. This is useful for realizing single qubit gates in the case of encoded two-spin qubits and two qubit gates in single spin qubits. The above relative phase is usually expressed in terms of Heisenberg's effective spin-spin interaction Hamiltonian

$$H_s = J\frac{\vec{S}_1 \cdot \vec{S}_2}{\hbar^2}. \tag{5.6}$$

In the following we calculate the magnitude of J as a function of magnetic field intensity for both cases of coupled quantum dots. This involves the estimation of E_- and E_+ from the two-electron orbital wave function.

5.2.1 Heitler-London Approximation

At first we consider the simplest approximation of one electron sitting in each quantum dot. In Heitler-London (H-L) approximation, this picture is constructed out of single electron ground states of the left and right single quantum dots. If $\varphi_L(\vec{r})$ is the ground state of the left QD and $\varphi_R(\vec{r})$ is the ground state of the right QD, the orbital part of the two electron wavefunction is written as

$$|\psi_\pm\rangle = \frac{\varphi_L(\vec{r_1})\varphi_R(\vec{r_2}) \pm \varphi_R(\vec{r_1})\varphi_L(\vec{r_2})}{\sqrt{2(1 \pm S^2)}}. \tag{5.7}$$

The symmetric combination correspond to singlet ground state ψ_+ and the anti-symmetric combination correspond to triplet ground state ψ_-. The denominator of the above equation is the normalization factor where, S is the overlap between φ_L and φ_R. The value of energies for singlet and triplet ground state can then be written as

$$E_\pm = \langle \psi_\pm | H | \psi_\pm \rangle . \tag{5.8}$$

After simplification, this becomes

$$\begin{aligned} E_\pm = \frac{1}{1 \pm S^2} \Big\{ 2\epsilon \left(1 \pm S^2\right) + 2 \langle \varphi_L(r) | V_r(r) | \varphi_L(r) \rangle \pm 2S \langle \varphi_L(r) | V_l(r) | \varphi_R(r) \rangle \\ + \left\langle \varphi_L(r_1)\varphi_R(r_2) \left| \frac{q^2}{\kappa|\vec{r_1} - \vec{r_2}|} \right| \varphi_L(r_1)\varphi_R(r_2) \right\rangle \\ \pm \left\langle \varphi_L(r_1)\varphi_R(r_2) \left| \frac{q^2}{\kappa|\vec{r_1} - \vec{r_2}|} \right| \varphi_R(r_1)\varphi_L(r_2) \right\rangle \Big\} . \end{aligned} \tag{5.9}$$

In the above expression, ϵ is the single electron energy for the single dot ground state, $V_r(r) = V(r) - V_L(r)$ and $V_l(r) = V(r) - V_R(r)$ are the residue potentials; V_L and V_R are the confining potentials for the single QD at the left and right positions, respectively. Shifting the single particle ground state orbital toward left and right by transforming $(x, y) \rightarrow (x \pm a, y)$ will also change the gauge

of the problem. This is then fixed by an inverse gauge transformation $\vec{A} = \frac{B}{2}(-y, x \pm a, 0) \rightarrow \vec{A} = \frac{B}{2}(-y, x, 0)$, which will introduce a phase factor on the shifted orbitals as shown below.

$$\varphi_{L/R}(x, y) = e^{\pm iya/2l_B^2}\varphi(x \pm a, y) \tag{5.10}$$

where $l_B = \sqrt{\hbar/qB}$ is the cyclotron radius corresponding to the lowest Landau orbital.

5.2.2 Weinbaum Approximation

A method of obtaining better estimation of ground state energy for hydrogen molecule was proposed by Weinbaum [129], where the double occupancy states at each H-atom was also considered. In a similar way, we try to improve the results for our coupled QDs. Since we consider only the ground state from each QD, the doubly occupied two-electron states formed from them are always singlet states. Thus our effective Hilbert space is spanned by three singlet states having the same antisymmetric spatial configuration, and three triplet states having distinct symmetric spatial configurations. The four spatial parts of the wavefunctions are listed below.

$$\Phi_L^d(\vec{r}_1, \vec{r}_2) = \varphi_L(\vec{r}_1)\varphi_L(\vec{r}_2) \tag{5.11a}$$

$$\Phi_R^d(\vec{r}_1, \vec{r}_2) = \varphi_R(\vec{r}_1)\varphi_R(\vec{r}_2) \tag{5.11b}$$

$$\Phi_\pm^{(1,1)}(\vec{r}_1, \vec{r}_2) = \frac{\varphi_L(\vec{r}_1)\varphi_R(\vec{r}_2) \pm \varphi_R(\vec{r}_1)\varphi_L(\vec{r}_2)}{\sqrt{2(1 \pm S^2)}} \tag{5.11c}$$

In the above, the superscript d denotes double occupancy and superscript $(1, 1)$ denotes single occupancy states. All the above orbital states are written in normalized form. As the spin part of the wavefunction $\left(|\uparrow\uparrow\rangle, |\downarrow\downarrow\rangle, \frac{|\uparrow\downarrow\rangle \pm |\downarrow\uparrow\rangle}{\sqrt{2}}\right)$ are all orthonormal to one another, the three triplet states are orthogonal to each other and to the singlet state. However the three singlet states in the six dimensional basis are not orthogonal. Therefore, we need to solve a generalized eigen value problem in applying the present linear variational analysis. This is written as

shown in the following equation.

$$[H]\{C\} = E\,[G]\{C\} \tag{5.12}$$

Here, $[H]$ is the two-electron Hamiltonian in Eq. 5.1 written in the basis of three singlet orbital states shown in Eq. 5.11 viz. Φ_L^d, Φ_R^d and $\Phi_+^{(1,1)}$. Due to the symmetry of the problem, we have

$$H_{11} = H_{22},$$

$$H_{12} = H_{21},$$

$$H_{13} = H_{23} = H_{31} = H_{32}.$$

$\{C\}$ is a column matrix corresponding to the linear variational parameters that are to be determined and E is the unknown energy eigen value. $[G]$ is the overlap matrix written in the same basis and its expression is given by

$$[G] = \begin{bmatrix} 1 & S^2 & \frac{\sqrt{2}}{\sqrt{1+S^2}}S \\ S^2 & 1 & \frac{\sqrt{2}}{\sqrt{1+S^2}}S \\ \frac{\sqrt{2}}{\sqrt{1+S^2}}S & \frac{\sqrt{2}}{\sqrt{1+S^2}}S & 1 \end{bmatrix}. \tag{5.13}$$

The diagonalization of Eq. 5.12 assumes the minimization of the energy of the singlet ground state. We expect that the introduction of double occupancy states into the analysis improves the value of the exchange energy.

5.3 Results and Discussion

We have numerically evaluated all the integrals involved in the Heitler-London and Weinbaum methods using the MATHEMATICA package. The diagonalization of Eq. 5.12 was also done numerically. The energy of the lowest singlet state is subtracted from the energy of the triplet state to evaluate the strength of exchange interaction coefficient. This is then plotted as a function of external magnetic field strength for a given inter-dot distance $2a$. The value of $2a$ for coupled heterostructured QD is expressed in terms of the radius of the dot r_0. In

our analysis, we kept the radius same ($r_0 = 15$nm) for both dots. For the impurity based QDs, $2a$ is measured in terms of the effective Bohr radius r_B. The value of r_B depends upon the effective mass and dielectric constant of the material. Since we have considered GaAs as the host material, its value turns out to be around 10nm. The results obtained for both cases of coupled QDs suppressing the contribution from Zeeman interaction are shown in figures 5.2 and 5.3.

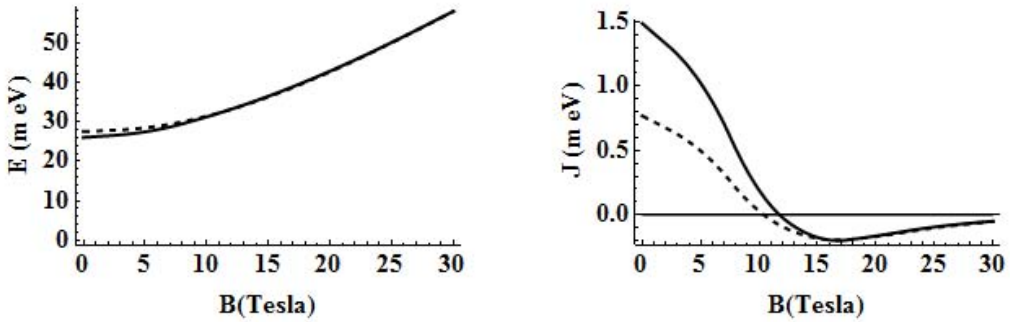

Figure 5.2: The variation of singlet (continuous) and triplet (dashed) energy levels [left] exchange interaction coefficient [right] for coupled heterostructured QD as a function of magnetic field strength. Here, an inter-dot separation of $2a = 1.4r_0$ is considered under H-L method (dotted) and Weinbaum method (continuous).

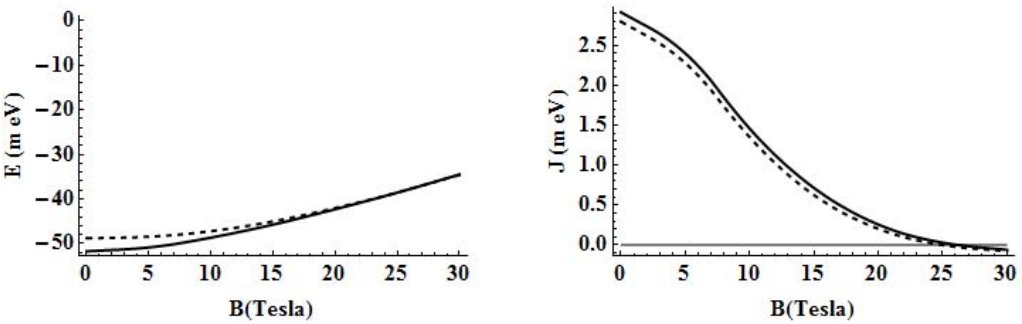

Figure 5.3: The variation of singlet (continuous) and triplet (dashed) energy levels [left] exchange interaction coefficient [right] for coupled impurity QDs as a function of magnetic field strength. Here, an inter-dot separation of $2a = 1.6r_B$ is considered under H-L method (dotted) and Weinbaum method (continuous).

It may be noticed from Fig. 5.2 that the inclusion of double occupancy states in the analysis gives significant improvement in the calculation of exchange en-

ergy. Since the ground state energy of the singlet state is further minimized through a non-zero probability for double occupancies, exchange energy is enhanced whenever its value is actually positive and suppressed whenever it is negative, in comparison to H-L results. On the other hand, for the case of coupled impurity potentials there exist no significant difference between the results obtained from H-L and Weinbaum methods. This may be attributed to the presence of singularity in the single quantum dot potentials. For a given inter-dot separation, presence of singularity would minimize the probability of double occupancy in either QDs.

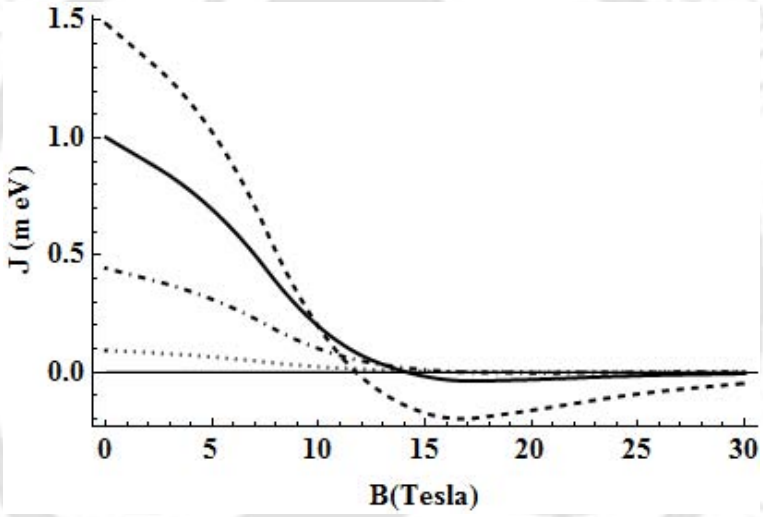

Figure 5.4: The variation of exchange interaction coefficient for coupled heterostructured QDs as a function of magnetic field strength. The different graphs corresponds to inter-dot separations $2a = 1.4r_0$ (dashed), $2a = 1.6r_0$ (continuous), $2a = 1.8r_0$ (dot-dashed) and $2a = 2r_0$ (dotted). All results are due to Weinbaum method.

The Fig. 5.4 shows the variation of exchange interaction with respect to magnetic field strength for different inter-dot separations. It is easily seen from the graph that the strength of exchange interaction decreases with the increase of inter-dot separation. This behavior is expected as the magnitude of inter-dot tunneling is inversely proportional to $2a$. It may also be noticed that the magnetic field at which singlet-triplet cross-over occurs is also a function of inter-dot separation. For example when $2a = 1.6r_0$, at 14 Tesla, the singlet and the

triplet state are degenerate, and therefore their time evolution will introduce no phase difference between the states. Fig. 5.5 shows the variation of exchange

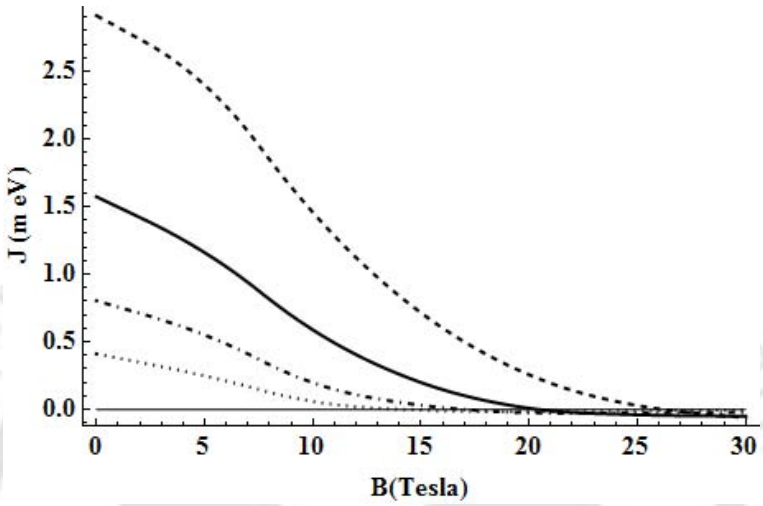

Figure 5.5: The variation of exchange interaction coefficient for coupled impurity QDs as a function of magnetic field strength. The different graphs corresponds to inter-dot separations $2a = 1.4r_B$ (dashed), $2a = 1.6r_B$ (continuous), $2a = 1.8r_B$ (dot-dashed) and $2a = 2r_B$ (dotted). All results are due to Weinbaum method.

interaction for coupled impurities at different inter-dot separations. One major difference that may be noticed here is that the singlet-triplet crossing happens at lower magnetic field strengths for larger inter-dot separations.

5.4 Application in Quantum Computation

The results obtained in the above section may be utilized for constructing useful quantum gate operation. To achieve this, we must be able to switch off and on the exchange interaction between the qubits. This can only be implemented by switching the magnetic flux densities between values that correspond to $J_{ex} = 0$ and some other point where it is non-zero. We already noticed that the magnetic field at which exchange interaction coefficient goes to zero depends upon the inter-dot separation. Yet another parameter that can determine the value of magnetic field at which singlet-triplet phase transition occurs is the radius of single dot confinement potential. This, in the case of hydrogenic impurity based

confinement, is a parameter fixed by the properties of the host material. On the other hand, for cylindrical QDs, it is possible to have confinement radii over a large range. For larger radius of QDs, the singlet-triplet transition in ground state is expected to happen at smaller magnetic flux densities. This helps us to neglect the contribution from Zeeman effect and treat all triplet states on the same footing. But for smaller QD radius, the singlet-triplet transition occurs at larger values of external magnetic field. Therefore, we cannot any longer neglect the splitting of triplet energy states as can be verified from Fig. 5.6. To demonstrate SWAP-gate operation between the spin-qubits, it is enough to show that for all product and entangled states, the spins could be interchanged after a period of gate-operation time, τ_g. Since the singlet and three triplet states are constants of motion, the time evolution of a generic state in this reduced Hilbert space could be written as

$$|\psi(t)\rangle = C_1 |\psi_+\rangle \frac{[|\uparrow\downarrow\rangle - |\downarrow\uparrow\rangle]}{\sqrt{2}} + C_2 e^{-\frac{i}{\hbar}J_0 t} |\psi_{-0}\rangle \frac{[|\uparrow\downarrow\rangle + |\downarrow\uparrow\rangle]}{\sqrt{2}} + C_3 e^{-\frac{i}{\hbar}J_+ t} |\psi_{-+}\rangle |\uparrow\uparrow\rangle + C_4 e^{-\frac{i}{\hbar}J_- t} |\psi_{--}\rangle |\downarrow\downarrow\rangle \tag{5.14}$$

where the subscripts -0, $-+$, $--$ correspond to the three triplet states and J_0, J_+, J_- are their respective exchange interaction energies.

Case-(i): $C_1 = C_2 = 0$; ($C_3 = 0$ and $C_4 = 1$) or ($C_3 = 1$ and $C_4 = 0$)
In this case, the non-zero term will only pick up a global phase after τ_g time, maintaining the expectation of $\hat{S}_z$ as $\mp\hbar$, respectively.

Case-(ii): ($C_1 = C_2 = 1$) or ($C_1 = -1; C_2 = 1$); $C_3 = C_4 = 0$
In this case, a relative phase will be picked up between the singlet and the triplet state, which when equal to π will result in a SWAP of spin states between individual electrons. This can be done by operating the system at a magnetic field strength, B_c where singlet and triplet states have the same energy, and then switching the field to a non-zero exchange interaction energy and then letting the system evolve for a sufficient period of time, τ_g.

Case-(iii): $C_1 = C_2 = 0$; $C_3 = C_4 = 1$

This correspond to the case of a completely entangled initial state viz. the Bell state. Now if the magnetic field is switched from $B = B_c$ to $B = 0T$, then letting the system evolve for a same amount of time τ_g, the state will pick up only a global phase as the energy difference between the triplet states is equal to zero when $B = 0$.

Thus we have demonstrated swapping of spin states for all important cases of initial two-electron states. From Fig. 5.6, it may be seen that at $B = 12\text{T}{=}B_c$, the value of J_0 goes to zero and at $B = 0\text{T}$, it is 1.6meV. Therefore, switching the system between these operating points, we can achieve a $SWAP$ gate operation between the two qubits. The time required to perform a $SWAP$ operation corresponds to a phase variation of π radians and is given as $\tau_g = \pi\hbar/J_0$. For $J_0 = 1.6\text{meV}$, the value of τ_g turns out to be 1.29ps. The switching of exchange interaction must be slow enough (adiabatic) to prevent the excitation of electrons into higher energy states. This can be done by appropriately fixing the inter-dot distance.

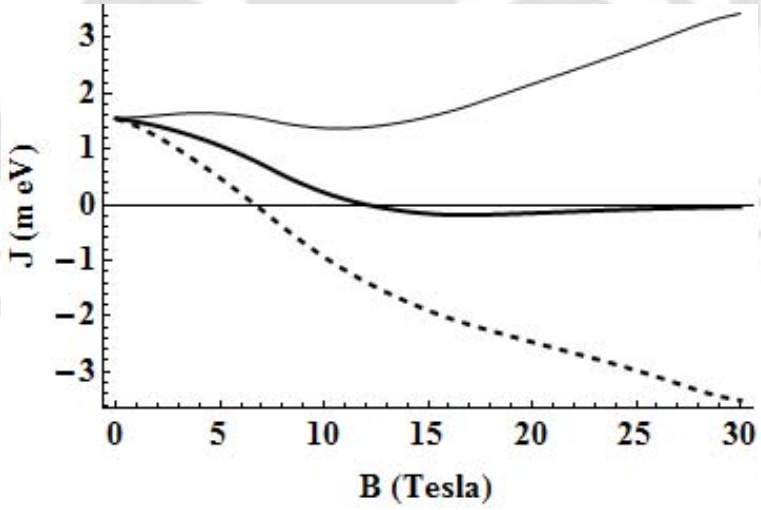

Figure 5.6: The variation of exchange interaction coefficient for coupled heterostructured QDs as a function of magnetic field strength. The different graphs corresponds to exchange interaction between the lowest singlet state and the three non-degenerate triplet states viz. J_+ (continuous thin), J_0 (continuous thick), and J_- (dashed) for an inter-dot separations $2a = 1.4r_B$.

5.5 Conclusion

In this chapter, we studied the exchange interaction properties of two kinds of coupled quantum dots. The first case involves fully heterostructured quantum confinements that are approximated with cylindrically symmetric step potentials. In the second case, we considered electrons confined in hydrogenic donor impurity potentials. In both cases, we modeled the system using a two dimensional effective mass approximation and the analysis was carried out using Heitler-London and Weinbaum methods of molecular physics. It was observed that the Weibaum method significantly improves the calculation of exchange energy for the heterostructured case over the H-L method. In contrast, for the impurity based coupled QDs, the results due to H-L method are comparable with the Weinbaum method. We have plotted the dependency of exchange interaction with respect to magnetic field for various inter-dot separations. Compared to the patterned gate based switching of exchange interaction, we do not have any control over the ability to change the inter-dot separation. The value of $2a$ is fixed in both cases of the coupled QDs we analyzed in this chapter. But this difficulty can be overcome by depending on the strength of external magnetic field for controlling the exchange interaction. Yet another difficulty with the present scenario is that the exchange interaction goes to zero only at high magnetic field strengths where the Zeeman interactions cannot be neglected anymore. This will result in a splitting of triplet energy levels as shown in Fig. 5.6. Important quantum gate operations can still be realized by operating the system near a magnetic field strength where the ground state switches from singlet to the lowest triplet state.

Chapter 6

Decoherence of a single electron spin qubit

6.1 Introduction

Decoherence, the phenomenon through which a superposition state of a quantum system loses coherent relationship between its components, has been studied for many decades now from both the fundamental standpoint [130; 131; 132] and also from the point of view of quantum technologies. Since the Loss-DiVincezo proposal for quantum computation, plenty of theoretical [38; 133; 134; 135; 136] as well as experimental investigations [43; 137; 138] have been performed to understand the dynamics of decoherence in semiconductor quantum dots. Various factors that contribute to decoherence in such systems were identified and their relative magnitudes were estimated [139; 140]. At sufficiently low temperature, the contribution to decoherence due to phonons can be neglected. This leaves hyperfine interactions between the electron and its surrounding nuclei as the dominant mechanism for spin decoherence [141]. In most applications, we are interested only in the quantum state of the electrons and not on the state of environment surrounding it.

The exact analysis of decoherence involves too many degrees of freedom and it is often very complicated when a complete mathematical model of the combined system-environment dynamics is taken into account. There are two ways by

which we can surmount this problem; either by using master equations, which are dynamic mappings within the reduced space of the system [142; 143], or by employing approximate models that are simple enough to be tackled exactly [144; 145]. For the present analysis, we employ a simplistic model due to F. M. Cucchietti et al. [146], where the total Hamiltonian of a central spin interacting with a spin bath is given by

$$\hat{H} = \Delta\hat{\sigma}_x + \hat{\sigma}_z \otimes \sum_{k=1}^{N} J_k \hat{\sigma}_z^{(k)} \tag{6.1}$$

Here, the first term represents the Hamiltonian of the central spin in the absence of any interaction with the spin–bath. The strength of this term is denoted by Δ, which is a parameter that has the dimension of energy. The second term represents the contribution to the Hamiltonian due to the interaction with the nuclear spins in the spin–bath, where J_k denotes the strength of hyperfine interaction between the central electron spin and k^{th} nuclear spin of the bath.

This chapter is organized as follows. In Section 6.2, we present the theoretical steps involved in the analysis of decoherence of a single electron spin in various quantum dot geometries. Then, in Section 6.3, we present and discusses the results of the analysis. Finally in Section 6.4, the conclusion is presented.

6.2 Theory

The quantum system of our interest is a central electron spin interacting with a nuclear spin bath inside a quantum dot. In the Hamiltonian shown in Eq. (6.1), the first term corresponds to the system Hamiltonian and the second corresponds to the interaction Hamiltonian. For simplicity, the interactions between nuclear spins are neglected. We assume that the spin bath consists of N nuclear spins and J_k is the hyperfine interaction strength between the k^{th} nucleus and the central electron. To begin our analysis, we consider the initial system-bath state to be a product state, given by

$$|\psi(0)_{SE}\rangle = |\psi_S(0)\rangle\,|\psi_E(0)\rangle \tag{6.2}$$

Expressing in a basis that diagonalizes the interaction Hamiltonian, this becomes

$$|\psi(0)_{SE}\rangle = (a\,|0\rangle + b\,|1\rangle) \sum_{n=0}^{2^N-1} c_n\,|n\rangle \tag{6.3}$$

Where, a and b are complex probability amplitudes for the electron spin to be found in up ($|0\rangle$) and down ($|1\rangle$) states and c_n is the probability amblitude for the product state ($|n\rangle$) of the nuclear spin bath containing N nuclear spins. Since the Hamiltonian in Eq. (6.1) is time independent,

$$|\psi(t)_{SE}\rangle = e^{-\frac{i}{\hbar}\hat{H}t}\,|\psi(0)_{SE}\rangle\,.$$

Following the same procedure as in reference [146], the system density matrix at time t can be written as

$$\hat{\rho}_S(t) = \mathrm{Tr}_E\left(\hat{\rho}_{SE}(t)\right) = \sum_{n=0}^{2^N-1} |c_n|^2 \left(\hat{U}_n \hat{\rho}_S(0) \hat{U}_n^+\right) \tag{6.4}$$

where

$$\hat{U}_n = \hat{I}\,\cos(\Omega_n t) - \frac{i}{\hbar\Omega_n}\left(\Delta\hat{\sigma}_x + \epsilon_n\hat{\sigma}_z\right)\sin(\Omega_n t) \tag{6.5}$$

and

$$\epsilon_n = \textstyle\sum_{k=1}^{N}(-1)^{n_k} J_k \quad ; \quad \Omega_n = \frac{\sqrt{\Delta^2+\epsilon_n^2}}{\hbar}. \tag{6.6}$$

so that ϵ_n is the environmental energy eigen value corresponding the eigen state $|n\rangle$, and n_k =0 or 1 depending on whether k^{th} nuclear spin within N–particle state $|n\rangle$ is in up or down state and $\hat{I}$ is the identity operator. Expanding $\hat{\rho}_S(t) = \frac{1}{2}\left(\hat{I} + \vec{P}(t)\cdot\vec{\hat{\sigma}}\right)$, the polarization components becomes

$$P_j(t) = \sum_{n=0}^{2^N-1} |c_n|^2 P_j^n(t) \tag{6.7}$$

where $P_j^n(t) = \mathrm{Tr}_S\left(\hat{\sigma}_j \hat{U}_n \hat{\rho}_S(0) \hat{U}_n^+\right)$ and $\hat{\sigma}_j$ is the j–component of the Pauli matrix. For completely random environmental state with zero net polarization, all eigen states are equally likely and therefore, $|c_n|^2 = \frac{1}{2^N}$ for all n. Further, in the limit of large N–value, we can approximate the summation in Eq. (6.7) with an

integral as

$$P_j(t) \cong \frac{1}{2^N} \int_0^{2^N} P_j^n(t)\, dn \tag{6.8}$$

It is more feasible to evaluate the integral in the energy domain. Thus by changing the integration variable from n to ϵ, we get

$$P_j(t) = \frac{1}{2^N} \int_{\epsilon=\epsilon_{\min}}^{\epsilon_{\max}} \tilde{P}_j(t,\epsilon)\, D(\epsilon)\, d\epsilon \tag{6.9}$$

where the expressions for $\tilde{P}_j(t,\epsilon)$ are given as

$$\begin{aligned}
\tilde{P}_x(t,\epsilon) = &\quad P_x(0)\frac{\Delta^2 + \epsilon^2\cos(2\Omega_\epsilon t)}{\hbar^2\Omega_\epsilon^2} - P_y(0)\frac{\epsilon\sin(2\Omega_\epsilon t)}{\hbar\Omega_\epsilon} + P_z(0)\frac{2\Delta\epsilon\sin^2(\Omega_\epsilon t)}{\hbar^2\Omega_\epsilon^2} \\
\tilde{P}_y(t,\epsilon) = &\quad P_y(0)\cos(2\Omega_\epsilon t) + [P_x(0)\epsilon - P_z(0)\Delta]\frac{\sin(2\Omega_\epsilon t)}{\hbar\Omega_\epsilon} \\
\tilde{P}_z(t,\epsilon) = &\quad P_z(0)\frac{\epsilon^2 + \Delta^2\cos(2\Omega_\epsilon t)}{\hbar^2\Omega_\epsilon^2} + P_x(0)\frac{2\Delta\epsilon\sin^2(\Omega_\epsilon t)}{\hbar^2\Omega_\epsilon^2} + P_y(0)\frac{\Delta\sin(2\Omega_\epsilon t)}{\hbar\Omega_\epsilon}
\end{aligned} \tag{6.10}$$

and $\epsilon_{\min} = -\epsilon_{\max} = -\sum_{k=1}^{N} J_k$, and $D(\epsilon)$ is the density of states. Since there exists 2^N number of environmental eigen states, $D(\epsilon)$ can be written as

$$D(\epsilon) = 2^N f(\epsilon). \tag{6.11}$$

where $f(\epsilon)$ is the probability density function of the total energy of the nuclear spin bath and it can be evaluated using the central limit theorem (CLT). The energy contribution from each nuclear spin corresponds to an individual random variable that can take only one of the two possible values, viz. $\pm J_k$, say with probabilities $|a_k|^2$ and $|b_k|^2$ respectively. For a completely depolarized environment, we assume $|a_k|^2 = |b_k|^2 = \frac{1}{2}$ for all k. The total energy variable ϵ, due to all nuclear spins is equal to the sum of all individual energy variables and its probability distribution becomes a Gaussian function due to CLT, given by

$$f(\epsilon) = \frac{1}{\sqrt{2\pi}\Lambda}\exp\left(-\frac{\epsilon^2}{2\Lambda^2}\right) \tag{6.12}$$

with

$$\epsilon = \pm J_1 \pm J_2 \pm \ldots \pm J_N \tag{6.13}$$

and

$$\Lambda^2 = \lambda_1^2 + \lambda_2^2 + \ldots + \lambda_N^2 \tag{6.14}$$

where λ_k is the standard deviation of the individual random variable corresponding to the energy contribution from k^{th} nuclear spin. Notice from Eq. (6.12) that the mean of the composite variable $\bar{\epsilon}$ is zero as the individual means $J_k(|a_k|^2-|b_k|^2)$ are all zero. But the square of the standard deviation of ϵ is equal to the sum of squares of the individual standard deviations as given in Eq. (6.14). Substituting for $D(\epsilon)$ in Eq. (6.9), we get

$$P_i(t) = \frac{1}{\sqrt{2\pi}\Lambda} \int_{\epsilon=\epsilon_{min}}^{\epsilon_{max}} \tilde{P}_i(t,\epsilon) \exp\left(-\frac{\epsilon^2}{2\Lambda^2}\right) d\epsilon. \tag{6.15}$$

For a completely depolarized environment, we have

$$\lambda_k^2 = (|a_k|^2+|b_k|^2)J_k^2 - (J_k(|a_k|^2-|b_k|^2))^2 = J_k^2.$$

Therefore, if the coupling strength J_k is a function of position of the individual nuclei, so is its standard deviation. The Hamiltonian for hyperfine interaction between k^{th} nucleus and central electron spin can be written as

$$\hat{H}_{hf}^{(k)} = -\frac{2}{3}\mu_0 \left\langle \vec{\mu}_e \cdot \vec{\mu}_n^{(k)} \right\rangle |\psi(\vec{r}_k)|^2 \tag{6.16}$$

where μ_0 is the permeability of free space, $\vec{\mu}_e$ and $\vec{\mu}_n^{(k)}$ are the magnetic moments of the electron and the k^{th} nucleus, respectively, and $|\psi(\vec{r}_k)|^2$ is the probability density for finding an electron at position $\vec{r}_k$.

Substituting $\vec{\mu}_e = -g_e\mu_B\frac{\vec{S}}{\hbar}$ and $\vec{\mu}_n^{(k)} = g_N\mu_N\frac{\vec{I}^{(k)}}{\hbar}$, and considering only the z-z interaction, we get

$$\hat{H}_{hf}^{(k)} = J_k\, \hat{\sigma}_z \otimes \hat{\sigma}_z^{(k)}. \tag{6.17}$$

Here $\vec{S}$ and $\vec{I}^{(k)}$ are the electron and nuclear spin operators, and the strength of interaction J_k is given by

$$J_k = \kappa|\Psi(\vec{r_k})|^2. \tag{6.18}$$

with $|\psi(\vec{r_k})|^2 = \eta|\Psi(\vec{r_k})|^2$ and

$$\kappa = \frac{2}{3\hbar^2}\mu_0 g_e g_N \mu_B \mu_N \eta,$$

g_e and g_N are the electron and nuclear g-factors, μ_B and μ_N are the Bohr and nuclear magnetons, η is the square of Bloch wave amplitude, and $\Psi(\vec{r_k})$ is the amplitude of electron envelope function. From Eq. (6.18) it is clear that $J_k = J(\vec{r_k})$ and therefore the expression for composite standard deviation in Eq. (6.14) can be written as

$$\Lambda^2 = \sum_{k=1}^{N} J_k^2 = \int_V J^2(\vec{r})\,\frac{d\tau}{d^3} \tag{6.19}$$

where the integration is performed over V, the volume of the nuclear spin bath, and d is the inter-nuclear distance. Thus we notice here that the spread of $D(\epsilon)$ function in Eq. (6.11) depends on the geometrical arrangement of the nuclei around the central spin. In the following, we consider three distinct quantum dot geometries and analyze how Λ^2 depends on the dimension of the nuclear spin bath. In all cases, we assume $Ga_{1-x}Al_xAs$ quantum dot and that the electron is sitting in its ground state. The value of κ in Eq. (6.18) is evaluated to be $1.62\,\mu\text{eV}\,\text{nm}^3$ after substituting for various parameters as shown in Appendix A.

- First, we consider a quantum dot inside a 3–dimensional nuclear spin bath of infinite extent. Assuming a spherically symmetric harmonic oscillator potential, the interaction strength can be written down as

$$J(r,\theta,\phi) = \kappa\left(\frac{1}{\sqrt{\pi}a_B}\right)^3 e^{-\left(\frac{r}{a_B}\right)^2}. \tag{6.20}$$

  where $a_B = \sqrt{\frac{\hbar}{m_e\omega}}$ is the effective Bohr radius of the ground state electron inside the 3D oscillator. For a_B = 20nm, 50nm and 100nm, we get Λ = 30.82 neV, 7.80 neV and 2.76 neV, respectively. Here 1 neV= 10^{-9}eV.

- Secondly, we consider a quantum dot embedded in a 2–dimensional (thin sheet) nuclear spin bath extending to infinity. Assuming a symmetric parabolic confinement potential in the radial direction, and no variation in the confined z-direction, the interaction strength can be written down in cylindrical co-

ordinates as

$$J(\rho,\phi,z)=\kappa\left(\frac{2}{\pi a_B^2 d_z}\right)e^{-\left(\frac{\rho}{a_B}\right)^2}\sin^2\left(\frac{\pi z}{d_z}\right). \tag{6.21}$$

For a sheet of thickness $d_z = 5$nm and $a_B = 20$nm, 50nm and 100nm, we get $\Lambda = 119.52\,\text{neV}, 47.81\,\text{neV}$ and $23.90\,\text{neV}$, respectively.

- Finally, we consider a quantum dot in a 1–dimensional (thin wire) nuclear spin bath environment extending to infinity. The strength of interaction can be written in Cartesian coordinates as

$$J(x,y,z)=\kappa\left(\frac{4}{\sqrt{\pi}a_B d_x d_y}\right)\sin^2\left(\frac{\pi x}{d_x}\right)\sin^2\left(\frac{\pi y}{d_y}\right)e^{-\left(\frac{z}{a_B}\right)^2}. \tag{6.22}$$

We assume a square cross–section for the wire with $d_x = d_y = 5$nm, and parabolic confinement potential along the z direction and correspondingly we obtain $\Lambda = 463.51\,\text{neV}, 293.15\,\text{neV}$ and $207.29\,\text{neV}$ for $a_B = 20$nm, 50nm and 100nm, respectively.

With the obtained value of Λ in each case, we now proceed to evaluate $\varsigma(t)$, the trace of the square of reduced density matrix, to quantitatively monitor the decoherence dynamics. This can be written in terms of polarization components as

$$\varsigma(t)=\text{Tr}\rho_S^2(t)=\frac{1}{2}\left(1+P_x^2(t)+P_y^2(t)+P_z^2(t)\right) \tag{6.23}$$

where the polarization components are given by Eq. (6.15) and its form, after simplification, becomes

$$\begin{aligned}
P_x(t)&=\sqrt{\tfrac{2}{\pi}}\int_{v=0}^{\infty}P_x(0)\left[\tfrac{u^2}{u^2+v^2}+\tfrac{v^2}{u^2+v^2}\cos\left(\tfrac{2t\sqrt{u^2+v^2}}{\hbar/\Lambda}\right)\right]e^{-v^2/2}dv,\\
P_y(t)&=\sqrt{\tfrac{2}{\pi}}\int_{v=0}^{\infty}\left[P_y(0)\cos\left(\tfrac{2t\sqrt{u^2+v^2}}{\hbar/\Lambda}\right)-P_z(0)\tfrac{u}{\sqrt{u^2+v^2}}\sin\left(\tfrac{2t\sqrt{u^2+v^2}}{\hbar/\Lambda}\right)\right]e^{-v^2/2}dv,\\
P_z(t)&=\sqrt{\tfrac{2}{\pi}}\int_{v=0}^{\infty}\left[P_y(0)\tfrac{u}{\sqrt{u^2+v^2}}\sin\left(\tfrac{2t\sqrt{u^2+v^2}}{\hbar/\Lambda}\right)-P_z(0)\tfrac{v^2+u^2\cos\left(\frac{2t\sqrt{u^2+v^2}}{\hbar/\Lambda}\right)}{u^2+v^2}\right]e^{-v^2/2}dv.
\end{aligned} \tag{6.24}$$

Here we used $u = \Delta/\Lambda$ and $v = \epsilon/\Lambda$ to normalize the energy variable for making the integration variable independent of units. For a completely decohered state, $\varsigma = 1/2$, whereas for a completely coherent state, $\varsigma = 1$. Therefore, a partially

coherent state, we will have $0.5 < \varsigma(t) < 1$.

6.3 Results and Discussion

The integrals in Eq. (6.24) were evaluated numerically using MATHEMATICA software. Fig. 6.1 shows the plots of $\varsigma(t)$ when $P_x(0) = 1$ and $P_y(0) = P_z(0) = 0$. It is interesting to note that when u is very large, no decoherence takes place in this case. This is because, the initial state is an eigen state of the system–Hamiltonian and it completely dominates the evolution of the electron spin state in comparison to the weak environmental interaction term. For medium values of u, we observe that $\varsigma(t)$ reaches a steady-state value after a characteristic time, the magnitude of which is determined by the time-independent part of the integral in the first equation in Eq. (6.24). When $u = 0$, we observe complete decoherence, as the interaction term alone governs the dynamics of state evolution, for which the present initial state is not an eigen state. We also see oscillations in the decoherence process, whose frequency monotonically increases with the value of u, as expected from the time dependent part of the integrand.

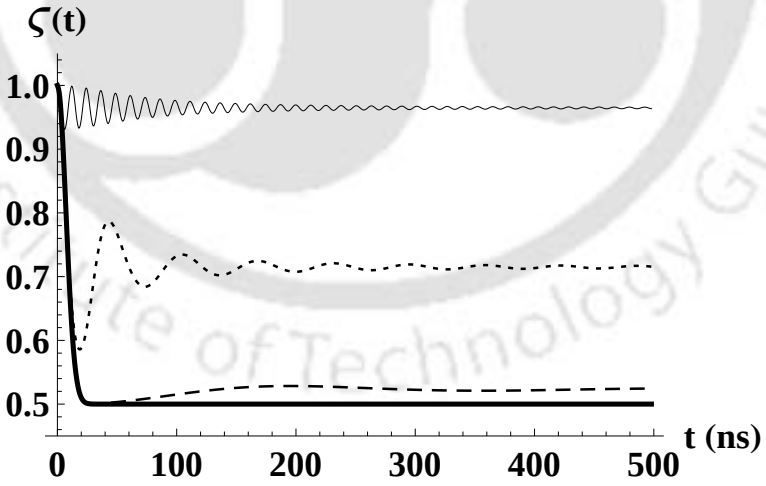

Figure 6.1: The time development of decoherence when $|\psi_S(0)\rangle = \frac{1}{\sqrt{2}}(|0\rangle + |1\rangle)$. The continuous–thick, dashed, dotted and continuous–thin curves corresponds to $u = 0$, $u = 0.2$, $u = 1$ and $u = 5$ respectively.

In the present case, for $u = 0$, the expression for $\varsigma(t)$ simplifies to

$$\varsigma(t) = \frac{1}{2}\left(1 + e^{-(2\Lambda/\hbar)^2 t^2}\right). \tag{6.25}$$

so that we observe a square-exponential decay with respect to time, as also can be seen from Fig. 6.1. From Eq. (6.25), we define a characteristic decoherence time, τ_D as the time the system takes for $\varsigma(t)$ to reach $1/e$ of the difference between the initial and final value. Thus we get

$$\tau_D = \frac{\hbar}{2\Lambda}. \tag{6.26}$$

The value of τ_D for three, two and one dimensional nuclear baths were obtained as 10.64ns, 2.74ns and 0.71ns respectively for $a_B = 20$nm quantum dot and 42.07ns, 6.86ns and 1.12ns respectively for $a_B = 50$nm quantum dot. Thus we notice that the decoherence process is faster in low dimensional spin–bath system. This is because of the quantum confinement effects, as can be directly verified from the expressions for $J(\vec{r})$ in each cases. In Fig. 6.2, we plot the decoherence curves for $P_y(0) = 1$ and $P_x(0) = P_z(0) = 0$. Here, for all values of u, we

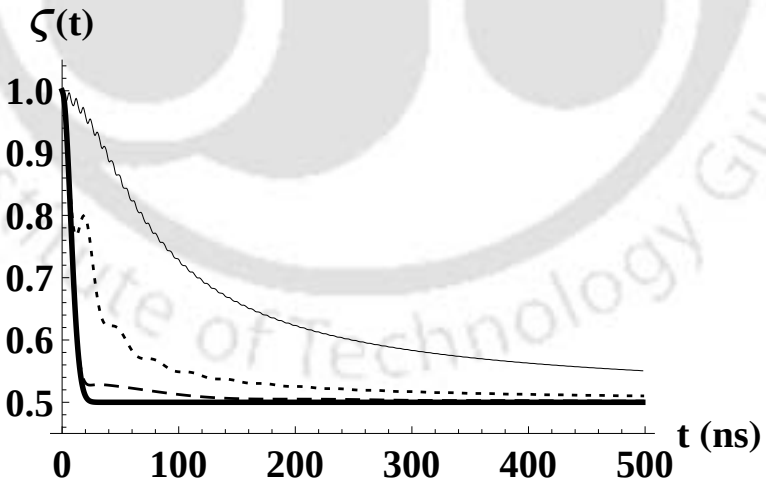

Figure 6.2: The time development of decoherence when $|\psi_S(0)\rangle = \frac{1}{\sqrt{2}}(|0\rangle + i\,|1\rangle)$. The continuous–thick, dashed, dotted and continuous–thin curves corresponds to $u = 0$, $u = 0.2$, $u = 1$ and $u = 5$ respectively.

notice complete decoherence, as the initial state is neither an eigen state of the

system–Hamiltonian, nor of the interaction term. For $u = 0$, we obtain the same expression as in Eq. (6.25) for decoherence factor, but for all other values of u, the dynamics is slower than square-exponential decay. The characteristic time τ_D monotonically increases with the value of u. The decoherence process is still different from both of the above cases when $P_z(0) = 1$ and $P_x(0) = P_y(0) = 0$ as can be seen from Fig. 6.3. In this case, $\varsigma(t)$ does not decay at all when $u = 0$,

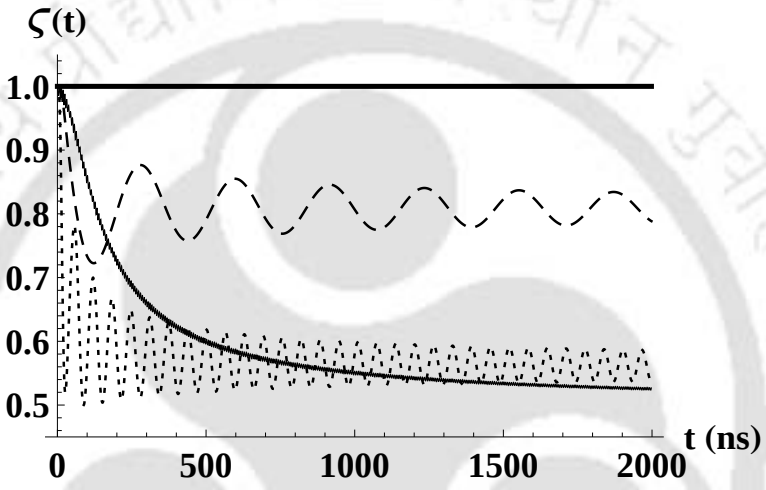

Figure 6.3: The time development of decoherence when $|\psi_S(0)\rangle = |0\rangle$. The continuous–thick, dashed, dotted and continuous–thin curves corresponds to $u = 0$, $u = 0.2$, $u = 1$ and $u = 10$ respectively.

as can be seen from Eq. (6.24), where it can be evaluated to get $P_z(t) = 1$ and $P_x(t) = P_y(t) = 0$ at all times. This is because our present initial state is an eigen state of the interaction–Hamiltonian, which is the only term that governs the evolution of the system when $u = 0$. But for all other values of u, the state decoheres. But the steady state value to which it approaches is determined by the relative strengths of system and interaction Hamiltonian terms. In the limit of very large values for u, we notice complete decoherence. But the characteristic time for complete decoherence in such cases was found to be very large. For example, τ_D can be graphically determined from Fig. 6.3 to be around 250ns when $u = 10$. For medium values of u, we notice partial decoherence accompanied by oscillations in the process. The value of steady–state $\varsigma(t)$ decreases with the increase in u values.

6.4 Conclusion

We have used a simplistic model due to F. M. Cucchietti et al. to study the decoherence dynamics of the various spin states of a single electron sitting inside a quantum dot. We considered a $Ga_{1-x}Al_xAs$ quantum dot with a single component (z-z) hyperfine interaction where each nuclear spin is assumed to carry equal but average $g_N \frac{\hat{I}_z}{\hbar\hat{\sigma}_z}$ values, and the interaction strength with electron was expressed as a function of position vector. Thus we could evaluate a realistic value for the statistical spread of the total energy variable for the entire nuclear bath. We have assumed a completely uncorrelated spin bath. We performed the analysis for three different geometries of the spin bath and evaluated the dependence of energy spread on bath dimension. We obtained large spread for lower dimension as the magnitude of wavefunction and thereby the interaction strength increases for lower dimensional structures. This is purely a quantum confinement effect. We used the trace of the square of reduced density matrix as a parameter to quantitatively study the decoherence effects. We noticed that when the initial state was not an eigen state of the system or the interaction Hamiltonian, the state decohered completely. But for all other cases, we observed partial decoherence. The degree of decoherence is found to depend on the relative magnitude of system and interaction terms. When the initial state corresponds to that part of the Hamiltonian which was relatively strong, lesser decoherence was observed for the state. Thus the decoherence process depends on the initial state of the system as well as the relative strengths of different terms in the Hamiltonian. A recent experiment [138] gives phase decoherence time as high as $500\mu s$ in quantum dots, which is way above the values we obtained here for open quantum systems with very weak system–Hamiltonian term. But such large decoherence times can still be attributed to strong system Hamiltonian term with initial state as an eigen state of the interaction term, as can be noticed from Fig. 6.3. But more importantly, this discrepancy may be better attributed to the too simplistic model we have considered, where only a one component spin–spin interactions is taken into account for the analysis.

Chapter 7

Decoherence of two-electron spin qubits

7.1 Introduction

Electrons confined in coupled quantum dots are promising candidates for scalable spin qubits [38]. In order to perform useful quantum gate operations, the coherence of the spin phase must be maintained for sufficiently long periods of time. The main physical mechanisms that limit the coherence time of spin qubits are spin-orbit interactions and interaction with nuclear-spins. The effect of spin-orbit interaction on spin decoherence via the interaction through phonons is expected to be minimum in quantum dots (QDs) at low temperatures [147]. In contrast, the contact hyperfine interaction between the electron spin and a random nuclear spin environment is reported to play an important role in deciding the spin dephasing time T_2^* in QDs made out of GaAs material [43]. This interaction is proportional to the modulus square of the electron wavefunction at the location of each nucleus and thus it leads to a position dependent coupling strength within the QD. In the last two decades, there has been much effort to theoretically describe the decoherence of spin phase of localized electrons due to hyperfine interactions. Some authors have employed a semi-classical model for the interaction between the electron and nuclear spins, in which the time-dependent Overhauser fields induced by the nuclear spins are treated as classical vector variables [133],

whereas others have aimed at fully quantum mechanical solution for the spin dynamics, where the problem is solved in a subspace where the total z-component of the spin takes specific values [134; 148]. Using analytical and numerical tools, the problem has also been studied in the presence of an external magnetic field with various initial bath polarizations [149].

As the final problem in this thesis, we study the decoherence of two electron spin qubits in a coupled quantum dot due to their interaction with the surrounding nuclear spin bath. We utilize an extended version of the simplified model discussed in the previous chapter on single electron decoherence. The theoretical framework for this study is discussed in Section 7.2. Following this, the results for various initial two-qubits are presented in Section 7.3. Finally the chapter is concluded in Section 7.4.

7.2 Theory

A system of two electrons in a nuclear spin bath may be modeled by the following Hamiltonian

$$\hat{H} = J_{ex}\hat{\vec{\sigma_A}} \cdot \hat{\vec{\sigma_B}} + \hat{\sigma}_A^z \otimes \left(\sum_{k=1}^{N} g_A^k \hat{\sigma}_k^z\right) + \hat{\sigma}_B^z \otimes \left(\sum_{k=1}^{N} g_B^k \hat{\sigma}_k^z\right) \tag{7.1}$$

where the first term corresponds to the exchange interaction between the spin qubits A and B, and the latter two terms correspond to the interaction of individual spins with the surrounding nuclear bath. $g_{A/B}^k$ is the interaction strength between qubit $A(B)$ with the k^{th} nuclear spin and $\hat{\sigma}_{A/B/k}^i$ are the standard Pauli matrices (with $i = x, y, z$) for the electrons and nuclear spins. It may be noticed that the hyperfine interaction between the electron spins and the nuclear bath is taken to be of Ising type (has only one component), whereas the interaction between the two electrons is of Heisenberg type (with all the three components). This will keep the model simple enough to be analytically tractable. Though this is not a very accurate description for hyperfine interaction, we believe that it can capture the essential features of the relevant interactions and thus it can give valuable results when applied to various systems.

Since the state of a spin-$\frac{1}{2}$ particle is a vector in two-dimensional Hilbert space, one usually expresses them in the basis of $|\uparrow\rangle$ (up) and $|\downarrow\rangle$ (down) states, namely, the eigen vectors of the σ^z operator. In a similar way, we express a generic state of the nuclear spin bath containing N spin-$\frac{1}{2}$ nuclei, in a 2^N dimensional basis of product states, $|\uparrow\uparrow\ldots\uparrow\uparrow\rangle$, $|\uparrow\uparrow\ldots\uparrow\downarrow\rangle$, $\cdots\cdots|\downarrow\downarrow\ldots\downarrow\downarrow\rangle$. Labeling each product state with integers ranging from 0 to 2^N-1, we write the generic state of nuclear spin bath at time t as

$$|\psi_E(t)\rangle = \sum_{k=0}^{2^N-1} c_n(t)\,|n\rangle\,. \tag{7.2}$$

where the subscript E stands for the environment and c_n's are the probability amplitudes for different product states and, at $t=0$, we assume $c_n(0) = 1/\sqrt{2^N}$ for all n. In other words, we consider a completely depolarized initial state for the spin bath, where each nuclear spin individually has equal probability for being in the up or down state. We further assume that the total state $|\psi_T\rangle$ is a product of the two-qubit system state $|\psi_{AB}\rangle$ and the environmental state $|\psi_E\rangle$ at $t=0$, given by

$$|\psi_T(0)\rangle = |\psi_{AB}(0)\rangle\,\frac{1}{\sqrt{2^N}}\sum_{k=0}^{2^N-1}|n\rangle \tag{7.3}$$

Beginning with this initial state, the system and environment will get entangled with the progression of time. This is governed by the combined time evolution of the system and environment by the total Hamiltonian (Eq. 7.1) that can be written as

$$|\psi_T(t)\rangle = e^{i\hat{H}t/\hbar}\,|\psi_T(0)\rangle = \frac{1}{\sqrt{2^N}}\sum_{n=0}^{2^N-1}\hat{U}_n(t)\,|\psi_{AB}(0)\rangle\,|n\rangle \tag{7.4}$$

where

$$\hat{U}_n(t) = e^{-\frac{i}{\hbar}\left(J_{ex}\hat{\vec{\sigma}}_A\cdot\hat{\vec{\sigma}}_B+\epsilon^n_A\hat{\sigma}^z_A+\epsilon^n_B\hat{\sigma}^z_B\right)t} \tag{7.5}$$

$$\epsilon^n_{A/B} = \sum_{k=1}^{N}(-1)^{n_k}g^k_{A/B}. \tag{7.6}$$

Here $n_k = 0(1)$ if the k^{th} nuclear spin has an up (down) configuration in the n^{th}

product state. Since our aim is to find the state of the two qubit system at a later time t, we employ the density matrix formalism which has the advantage of taking into account of the mixed states (classical probabilities) in addition to the pure states (probability amplitudes). The density matrix for the total state at any time t is given by $\rho_T(t) = |\psi_T(t)\rangle \langle\psi_T(t)|$. The two-qubit density matrix at time t is obtained from the total density matrix by performing a partial trace operation over all the bath degrees of freedom. Thus

$$\rho_{AB}(t) = \mathrm{Tr}_E \rho_T(t) = \frac{1}{2^N} \sum_{n=0}^{2^N-1} \hat{U}_n(t) \rho_{AB}(0) \hat{U}_n^\dagger(t) \tag{7.7}$$

where $\rho_{AB}(0) = |\psi_{AB}(0)\rangle \langle\psi_{AB}(0)|$. The degree of mixedness in the state $\rho_{AB}(t)$ depends on the degree of entanglement between the system and the environment in the total state $|\psi_T(t)\rangle$.

7.2.1 Characteristics of two-qubit density matrices

Any two-qubit density matrix is a 4×4 matrix having 16 unique elements. It is a standard procedure to synthesize such a matrix in terms of 15 polarization coefficients as written below.

$$\rho_{AB}(t) = \frac{1}{4} \left[I + \vec{P}_A(t) \cdot \vec{\sigma}_A + \vec{P}_B(t) \cdot \vec{\sigma}_B + \sum_{u,v=x,y,z} \Pi^{uv}(t) \sigma_A^u \sigma_B^v \right]. \tag{7.8}$$

Here, $\vec{P}_{A/B}$ =Tr$[\rho_{AB} \vec{\sigma}_{A/B}]$ is the polarization vector for qubit A/B and it has 3 components. Π^{uv} =Tr$[\rho_{AB} \sigma_A^u \sigma_B^v]$ is a 3×3 matrix containing 9 components corresponding to various tensor polarizations. For example, in the case of singlet state ($\frac{|\uparrow\downarrow\rangle - |\downarrow\uparrow\rangle}{\sqrt{2}}$), the non-zero polarization components are $\Pi^{xx} = \Pi^{yy} = \Pi^{zz} = -1$. Likewise, for the triplet state ($\frac{|\uparrow\downarrow\rangle + |\downarrow\uparrow\rangle}{\sqrt{2}}$), the non-zero polarization components are $\Pi^{xx} = \Pi^{yy} = 1$ and $\Pi^{zz} = -1$. Similarly, for the product state ($|\uparrow\downarrow\rangle$), all polarization components are zero except $P_A^z = 1, P_B^z = \Pi^{zz} = -1$.

From the two-qubit density matrix, one can evaluate quantitative measures such as $\varsigma(t)$ =Tr$\rho_{AB}^2(t)$ and concurrence. If the elements of the matrix are functions of time, the polarization components as well as the quantitative measures

will also vary with time. The plot of $\varsigma(t)$ with respect to time can tell us how the quantum coherence of the two-qubit state is lost as a function of time. This, in terms of polarization components, can be written as

$$\varsigma(t) = \frac{1}{4}\left[1 + \sum_{j=x,y,z}\left(P_A^j(t)^2 + P_B^j(t)^2\right) + \sum_{u,v=x,y,z}\Pi^{uv}(t)^2\right]. \tag{7.9}$$

The value of concurrence $C(\rho_{AB}(t))$ gives us a measure of entanglement between qubits A and B at any given time t [150]. It is defined, for a two-qubit density matrix, as

$$C(\rho_{AB}) = \text{Max}(0, \lambda_1 - \lambda_2 - \lambda_3 - \lambda_4) \tag{7.10}$$

where $\lambda_1, \lambda_2, \lambda_3$, and λ_4 are the eigen values (in decreasing order) of the matrix

$$R = \sqrt{\sqrt{\rho_{AB}}\left(\sigma_A^y\sigma_B^y\rho_{AB}^*\sigma_A^y\sigma_B^y\right)\sqrt{\rho_{AB}}}.$$

7.2.2 Continuum Limit

For coupled quantum dots considered in chapter 5, the value of N is of the order of 10^5 and thus 2^N is a very large number ($10^{30,000}$). Therefore, we can approximate the qubit-bath interaction strength, $g_{A/B}^k$ in Eq. 7.5, as a smooth function of position that depends on the single electron probability densities of the corresponding electrons, as

$$g_{A/B}(\vec{r}) = \kappa\left|\psi_{A/B}(\vec{r})\right|^2 \tag{7.11}$$

where $\kappa = \frac{2}{3\hbar^2}\mu_0 g_e g_N \mu_B \mu_N \eta$, with g_e and g_N the electron and nuclear g-factors, μ_B and μ_N are the Bohr and nuclear magnetons, η is the square of Bloch wave amplitude, and $\psi_{A/B}(\vec{r})$ is the amplitude of electron envelope function. The value of κ after the substitution of various parameters turns out to be $1.62\,\mu\text{eV}\,\text{nm}^3$ as shown in Appendix A. In a Hibert space containing only the lowest singlet and triplet states, the single electron probability densities for a general state in Eq.

(5.5) can be written as

$$\begin{aligned}\left|\psi_{A/B}(\vec{r},t)\right|^2 = &\frac{1-S^2\left(C_1^2-C_2^2\right)}{2\left(1-S^4\right)}\left(\left|\varphi_L(\vec{r})\right|^2+\left|\varphi_R(\vec{r})\right|^2\right)\\ &+S\frac{\left(C_1^2-C_2^2\right)-S^2}{2\left(1-S^4\right)}\left(\varphi_L^*(\vec{r})\varphi_R(\vec{r})+\varphi_R^*(\vec{r})\varphi_L(\vec{r})\right)\\ &\pm\frac{C_1C_2}{\sqrt{1-S^4}}\left(\left|\varphi_L(\vec{r})\right|^2-\left|\varphi_R(\vec{r})\right|^2\right)\cos\left(J_{ex}t/\hbar\right)\\ \pm iS&\frac{C_1C_2}{\sqrt{1-S^4}}\left(\varphi_L^*(\vec{r})\varphi_R(\vec{r})-\varphi_R^*(\vec{r})\varphi_L(\vec{r})\right)\sin\left(J_{ex}t/\hbar\right)\end{aligned} \tag{7.12}$$

where we have assumed the initial superposition amplitudes, C_1 and C_2, to be real numbers. When $S \leq 0.1$ (weak coupling limit), the second and fourth terms in the above equation can be neglected and the simplified expression becomes

$$\left|\psi_{A/B}(\vec{r},t)\right|^2 = \frac{1}{2}\left(\left|\varphi_L(\vec{r})\right|^2+\left|\varphi_R(\vec{r})\right|^2\right)\pm C_1C_2\left(\left|\varphi_L(\vec{r})\right|^2-\left|\varphi_R(\vec{r})\right|^2\right)\cos\left(J_{ex}t/\hbar\right). \tag{7.13}$$

Since $|\varphi_L(x,y)|^2 = |\varphi_0(x-a,y)|^2$ and $|\varphi_R(x,y)|^2 = |\varphi_0(x+a,y)|^2$, it is easy to verify from above equation that

$$|\psi_A(x,y,t)|^2 = |\psi_B(-x,y,t)|^2. \tag{7.14}$$

at all times. That is, for every nuclear spin at (x,y) which interacts with electron A by a particular interaction strength, there exists another nucleus at $(-x,y)$ which interacts with electron B by the same interaction strength. Therefore, if we assume that all individual nuclei in the nuclear bath possesses the same statistics, then the qubit-bath interaction energies, $\epsilon_A = \int(\pm g_A(\vec{r}))\,dV$ and $\epsilon_B = \int(\pm g_B(\vec{r}))\,dV$ will both have the same statistics. Here the integrals are over the entire volume of the spin bath. This is a consequence of central limit theorem (CLT) which we have discussed in section 6.2.

From Eq. 7.13, it is clear that for singlet ($C_2 = 0$) and triplet ($C_1 = 0$) states, the time dependent term goes to zero and both electrons (A and B) have the same probability density functions distributed over the coupled dots. In such cases the qubit-bath interaction energies are totally correlated, that is, we can define $\epsilon_A = \epsilon_B = \epsilon$. The statistics of ϵ is given by a Gaussian probability density

function given in 6.12 whose mean is zero (as each individual nucleus is assumed to have a mean equal to zero) and standard deviation Λ given by

$$\Lambda_{A/B}^2 = \int g_{A/B}^2(\vec{r}) \frac{dV}{d^3} \tag{7.15}$$

where d is the inter-nuclear distance.

For the superposed singlet and triplet initial states, $|\psi_A(t)|^2$ and $|\psi_B(t)|^2$ oscillate alternately between the left and right QDs. Larger the value of J_{ex}, larger will be the frequency with which $\left|\psi_{A/B}(t)\right|^2$ will oscillate. At times when $J_{ex}t/\hbar$ is an odd multiple of $\pi/2$, single electron probabilities for both electrons will become the same and ϵ_A and ϵ_B are again fully correlated. On the other hand, when $J_{ex}t/\hbar$ is an even multiple of $\pi/2$, they are minimally correlated. Thus we have a time-dependent correlation between the variables ϵ_A and ϵ_B which can be represented by a joint probability density function, $f(\epsilon_A, \epsilon_B, t)$. When $C_1 = C_2 = 1/\sqrt{2}$ and $J_{ex} = 0$, the single electron probabilities will be such that electron A will continue to sit in the left QD while electron B on the right QD and thus the joint probability density function will be time-independent. Since the regions of bath where electron A and electron B have non-zero interactions are almost mutually exclusive in the present case, we can treat the two electrons as if they are interacting with separate baths. Thus we write

$$f(\epsilon_A, \epsilon_B) = \frac{1}{2\pi\Lambda^2} e^{-\frac{\epsilon_A^2+\epsilon_B^2}{2\Lambda^2}}, \tag{7.16}$$

as the product of two Gaussians in variable ϵ_A and ϵ_B respectively with equal means and standard deviations.

Now, we can express the summation over n in Eq. 7.7 with an integration over ϵ_A and ϵ_B, the qubit-bath interaction energy variables for electron A and electron B. The limits of integration go from $\epsilon_{\min} = -\int g_A(\vec{r})dV$ to $\epsilon_{\max} = \int g_A(\vec{r})dV$. Thus, the polarization components of the two-qubit density matrix at time t

become

$$P^j_{A/B}(t) = \int\int_{\epsilon_{\min}}^{\epsilon_{\max}} \mathrm{Tr}[\hat{U}(\epsilon_A,\epsilon_B,t)\rho_{AB}(0)\hat{U}^\dagger(\epsilon_A,\epsilon_B,t)\sigma^j_{A/B}]f(\epsilon_A,\epsilon_B,t)d\epsilon_A d\epsilon_B$$
$$\Pi^{uv}(t) = \int\int_{\epsilon_{\min}}^{\epsilon_{\max}} \mathrm{Tr}[\hat{U}(\epsilon_A,\epsilon_B,t)\rho_{AB}(0)\hat{U}^\dagger(\epsilon_A,\epsilon_B,t)\sigma^u_A\sigma^v_B]f(\epsilon_A,\epsilon_B,t)d\epsilon_A d\epsilon_B. \tag{7.17}$$

where $2^N f(\epsilon_A,\epsilon_B,t)d\epsilon_A d\epsilon_B$ is the number of bath product states having first qubit-bath ineraction energy between ϵ_A and $\epsilon_A + d\epsilon_A$ and the second qubit-bath interaction energy between ϵ_B and $\epsilon_B + d\epsilon_B$.

7.3 Results and Discussion

The single electron probability density function for singlet and triplet states of a coupled cylindrical quantum dots discussed in chapter 5 is shown in Fig. 7.1. The

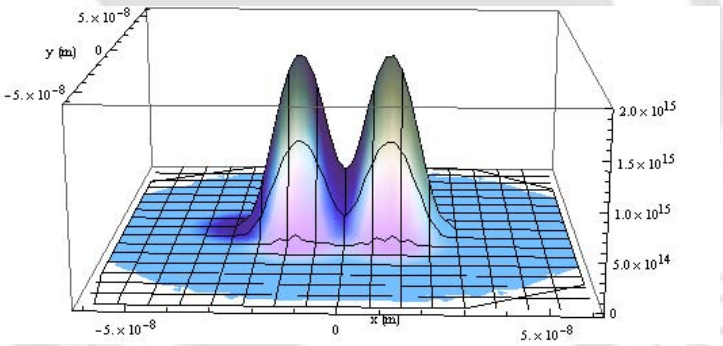

Figure 7.1: Single electron probability density function ($|\psi_A(t)|^2 = |\psi_B(t)|^2$) for completely correlated qubit-bath interaction energy variables ϵ_A and ϵ_B.

single dot diameter here is 15nm and the centers of the two dots are separated by 24nm. Since $\epsilon_A = \epsilon_B = \epsilon$, we have $f(\epsilon_A,\epsilon_B,t) = \frac{1}{\sqrt{2\pi}\Lambda}e^{\frac{\epsilon^2}{2\Lambda^2}}$ in this case, and the integration is performed over a single variable ϵ. The value of Λ is obtained using Eq. 7.15 as 1.98×10^{-4}meV. For singlet and triplet states, the expression for $\hat{U}(\epsilon,t)$ becomes

$$\hat{U}(\epsilon,t) = e^{-\frac{i}{\hbar}\left(J_{ex}\hat{\vec{\sigma}}_A\cdot\hat{\vec{\sigma}}_B + \epsilon(\hat{\sigma}^z_A+\hat{\sigma}^z_B)\right)t}. \tag{7.18}$$

$\hat{U}(\epsilon,t)$ operating on an initial singlet ($\frac{|\uparrow\downarrow\rangle - |\downarrow\uparrow\rangle}{\sqrt{2}}$) or triplet states ($\frac{|\uparrow\downarrow\rangle + |\downarrow\uparrow\rangle}{\sqrt{2}}, |\uparrow\uparrow\rangle, |\downarrow\downarrow\rangle$)

will introduce only a phase which will get canceled when multiplied with $\hat{U}^{\dagger}(\epsilon, t)$. Thus the integrals in Eq. 7.17 become very trivial as the trace part is independent of ϵ. The polarization components at time t turnout to be the same as the ones at $t = 0$. This means that these states will neither decohere nor lose their initial entanglement with the progress of time.

For superposed singlet and triplet states, we consider two values of exchange interaction coefficients: (i) $J_{ex} = 0.5$ and (ii) $J_{ex} = 0$. In the first case the single electron probabilities for electron A and B oscillate fast between the two dots. The period of oscillation is $2\pi\hbar/J_{ex} \approx 8$ps. Thus to simplify the analysis, we can average out the fast time dependent part. This results in $|\psi_A(t)|^2 = |\psi_B(t)|^2$ leading to $\epsilon_A = \epsilon_B = \epsilon$. For $C_1 = C_2 = 1/\sqrt{2}$, the density matrices at time $t = 0$ and at a later time t can be written as

$$\rho_{AB}(0) = \begin{bmatrix} 0 & 0 & 0 & 0 \\ 0 & 1 & 0 & 0 \\ 0 & 0 & 0 & 0 \\ 0 & 0 & 0 & 0 \end{bmatrix}; \tag{7.19}$$

$$\rho_{AB}(t) = \begin{bmatrix} 0 & 0 & 0 & 0 \\ 0 & \cos^2(2J_{ex}t/\hbar) & \frac{i}{2}\sin(4J_{ex}t/\hbar) & 0 \\ 0 & -\frac{i}{2}\sin(4J_{ex}t/\hbar) & \sin^2(2J_{ex}t/\hbar) & 0 \\ 0 & 0 & 0 & 0 \end{bmatrix}. \tag{7.20}$$

Since $\rho_{AB}^2(t) = \rho_{AB}(t)$ in this case, the density matrix corresponds to a pure state indicating no decoherence with time. We plot the measure of entanglement between qubit A and B as a function of time as shown in Fig. 7.2. As the initial state is a product state, there is no entanglement at $t = 0$. But as time progresses, the qubits are entangled and disentangled in a periodic way. The frequency of this dynamics is about 8 times the frequency with which $\left|\psi_{A/B}(t)\right|^2$ oscillates. When $J_{ex} = 0$, the qubit-bath interaction energies ϵ_A and ϵ_B can be considered to be independent of each other. The single electron probability density for qubit A and B in such a case are shown in Fig. 7.3. The expression for $U(\epsilon_A, \epsilon_B, t)$ becomes

$$\hat{U}(\epsilon_A, \epsilon_B, t) = e^{-\frac{i}{\hbar}\left(\epsilon_A\hat{\sigma}_A^z + \epsilon_B\hat{\sigma}_B^z\right)t}. \tag{7.21}$$

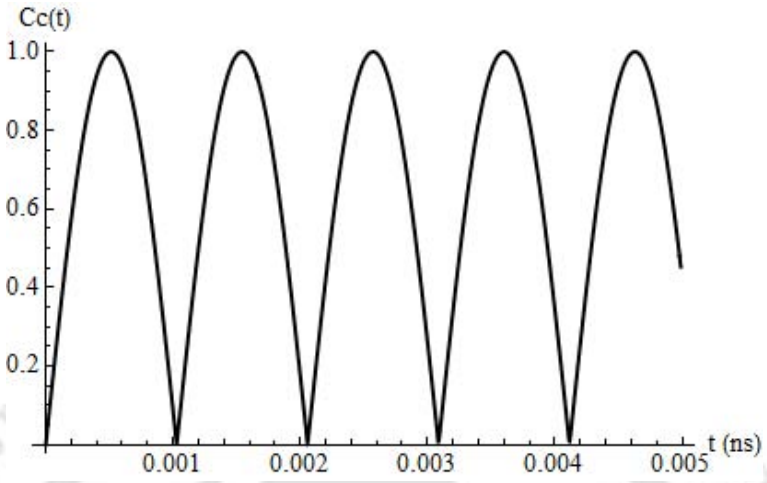

Figure 7.2: Concurrence as a function of time when $J_{ex} = 0.5$ and the initial state is $|\uparrow\downarrow\rangle$.

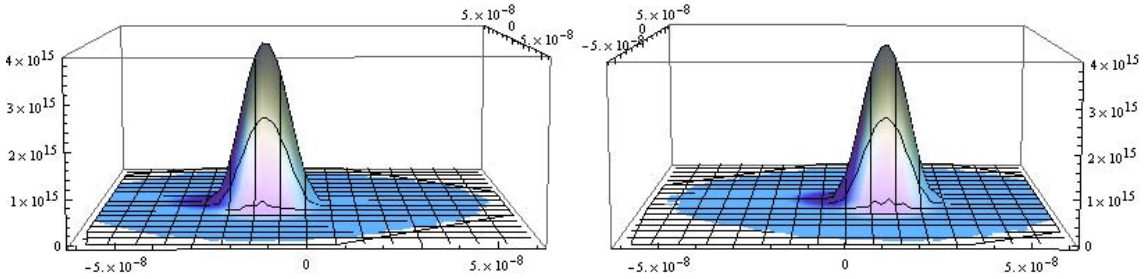

Figure 7.3: Single electron probability density functions $|\psi_A(t)|^2$ and $|\psi_B(t)|^2$ when $J_{ex} = 0$.

As in the case of singlet and triplet states, this operator will only introduce a global phase to the initial state and, therefore, the density matrix will remain the same for all times. Thus the initial state $|\uparrow\downarrow\rangle$ will neither decohere nor develop entanglement with time.

Finally we consider the decoherence property of a very important initial state, the Bell state, $|\psi_{AB}\rangle = \frac{|\uparrow\uparrow\rangle \pm |\downarrow\downarrow\rangle}{\sqrt{2}}$. Since this is a linear combination two triplet states, we only have one qubit-bath interaction energy variable, ϵ. The form of

density matrix ρ_{AB} at a later time t can be written as

$$\rho_{AB}(t) = \frac{1}{\sqrt{2\pi}\Lambda}\int_{\epsilon_{min}}^{\epsilon_{max}} \tilde{\rho}_{AB}(\epsilon,t)e^{-\frac{\epsilon^2}{2\Lambda}}d\epsilon \tag{7.22}$$

where

$$\tilde{\rho}_{AB}(\epsilon,t) = \begin{bmatrix} \frac{1}{2} & 0 & 0 & \frac{1}{2}e^{-i4\epsilon t/\hbar} \\ 0 & 0 & 0 & 0 \\ 0 & 0 & 0 & 0 \\ \frac{1}{2}e^{i4\epsilon t/\hbar} & 0 & 0 & \frac{1}{2} \end{bmatrix}. \tag{7.23}$$

The above integration can be performed with limits from $-\infty$ to ∞ for each element of $\rho_{AB}(t)$ separately and it will modify only the ϵ dependent element in the matrix as shown below.

$$\frac{1}{2\sqrt{2\pi}\Lambda}\int_{-\infty}^{\infty} e^{\pm\frac{i4\epsilon t}{\hbar}}e^{-\frac{\epsilon^2}{2\Lambda}}d\epsilon = \frac{1}{2}e^{-\frac{8\Lambda^2t^2}{\hbar^2}} \tag{7.24}$$

The measure for decoherence becomes

$$\mathrm{Tr}\rho_{AB}^2(t) = \frac{1}{2}\left(1+e^{-\left(\frac{4\Lambda}{\hbar}\right)^2t^2}\right).$$

This is plotted in Fig. 7.4. From this plot, a characteristic time for decoherence may be evaluated as $\frac{\hbar}{4\Lambda}$. The measure of entanglement, concurrence, is also plotted for the present $\rho_{AB}(t)$ matrix in Fig.7.5. From these graphs, it is clear that both the coherence and the degree of entanglement of the two qubit state are totally lost in a time scale of 1 ns.

Decoherence also depends on the degree of confinement due the QDs. This is because, the value of Λ, the standard deviation of the qubit-bath interaction energy distribution function, depends on the spread of the wavefunction. As the confinement increases, electrons interact with the surrounding nuclear-bath with an increased strength of qubit-bath interaction giving rise to larger values of Λ. Such behavior was also noticed in the case of single qubit decoherence.

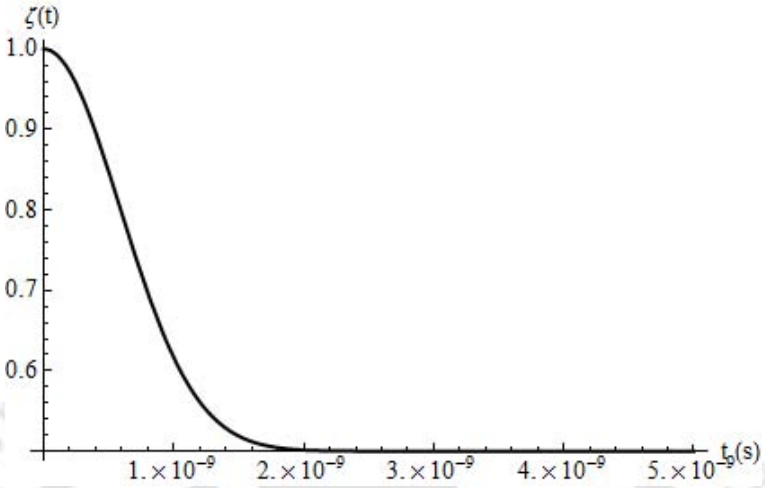

Figure 7.4: Tr$\rho_{AB}(t)$ as a function of time when the initial state is $\frac{|\uparrow\uparrow\rangle \pm |\downarrow\downarrow\rangle}{\sqrt{2}}$.

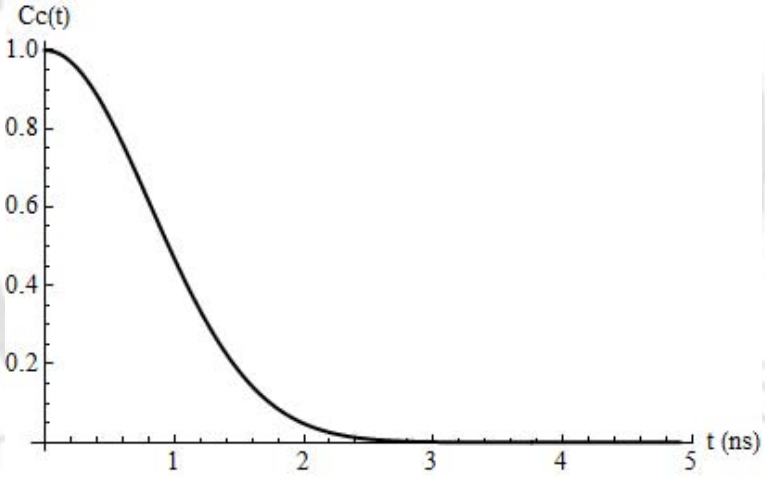

Figure 7.5: Concurrence as a function of time when the initial state is $\frac{|\uparrow\uparrow\rangle \pm |\downarrow\downarrow\rangle}{\sqrt{2}}$.

7.4 Conclusion

In this chapter, we considered an Ising type model of hyperfine interaction between two electrons in a coupled quantum dots and the surrounding nuclear bath. All nuclei in the bath were assumed to have an equally likely probability of being in the up or down state. Therefore, we could apply the central limit theorem and obtain a simplified representation of the problem in the composite qubit-bath interaction energy variables ϵ_A and ϵ_B. These energies depend not only on the

state of the spin-bath, but also on the single electron probabilities of qubit A and B. Therefore, whenever these probabilities are one and the same, we have a totally correlated interaction with the bath for both electrons. On the other hand, when these probabilities are functions having no or very little overlap, the interaction energy variables are independent of each other. In the first case, we defined an energy density function in one variable and in the second case, we defined a joint-energy density function. We then used these approximations to study the decoherence and entanglement dynamics of various initial two-qubit states. It was noticed that the singlet and triplet states did not decohere or lose entanglement with respect to time. This is because these states turn out to be the eigen states of the two qubit operator $\hat{U}(\epsilon, t)$. We also considered superposition of singlet and triplet states in the limits of very small and very large magnitude of J_{ex}. When it is large, we could overlook the fast coherent oscillations and took only the static part of the single electron probability densities. This resulted in no decoherence of the two-qubit states and periodic oscillations in entanglement measure. When J_{ex} is very small, we considered ϵ_A and ϵ_B as two independent variables and we observed no decoherence with time. Finally we considered Bell states that are superposition of $|\uparrow\uparrow\rangle$ and $|\downarrow\downarrow\rangle$ triplet states. In this case we observed decay of coherence as well as the measure of initial entanglement. We could estimate a decoherence time which only depended on the standard deviation of the interaction energy distribution. Thus, we observed that only initial states that are not eigen states of the interaction Hamiltonian decohere with respect to time. All eigen states of the interaction Hamiltonian will continue to evolve coherently with respect to time.

Chapter 8

Conclusions

The works presented in this thesis are in view of the second quantum revolution [72], i.e. the revolution of engineering quantum mechanics to build technologies such as quantum computers. Our study focused mainly on the properties of single electron and two electron semiconductor quantum dots (QDs). In the literature, the theoretical studies on quantum dots are mostly based on harmonic oscillator confinement potentials. They are a good model potential for QDs made out of patterned gate electrodes, which have the advantage of electrical manipulation of their properties. This convenience is what lies at the heart of Loss-DiVincezo proposal for quantum computation. On the other hand, for QDs that are grown in a self-assembled way, spectroscopic studies suggest that smooth models for confinement potential may not be a proper approximation. Therefore, in Chapter 2, we considered a QD with cylindrical geometry in which the confining potential in the radial direction was taken to be a step potential of finite size. The time independent Schrodinger equation was solved analytically with different effective masses for regions inside and outside the step potential. The eigen values were determined numerically in order to satisfy the continuity of wavefunction at the QD boundary. We also plotted the variation of energy levels with the flux density of the applied magnetic field. We observed that the effect of diamagnetism dominated at higher magnitudes of magnetic flux densities. This resulted in significant compression of energy eigen states, especially for large QD radius.

In Chapter 3, we studied the effect of magnetic flux densities on an electron bound to a hydrogenic donor impurity inside a quasi two-dimensional semiconduc-

tor host material. The binding potential was approximated by a two-dimensional $1/r$ potential. Since there existed no analytical solution for the time independent Schrodinger equation of this problem, numerical methods were employed. It was found that the numerical methods based on linear grid gave incorrect solution near the singularity point. The validation of the numerical results was done using the case of zero magnetic field, for which exact analytical solutions exist. Thus we employed Numerov's shooting method based on logarithmic grid to increase the sampling rate near the singularity point and noticed excellent accuracy near the singularity point. The variation of energy levels with magnetic flux densities was plotted for different values of radial and azimuthal quantum numbers. It was noticed that the dependency of energy levels on magnetic field is significant only when the characteristic spread of wavefunction becomes comparable to the cyclotron radius. Therefore, the ground state was least affected as its effective Bohr radius is much smaller in comparison to that of the excited states.

In Chapter 4, we studied the problem of two electrons in a single cylindrical quantum dot in the presence of a magnetic field. We employed linear variational analysis to solve the time independent Schrodinger equation, where the trial wavefunction was constructed out of Fock-Darwin states. The strength of the oscillator potential was fixed by tuning the oscillator frequency for minimum ground state energy. We plotted the two-electron energy spectrum as a function of external magnetic field strength for various values of z-component of the total angular momentum and total spin quantum numbers. The results showed an oscillation in ground state between singlet and triplet with the increase in magnetic flux density. From the energy spectrum, we evaluated the free energy and then determined the dependency of magnetization with respect to the magnetic field strength. Similarly, we also plotted radial electron density and pair correlation functions for different quantum numbers and different magnetic field strengths. The results we obtained are in complete agreement with the results due to finite difference methods reported in the literature.

In Chapter 5, we studied the properties of exchange interaction between two electrons confined in a coupled quantum dot system. Firstly, we considered two heterostructured (cylindrical) QDs laterally coupled to each other and then two hydrogenic donor impurities laterally coupled to each other. We approximated

the system to be two-dimensional and solved the Schrodinger equation under the effective mass approximation. Assuming very low probability for the system to be in the excited states, we evaluated the exchange interaction coefficient using Heitler-London and Weinbaum's approximations of molecular physics. It was observed that the Weibaum method significantly improves the calculation of exchange energy for the heterostructured case over the Heitler-London method, whereas, for the impurity based coupled QDs, Weinbaum's method did not give any significant improvement. We plotted the dependency of exchange interaction with respect to magnetic field for various inter-dot separations. Compared to the patterned gate based switching of exchange interaction, in our system we do not have any control over the inter-dot separation d. The value of d is fixed in both cases of the coupled QDs we analyzed. Nevertheless the exchange interaction can be controlled/switched using the external magnetic field strength as a handle. To completely switch off the exchange interaction, it was noticed that we must apply very high magnetic fields where the contribution from Zeeman interactions becomes significant. Therefore, the splitting of triplet states must also be taken into account for proper evaluation of exchange interaction coefficient.

In the final part of the thesis we studied the decoherence of spin qubits in quantum dots due to its hyperfine interaction with the surrounding nuclear bath environment. In Chapter 6, we considered the decoherence of a central spin using a simplistic model that takes into account only of the σ_z-σ_z interaction. The strength of interaction between the electron and nuclei was expressed as a function of position vector as the contact hyperfine interaction term depends on the modulus square of the envelope wavefunction. We assumed a completely uncorrelated nuclear spin distribution inside the bath and applied central limit theorem to express the problem in terms of composite qubit-bath interaction energy variable. We then showed how the spread of interaction energy depended on the confinement of electron inside the QD geometry. This in turn can be related to the rate of decoherence. Using the trace of the square of reduced density matrix, we estimated the time scale in which the initial state decoheres. We noticed that when the initial state was not an eigen state of the system or interaction Hamiltonian, the state decohered completely. But for all other cases, we observed only partial decoherence. The degree of decoherence depended on

the relative magnitude of system and interaction terms. When the initial state was an eigen state of the stronger part of the Hamiltonian, lesser decoherence was observed for the state. Thus the decoherence process depends on the initial state of the system as well as the relative strengths of different terms in the Hamiltonian.

In Chapter 7, we extended the above open quantum system model to the case of coupled QDs. Since there are now two electrons, the exchange interaction between them must also be taken into account. Since each electron interacts with the nuclear bath surrounding it, we defined two composite qubit-bath interaction energy variables. Depending upon the state of the two qubits, the electrons will 'see' the bath in a fully correlated way or a partially or even minimally correlated manner. Depending upon this scenario, we defined an appropriate joint probability function for the interaction energy variables. We calculated the decoherence and the entanglement measures for various initial two-qubit states. It was noticed that the singlet and triplet states did not decohere or lose entanglement with respect to time. This is because these states happen to be the eigen states of the model Hamiltonian. We also considered superposition of singlet and triplet states in the limit of very small and very large magnitude of exchange interaction coefficient. For large value of exchange interaction, we noticed periodic oscillations in the entanglement measure. On the other hand, for no exchange interaction, we noticed no development of entanglement over time. Finally, we considered Bell states that are superposition of $|\uparrow\uparrow\rangle$ and $|\downarrow\downarrow\rangle$ states. In this case we observed decay of coherence as well as the degree of entanglement. We estimated a characteristic time which turned out to be a few nano seconds for quantum dots of radius 15nm.

As a final remark we state that the work presented in the thesis could be further improved in many ways. For example, by incorporating better methods of analysis such as exact diagonalization techniques to numerically solve the time-independent Schrodinger equation, more exact results could be achieved. Though such studies will definitely improve accuracy, they come with the cost of large computational power. Similarly the study of decoherence could be made with more detailed analytical models to capture the interactions between the system and the environment. Such improvements in the model may improve the results

but at the same time will complicate the calculations involved. Our main objective was to capture the essential features of the system in a simple manner so that the models are easily tractable. Such an approach of being simplistic in constructing models has been the guiding principle among physicists and engineers over a long time. We have followed the same principle in dealing with the problem of decoherence.

Since we have already addressed several problems and obtained a lot of features of the systems discussed in the thesis, it may be fair to draw the line at this point and leave the above mentioned possibilities for extensions as future assignments.

Appendix A

Here we list the value of various material parameters used in the calculation of hyperfine interaction strength. The material considered is GaAs and the values are adopted from reference [151].

The Bloch wave amplitude at the location of nucleus, $\eta = 3.6 \times 10^3$
g-factor of electron, $g_e = 2$
Bohr magneton, $\mu_B = 9.27 \times 10^{-24}$ JT^{-1}
Nuclear magneton, $\mu_N = 5.05 \times 10^{-27}$ JT^{-1}
Natural abundance of ^{69}Ga= 60.4%
Nuclear magnetic moment of ^{69}Ga= 2.016 μ_N
Natural abundance of ^{71}Ga= 39.6%
Nuclear magnetic moment of ^{71}Ga= 2.562 μ_N
Nuclear magnetic moment of ^{75}As= 1.439 μ_N
Average nuclear magnetic moment of GaAs= 1.836 μ_N
Permeability of free space, $\mu_0 = 4\pi \times 10^{-7}$ Hm^{-1}
The strength of hyperfine interaction (apart from the square of the envelope function),

$$\kappa = \frac{2}{3\hbar^2}\mu_0 g_e g_N \mu_B \mu_N \eta = 1.62\,\mu\text{eV nm}^3.$$

Appendix B

List of papers from this thesis:

1. Agile Mathew and Malay K. Nandy. Revisiting the problem of a single electron cylindrical quantum dot in constant magnetic field. *Physica E*, **42**: 1383-1386, 2010.
2. Agile Mathew and Malay K. Nandy. Two electrons in a cylindrical quantum dot under constant magnetic field. *Physica B*, **421**: 127-131, 2013.
3. Agile Mathew and Malay K. Nandy. Decoherence study of electron spin states in quantum dots using a simplistic model. *Mod. Phys. Lett. B*, **27**: 1350119, 2013.
4. Agile Mathew and Malay K. Nandy. An electron under impurity potential and magnetic field in a two-dimensional system. (To be communicated).
5. Agile Mathew and Malay K. Nandy. Two electrons in laterally coupled quantum dots under constant magnetic field. (To be communicated).
6. Agile Mathew and Malay K. Nandy. Decoherence of two-electron spin qubits in quantum dots due to Ising type hyperfine interaction. (To be communicated).

References

[1] A. Einstein, B. Podolsky, and N. Rosen. Can quantum-mechanical description of physical reality be considered complete? *Phys. Rev.*, 47:777–780, 1935. 3

[2] Alain Aspect, Jean Dalibard, and Gérard Roger. Experimental test of bell's inequalities using time- varying analyzers. *Phys. Rev. Lett.*, 49:1804, 1982. 3

[3] John S. Bell. On the Einstein Podolsky Rosen Paradox. *Physics*, 1:195–200, 1964. 3

[4] D.P. DiVincenzo. Quantum information is physical. *Superlatt. Microstruct.*, 23:419–432, 1998. 6

[5] K. Roy, S. Mukhopadhyay, and H. Mahmoodi-Meimand. Leakage current mechanisms and leakage reduction techniques in deep-submicrometer cmos circuits. *Proceedings of the IEEE*, 91:305–327, 2003. 6

[6] R.P. Feynman. Simulating physics with computers. *Int. J. Theor. Phys.*, 21, 1982. 7

[7] Paul Benioff. Quantum mechanical hamiltonian models of turing machines. *J. Stat. Phys.*, 29:515–546, 1982. 7

[8] D. Deutsch. Quantum theory, the Church-Turing principle and the universal quantum computer. *Proc. R. Soc. Lond. A*, 400:97–117, 1985. 7

[9] D. Deutsch. Rapid solution of problems by quantum computation. *Proc. R. Soc. Lond. A*, 439:553–558, 1992. 7

[10] P.W. Shor. Polynomial-time algorithms for prime factorization and discrete logarithms on a quantum computer. *SIAM Journal on Computing*, 26:1484, 1997. 7

[11] L.K. Grover. A fast quantum mechanical algorithm for database search. *Proceedings, 28th Annual ACM Symposium on the Theory of Computing*, pages 212–219, 1996. 7

[12] D.P. DiVincenzo. Quantum computation. *Science*, 270:255–261, 1995. 7

[13] T.D. Ladd, F. Jelezko, R. Laflamme, et al. Quantum computers. *Nature*, 464:45–53, 2010. 7

[14] C.H. Bennett, G. Brassard, C. Crépeau, et al. Teleporting an unknown quantum state via dual classical and Einstein-Podolsky-Rosen channels. *Phys. Rev. Lett.*, 70:1895, 1993. 7

[15] C.H. Bennett and G. Brassard. Quantum cryptography: Public key distribution and coin tossing. In *Proceedings of the IEEE International Conference on Computer, Systems, and Signal Processing, Bangalore, India*, pages 175–179, 1984. 7

[16] Dominic Mayers. Unconditionally secure quantum bit commitment is impossible. *Phys. Rev. Lett.*, 78:3414, 1997. 7

[17] C.B. Murray, C.R. Kagan, and M.G. Bawendi. Synthesis and characterization of monodisperse nanocrystals and close-packed nanocrystal assemblies. *Annual Review of Materials Science*, 30:545—610, 2000. 8

[18] N.N. Ledentsov, V.M. Ustinov, V.A. Shchukin, et al. Quantum dot heterostructures: Fabrication, properties, lasers (review). *Semiconductors*, 32:343–365, 1998. 8

[19] A. Tartakovskii. *Quantum Dots: Optics, Electron Transport and Future Applications*. Cambridge Univ. Press, 2012. 8

[20] M.A. Kastner. Artificial atoms. *Physics Today*, 46:24–31, 1993. 8

[21] R.C. Ashoori. Electrons in artificial atoms. *Nature*, 379:413–419, 1996. 8

[22] T.A. Fulton and G.J. Dolan. Observation of single-electron charging effects in small tunnel junctions. *Phys. Rev. Lett.*, 59:109–112, 1987. 8

[23] H. Grabert and M.H. Devoret. *Single Charge Tunneling: Coulomb Blockade Phenomena in Nanostructures*. Plenum Press, New York, 1992. 8

[24] M.A. Reed, R.T. Bate, K. Bradshaw, et al. Spatial quantization in GaAs-AlGaAs multiple quantum dots. *J. Vac. Sci. Technol. B*, 4:358–360, 1986. 8

[25] G.W. Bryant. Excitons in quantum boxes: Correlation effects and quantum confinement. *Phys. Rev. B*, 37:8763, 1988. 8

[26] T. Chakraborty. *Quantum Dots: A Survey of the Properties of Artificial Atoms*. Elsevier Science, 1999. 8, 14, 23, 39, 42

[27] S.M. Reimann and M. Manninen. Electronic structure of quantum dots. *Rev. Mod. Phys.*, 74:1283, 2002. 8, 39

[28] P.A. Ling. *Trends In Quantum Dots Research*. Nova Science, 2005. 8

[29] M.A. Kastner. The single electron transistor and articial atoms. *Ann. Phys. (Leipzig)*, 9:885–894, 2000. 8

[30] S. Kafanov, A. Kemppinen, Yu. A. Pashkin, et al. Single-electronic radio-frequency refrigerator. *Appl. Phys. Lett*, 76:120801, 2009. 8

[31] R.J. Young, S.J Dewhurst, R.M. Stevenson, et al. Single electron-spin memory with a semiconductor quantum dot. *New J. Phys.*, 9:365, 2007. 8, 14

[32] C. Santori, M. Pelton, G. Solomon, et al. Triggered single photons from a quantum dot. *Phys. Rev. Lett.*, 86:1502, 2001. 8

[33] M. Feng, K.L. Silverman, R.P. Mirin, et al. Dark pulse quantum dot diode laser. *Opt. Express*, 18:13385, 2010. 8

[34] A.G. Curto, G. Volpe, T.H. Taminiau, et al. Unidirectional emission of a quantum dot coupled to a nanoantenna. *Science*, 329:930–933, 2010. 8

[35] E. Jang, S. Jun, H. Jang, et al. White-light-emitting diodes with quantum dot color converters for display backlights. *Adv. Mater.*, 22:3076, 2010. 8

[36] S.D. Gittard, P.R. Miller, R.D. Boehm, et al. Multiphoton microscopy of transdermal quantum dot delivery using two photon polymerization-fabricated polymer microneedles. *Faraday Discuss.*, 149:171–185, 2011. 8

[37] O.E. Semonin, J.M. Luther, S. Choi, et al. Peak external photocurrent quantum efficiency exceeding 100in a quantum dot solar cell. *Science*, 334:1530, 2011. 8

[38] D. Loss and D.P. DiVincenzo. Quantum computation with quantum dots. *Phys. Rev. A*, 57:120–126, 1998. 9, 14, 68, 79

[39] G. Burkard, D. Loss, and D.P. DiVincenzo. Coupled quantum dots as quantum gates. *Phys. Rev. B*, 59:2070, 1999. 9, 14, 50, 54

[40] A. Barenco, C. H. Bennett, R. Cleve, et al. Elementary gates for quantum computation. *Phys. Rev. A*, 52:3457, 1995. 9

[41] G. Burkard, G. Seelig, and D. Loss. Spin interactions and switching in vertically tunnel-coupled quantum dots. *Phys. Rev. B*, 62:2581, 2000. 10, 14

[42] D. P. DiVincenzo, D. Bacon, J. Kempe, et al. Universal quantum computation with the exchange interaction. *Nature*, 408:339–342, 2000. 10

[43] J.R. Petta, A.C. Johnson, J.M. Taylor, et al. Coherent manipulation of coupled electron spins in semiconductor quantum dots. *Science*, 309:2180, 2005. 10, 14, 54, 68, 79

[44] Dimitrije Stepanenko and Guido Burkard. Quantum gates between capacitively coupled double quantum dot two-spin qubits. *Phys. Rev. B*, 75:085324, 2007. 10, 14

[45] Ari Mizel and Daniel A. Lidar. Exchange interaction between three and four coupled quantum dots: Theory and applications to quantum computing. *Phys. Rev. B*, 70:115310, 2004. 10, 14

[46] L. Trifunovic, O. Dial, M. Trif, et al. Long-distance spin-spin coupling via floating gates. *Phys. Rev. X*, 2:011006, 2012. 10

[47] B.E. Kane. A silicon-based nuclear spin quantum computer. *Nature*, 393:133 –137, 1998. 10, 26

[48] R. Vrijen, E. Yablonovitch, K. Wang, et al. Electron-spin-resonance transistors for quantum computing in silicon-germanium heterostructures. *Phys. Rev. A*, 62:012306, 2000. 10, 26, 54

[49] F.H.L. Koppens, C. Buizert, K.J. Tielrooij, et al. Driven coherent oscillations of a single electron spin in a quantum dot. *Nature*, 442:766–771, 2006. 10, 14

[50] K.C. Nowack, M. Shafiei, M. Laforest, et al. Single-shot correlations and two-qubit gate of solid-state spins. *Science*, 333:1269, 2011. 10

[51] R. Hanson, L. H. Willems van Beveren, I. T. Vink, et al. Single-shot readout of electron spin states in a quantum dot using spin-dependent tunnel rates. *Phys. Rev. Lett.*, 94:196802, 2005. 10

[52] D.P. DiVincenzo. The physical implementation of quantum computation. *arXiv:quant-ph/0002077*. 11

[53] Yu.A. Pashkin, Y. Nakamura, and J.S. Tsai. Room-temperature al single-electron transistor made by electron-beam lithography. *Appl. Phys. Lett.*, 76:2256, 2000. 14

[54] K. C. Nowack, F. H. L. Koppens, Yu. V. Nazarov, et al. Coherent control of a single electron spin with electric fields. *Science*, 318:1430, 2007. 14

[55] V. Fock. Bemerkung zur quantelung des harmonischen oszillators im magnetfeld. *Z. Phys.*, 47:446, 1928. 14

[56] T. Mano, T. Kuroda, S. Sanguinetti, et al. Self-assembly of concentric quantum double rings. *Nano Lett.*, 5:425, 2005. 14

[57] Ch. Heyn, C. Klein, S. Kramp, et al. Fabrication of quantum wires by in-situ ion etching and mbe overgrowth. *J. Cryst. Growth*, 227-228:980, 2001. 14

[58] D. Bimberg, M. Grundmann, and N. M. Lendentsov. *Quantum Dot Heterostructures*. Wiley, Chichester, 1999. 14

[59] L. Z. Liu and J. J. Liu. Hydrogenic-donor impurity states in coupled quantum disks in the presence of a magnetic field. *J. Appl. Phys.*, 102:033709, 2007. 15

[60] F. J. Culchac, N. P-. Montenegro, J. C. Granada, et al. Energy spectrum in a concentric double quantum ring of GaAs(Ga,Al)As under applied magnetic fields. *J. Microelectron.*, 39:402, 2007. 15

[61] F. J. Culchac, N. P-. Montenegro, and A. Latge. GaAs-(Ga, Al) As double quantum rings: confinement and magnetic field effects. *J. Phys.: Condens. Matter*, 20:285215, 2008. 15

[62] F.A.P. Osorio, A.B.A. Marques, P.C.M. Machado, et al. The effects of magnetic field on the energy levels of shallow donor impurities in GaAs/Al_xGa_{1-x}As quantum dots. *J. Microelectron.*, 36:244, 2005. 15

[63] M.E. Rensink. Electron eigenstates in uniform magnetic fields. *Am. J. Phys.*, 37:900, 1969. 15

[64] G. Li, S.V. Branis, and K.K. Bajaj. Hydrogenic donor states in quantum dots in the presence of a magnetic field. *Phys. Rev. B*, 47:15735, 1993. 15, 26

[65] S.V. Branis, G. Li, and K.K. Bajaj. Hydrogenic donor states in quantum dots in the presence of a magnetic field. *Phys. Rev. B*, 47:1316, 1993. 15, 26

[66] R.B. Dingle. Some magnetic properties of metals. I. General introduction, and properties of large systems of electrons. *Proc. R. Soc. A*, 211:500, 1952. 18, 21

[67] L.D. Landau and E.M. Lifshitz. *Quantum Mechanics: Non-Relativistic Theory*. Pergamon Press, 3rd edition, 1973. 18, 21

[68] M. Abramowitz and I.A. Stegun. *Handbook of Mathematical Functions*. Dover Publication, New York, 1970. 18

[69] S. Wolfram. *The Mathematica Book*. Wolfram Media, 5th edition, 2003. 20

[70] C.G. Darwin. The diamagnetism of the free electron. *Proc. Cambridge Philos. Soc.*, 27:86, 1930. 21

[71] K. Huang. *Statistical Mechanics*. John Wiley, 2nd edition, 1987. 21

[72] J.P. Dowling and G.J. Milburn. Quantum technology: The second quantum revolution. *Phil. Trans. R. Soc. London A*, 361:1674, 2003. 25, 92

[73] G. Bastard. Hydrogenic impurity states in a quantum well: A simple model. *Phys. Rev. B*, 24:4714, 1981. 26

[74] R. L. Greene and K. K. Bajaj. Energy levels of hydrogenic impurity states in GaAs-GaAlAs Quantum well structures . *Solid State Commun.*, 45:825 –829, 1983. 26

[75] Bryant G. W. Hydrogenic impurity states in quantum-well wires. *Phys. Rev. B*, 29:6632, 1984. 26

[76] Jia-Lin Zhu, Jia-Jiong Xiong, and Bing-Lin Gu. Confined electron and hydrogenic donor states in a spherical quantum dot of GaAs-GaAlAs. *Phys. Rev. B*, 41:6001, 1990. 26

[77] Zhigang Xiao, Jiqian Zhu, and Fengai He. Magnetic field dependence of the binding energy of a hydrogenic impurity in a spherical quantum dot. *J. Appl. Phys.*, 79:9181, 1996. 26

[78] Chun-Ching Yang, Li-Chi Liu, and Shih-Hsin Chang. Eigenstates and fine structure of a hydrogenic impurity in a spherical quantum dot. *Phys. Rev. B*, 58:1954, 1998. 26

[79] Ruihao Wei and Wenfang Xie. Optical absorption of a hydrogenic impurity in a disc-shaped quantum dot. *Curr. Appl. Phys.*, 10:757– 760, 2010. 26

[80] K. M. Kumar, A. J. Peter, and C. W. Lee. Optical properties of a hydrogenic impurity in a confined $Zn_{1x}Cd_xSe/ZnSe$ spherical quantum dot. *Superlatt. Microstruct.*, 51:184 – 193, 2012. 26

[81] Wenfang Xie and Qiao Xie. Electric field effects of hydrogenic impurity states in a disc-like quantum dot. *Physica B: Condensed Matter*, 404:1625, 2009. 26

[82] Figen Karaca Boz and Saban Aktas. Magnetic field effect on the binding energy of a hydrogenic impurity in coaxial GaAs/ $Al_xGa_{1-x}As$ quantum well wires. *Superlatt. Microstruct.*, 37:281 – 291, 2005. 26

[83] Wenfang Xie. Nonlinear optical properties of a hydrogenic donor quantum dot. *Phys. Lett. A*, 372:5498, 2008. 26

[84] W.C. Chou, W.J. Huang, P.Y. Chu, et al. The binding energy of hydrogenic impurity in quantum well structures. *Physica B+C*, 150:361 – 368, 1988. 26

[85] Guangxin Wang and Peng Zhang. Hydrogenic impurity binding energy in self-assembled GaAs-GaAlAs quantum rings. *J. Appl. Phys.*, 103:063713, 2008. 26

[86] A. H. Macoonald and D. S. Ritchie. Hydrogenic energy levels in two dimensions at arbitrary magnetic fields. *Phys. Rev. B*, 33:8336, 1986. 27

[87] X. L. Yang, S. H. Guo, and F. T. Chan. Analytic solution of a two-dimensional hydrogen atom. I. Nonrelativistic theory. *Phys. Rev. B*, 43:1186, 1991. 27

[88] K. Eveker, D. Grow, B. Jost, et al. The two dimensional hydrogen atom with a logarithmic potential energy function. *Am. J. Phys.*, 58:1183, 1990. 27

[89] M. Taut. Two-dimensional hydrogen in a magnetic field: analytical solutions. *J. Phys. A: Math. Gen.*, 28:2081, 1995. 28

[90] J.-L. Zhu, Y. Chen, and J.-J. Xiong. Exact solutions for two-dimensional hydrogenic donor states in a magnetic field. *Phys. Lett. A*, 145:358 –362, 1990. 28

[91] W. H. Lim, F. A. Zwanenburg, H. Huebl, et al. Observation of the single-electron regime in a highly tunable silicon quantum dot. *Appl. Phys. Lett.*, 95:242102, 2009. 39

[92] F. Geerinckx, F. M. Peeters, and J. T. Devreese. Effect of the confining potential on the magneto-optical spectrum of a quantum dot. *J. Appl. Phys.*, 68:3435, 1990. 39

[93] C. Y. Ngo, S. F. Yoon, W. J. Fan, et al. Effects of size and shape on electronic states of quantum dots. *Phys. Rev. B*, 74:245331, 2006. 39

[94] Garnett W. Bryant. Electronic structure of ultrasmall quantum-well boxes. *Phys. Rev. Lett.*, 59:1140, 1987. 39

[95] Wenfang Xie. Two interacting electrons in a gaussian confining potential quantum dot. *Solid State Commun.*, 127:401–405, 2003. 39

[96] D. C. Thompson and A. Alavi. Three, four and five interacting electrons in a spherical box: an exact diagonalization study extended. *J. Phys.: Condens. Matter*, 16:7979, 2004. 39

[97] E. Welander and G. Burkard. Electric control of the exciton fine structure in non-parabolic quantum dots. *Phys. Rev. B*, 86:165312, 2012. 39

[98] Agile Mathew and Malay K. Nandy. Revisiting the problem of a single electron cylindrical quantum dot in constant magnetic field. *Physica E*, 42:1383, 2010. 39, 40

[99] B. Szafran, J. Adamowski, and S. Bednarek. Electron-electron correlation in quantum dots. *Physica E*, 5:185–195, 2000. 39

[100] U. Merkt, J. Huser, and M. Wagner. Energy spectra of two electrons in a harmonic quantum dot. *Phys. Rev. B*, 43:7320, 1991. 40

[101] M. Dineykhan and R. G. Nazmitdinov. Two-electron quantum dot in a magnetic field: Analytical results. *Phys. Rev. B*, 55:13707, 1997. 40

[102] J. T. Lin and T. F. Jiang. Two interacting electrons in a vertical quantum dot with magnetic fields. *Phys. Rev. B*, 64:195323, 2001. 40

[103] Mohammad El-Said. The spectral properties of two-electron quantum dot. *Physica E*, 14:323–329, 2002. 40

[104] B. S. Kandemir. Variational study of two-electron quantum dots. *Phys. Rev. B*, 72:165350, 2005. 40

[105] H. Hassanabadi, M. Hamzavi, and A. A. Rajabi. Analytical study of external magnetic field effect on the energy levels of a two-electron quantum dot. *Mod. Phys. Lett. B*, 24:1127, 2010. 40

[106] F. M. Peeters and V. A. Schweigert. Two-electron quantum disks. *Phys. Rev. B*, 53:1468, 1996. 40, 46, 49, 50, 52

[107] P. M. Mathews and K. Venkatesan. *A Textbook of Quantum Mechanics*. Tata McGraw-Hill. 42

[108] P. A. Maksym and T. Chakraborty. Effect of electron-electron interactions on the magnetization of quantum dots. *Phys. Rev. B*, 45:1947, 1992. 50

[109] M. Wagner, U. Merkt, and A. V. Chaplik. Spin-singlet–spin-triplet oscillations in quantum dots. *Phys. Rev. B*, 45:1951, 1992. 50

[110] C. Livermore, C. H. Crouch, R. M. Westervelt, et al. The coulomb blockade in coupled quantum dots. *Science*, 274:1332, 1996. 54

[111] A. Georges and Y. Meir. Electronic correlations in transport through coupled quantum dots. *Phys. Rev. Lett.*, 82:3508, 1999. 54

[112] A. P. Alivisatos. Semiconductor clusters, nanocrystals, and quantum dots. *Science*, 271:933, 1996. 54

[113] S. S. Li and J. B Xia. Intraband optical absorption in semiconductor coupled quantum dots. *Phys. Rev. B*, 55:15434, 1997. 54

[114] J. H. Oh and K. J. Chang. Electronic structure and optical properties of coupled quantum dots. *Phys. Rev. B*, 53:13264, 1996. 54

[115] T. Brandes and B. Kramer. Spontaneous emission of phonons by coupled quantum dots. *Phys. Rev. Lett.*, 83:3021, 1999. 54

[116] T. Aono and M. Eto. Kondo resonant spectra in coupled quantum dots. *Phys. Rev. B*, 63:125327, 2001. 54

[117] M. Tewordt, H. Asahi, V. J. Law, et al. Resonant tunneling in coupled quantum dots. *Appl. Phys. Lett.*, 60:595, 1992. 54

[118] L. Quiroga and N. F. Johnson. Entangled bell and greenberger-horne-zeilinger states of excitons in coupled quantum dots. *Phys. Rev. Lett.*, 83:2270, 1999. 54

[119] J.A. Lott, N.N. Ledentsov, V.M. Ustinov, et al. Vertical cavity lasers based on vertically coupled quantum dots. *Electron. Lett.*, 33:1150, 1997. 54

[120] C. S. Craig S. Lent, P. Douglas Tougaw, and W. Porod. Bistable saturation in coupled quantum dots for quantum cellular automata. *Appl. Phys. Lett.*, 62:714, 1993. 54

[121] L. H. Willems van Beveren. *Electron spins in few-electron lateral quantum dots*. PhD thesis, Delft University of Technology, 2005. 54

[122] M. M. Bayer, P. Hawrylak, K. Hinzer, et al. Coupling and entangling of quantum states in quantum dot molecules. *Science*, 291:451, 2001. 54

[123] G. G. Tarasov, Y. I. Mazur, Z. Y. Zhuchenko, et al. Carrier transfer in self-assembled coupled InAs/GaAs quantum dots. *J. Appl. Phys*, 88:7162, 2000. 54

[124] M. Fricke, A. A. Lorke, J. P. Kotthaus, et al. Shell structure and electron-electron interaction in self-assembled inas quantum dots. *Europhys. Lett*, 36:197, 1996. 55

[125] P. A. Maksym and T. Chakraborty. Quantum dots in a magnetic field: Role of electron-electron interactions. *Phys. Rev. Lett.*, 65:108, 1990. 55

[126] H. Drexler, D. Leonard, W. Hansen, et al. Spectroscopy of Quantum Levels in Charge-Tunable InGaAs Quantum Dots. *Phys. Rev. Lett.*, 73:2252, 1994. 55

[127] Tien-Kan Chuang and G.P. Carman. Magnetoelectronic nanoscale magnetic field generator. In *Proc. IEEE Solid-State Sensors, Actuators and Microsystems Conference, 2009*, page 640. 55

[128] A. Tsiatmas, E. Atmatzakis, N. Papasimakis, et al. Optical generation of intense ultrashort magnetic pulses at the nanoscale. *New J. Phys.*, 15:113035, 2013. 55

[129] S. Weinbaum. The normal state of the hydrogen molecule. *J. Chem. Phys.*, 1:593, 1933. 60

[130] E. Joos and H. D. Zeh. The emergence of classical properties through interaction with the environment. *Z. Phys. B: Cond. Mat.*, 59:223–243, 1985. 68

[131] W.H. Zurek. Decoherence and the transition from quantum to classical. *Physics Today*, 44:36–44, 1991. 68

[132] Wojciech Hubert Zurek. Decoherence, einselection, and the quantum origins of the classical. *Rev. Mod. Phys.*, 75:715–775, 2003. 68

[133] Alexander V. Khaetskii, Daniel Loss, and Leonid Glazman. Electron spin decoherence in quantum dots due to interaction with nuclei. *Phys. Rev. Lett.*, 88:186802, 2002. 68, 79

[134] W. A. Coish and Daniel Loss. Hyperfine interaction in a quantum dot: Non-markovian electron spin dynamics. *Phys. Rev. B*, 70:195340, 2004. 68, 80

[135] Łukasz Cywiński, Wayne M. Witzel, and S. Das Sarma. Pure quantum dephasing of a solid-state electron spin qubit in a large nuclear spin bath coupled by long-range hyperfine-mediated interactions. *Phys. Rev. B*, 79:245314, 2009. 68

[136] D. D. Bhaktavatsala Rao, V. Ravishankar, and V. Subrahmanyam. Spin decoherence from hamiltonian dynamics in quantum dots. *Phys. Rev. A*, 74:022301, 2006. 68

[137] F. H. L. Koppens, J. A. Folk, J. M. Elzerman, et al. Control and Detection of Singlet-Triplet Mixing in a Random Nuclear Field. *Science*, 309:1346, 2005. 68

[138] H. Bluhm, S. Foletti, I. Neder, et al. Dephasing time of GaAs electron-spin qubits coupled to a nuclear bath exceeding 200us. *Nat Phys*, 7:109–113, 2011. 68, 78

[139] Denis V. Bulaev and Daniel Loss. Spin relaxation and anticrossing in quantum dots: Rashba versus dresselhaus spin-orbit coupling. *Phys. Rev. B*, 71:205324, 2005. 68

[140] K. Roszak and P. Machnikowski. Phonon-induced dephasing of singlet-triplet superpositions in double quantum dots without spin-orbit coupling. *Phys. Rev. B*, 80:195315, 2009. 68

[141] Wang Yao, Ren-Bao Liu, and L. J. Sham. Theory of electron spin decoherence by interacting nuclear spins in a quantum dot. *Phys. Rev. B*, 74:195301, 2006. 68

[142] H.-P. Breuer and F. Petruccione. *The Theory of Open Quantum Systems*. Oxford University Press, 2002. 69

[143] Maximilian A. Schlosshauer. *Decoherence and the Quantum-to-Classical Transition*. Springer, 2007. 69

[144] W. H. Zurek. Environment-induced superselection rules. *Phys. Rev. D*, 26:1862, 1982. 69

[145] Z. Gedik. Spin bath decoherence of quantum entanglement. *Solid State Communications*, 138:82–85, April 2006. 69

[146] F. M. Cucchietti, J. P. Paz, and W. H. Zurek. Decoherence from spin environments. *Phys. Rev. A*, 72:052113, Nov 2005. 69, 70

[147] Alexander V. Khaetskii and Yuli V. Nazarov. Spin relaxation in semiconductor quantum dots. *Phys. Rev. B*, 61:12639, 2000. 79

[148] Jo-Tzu Hung, Łukasz Cywiński, Xuedong Hu, et al. Hyperfine interaction induced dephasing of coupled spin qubits in semiconductor double quantum dots. *Phys. Rev. B*, 88:085314, 2013. 80

[149] Wenxian Zhang, V. V. Dobrovitski, K. A. Al-Hassanieh, et al. Hyperfine interaction induced decoherence of electron spins in quantum dots. *Phys. Rev. B*, 74:205313, 2006. 80

[150] William K. Wootters. Entanglement of formation of an arbitrary state of two qubits. *Phys. Rev. Lett.*, 80:2245, 1998. 83

[151] J. Schliemann, A. Khaetskii, and D. Loss. Electron spin dynamics in quantum dots and related nanostructures due to hyperfine interaction with nuclei. *J. Phys.: Cond. Mat.*, 15:1809, 2003. 97